Analysis of Ventral Furrow Formation in the *Drosophila* Embryo using Developmental Genetics in Combination with Computational Modelling

Dissertation

der Mathematisch-Naturwissenschaftlichen Fakultät

der Eberhard Karls Universität Tübingen

zur Erlangung des Grades eines

Doktors der Naturwissenschaften

(Dr. rer. nat.)

vorgelegt von

Philipp Spahn

aus Berlin

Tübingen

2013

Tag der mündlichen Qualifikation:	31.10.2013
Dekan:	Prof. Dr. Wolfgang Rosenstiel
1. Berichterstatter:	Prof. Dr. Rolf Reuter
2. Berichterstatter:	PD Dr. Ulrike Zentgraf
3. Berichterstatter:	Prof. Dr. Jörg Großhans

"All models are wrong, but some are useful."

George E. P. Box

1 TECHNICAL PREFACE

This thesis comes with supplemental videos that are provided as QuickTime files on the CD attached to the inside of the back cover. The implementation of the computational model in section 6.2 was done in MATLAB (The MathWorks). The code of the script is presented in the appendix and included on CD.

Abbreviations:

VFF	Ventral furrow formation	PMG	Posterior midgut
AJ	Adherens junction	DE-Cad	Drosophila E-cadherin
GLC	Germline clones	Arm	Armadillo (β-catenin)
EMT	Epithelial-to-mesenchymal transition	Zip	Zipper (myosin II)
PDZ	Acronym for PSD95, Disc-large, ZO-1	Nrt	Neurotactin (membrane marker)
GEF	Guanine nucleotide exchange factor		

Important terms:

Ventral furrow formation	Formation of a band of constricted cells in the ventral epithelium during gastrulation (causing a shallow tissue indentation)
Ventral furrow invagination	Internalization of the mesoderm anlage during gastrulation
Apical constriction	Reduction of apical cell surface area
Cell contraction	Contraction of the actomyosin meshwork underlying the apical cell surface
Myosin coalescence	Dense structures of myosin (as evident in confocal imaging) indicating contraction of the actomyosin meshwork
Stagnation period	Time period during gastrulation over which apical surface area of a cell remains temporarily constant because constriction stagnates
Cytoskeletal ratchet	Mechanism proposed in Martin et al. (2009) by which the actomyosin executes ± three alternating phases of contraction and stabilization and, thus, incrementally reduces the surface area of the cell

All these terms are explained in the text in more detail.

2 CONTENTS

3 ABSTRACT

This work explores cell biological mechanisms of ventral furrow formation during gastrulation of the fruit fly embryo (*Drosophila melanogaster*). During ventral furrow formation a band of cells in the ventral epithelium undergoes apical constriction (i.e. cells reduce their apical surface area) and forms a shallow indentation in the epithelium (the ventral furrow). Subsequently, this band of cells is invaginated into the interior of the embryo constituting the anlage of the mesoderm. Ventral furrow formation serves as a premier model system to study large-scale tissue movements in development as it is amenable to genetic manipulation and easily accessible to microscopic analysis.

In the first part of this work, we show that two genes – *dizzy (dzy)* and *rap1* – are critical to allow the proper formation of the furrow. Analyzing live-recordings of ventral furrow formation via automatic cell-tracking, we find that maternal loss of Dzy results in delayed apical constriction of ventral cells while maternal loss of Rap1 largely abolishes apical constriction. This causes ventral furrow formation to slow down or to fail, respectively. In both cases the actomyosin is unaffected but the establishment of apical adherens junctions is compromised: Upon loss of Dzy this apical junction establishment is slowed down, upon loss of Rap1 it only occurs fragmentarily with a conspicuous fraction of DE-cadherin being mislocalized to the cytoplasm. Overexpression of Dzy or Rap1 after invagination of the furrow interferes with the formation of the mesodermal monolayer as mesodermal cells clump and do not fully spread apart, correlating with the failure to reduce junction levels in the membranes. Together, these results point to a pivotal role of Dzy and Rap1 in the establishment and possibly the maintenance of adherens junctions during gastrulation.

In the second part of this work we undertake a modelling approach to assist the analysis of ventral furrow formation via computer simulation. We model the epithelium as a sheet of

hexagonal cells in a 2D surface view and equip the cells with biophysical properties, such as elasticity and contractility. The model shows that a lateral-to-ventral gradient of increasing cell contractility in the epithelium is a critical requirement to reproduce the morphology of the ventral furrow. The notion of such a gradient is supported *in vivo* by tracking labelled myosin in live-recordings. Based on combined analysis of *in silico* and *in vivo* data we challenge a previous view on ventral furrow formation as we do not find evidence for a cytoskeletal "ratchet"-mechanism by which cells would actively stabilize their constricted state between contraction pulses. We prefer to describe ventral furrow formation as a stochastic process where cells execute autonomous stochastic actomyosin contractions, under the constraint of their elasticity as well as their mechanical coherence in the epithelium. With this stochastic concept being in good congruence to experimental data, we show that ventral furrow formation can occur with less regulatory complexity than previously postulated.

4 ZUSAMMENFASSUNG

Diese Arbeit untersucht zellbiologische Mechanismen der Ventralfurchenbildung während der Gastrulation des Embryos der Taufliege (*Drosophila melanogaster*). Im Zuge der Ventralfurchenbildung macht ein Band von Zellen entlang des ventralen Epithels apikale Konstriktion (d.h. die Zellen verkleinern ihre apikale Oberfläche) und bildet eine flache Einbuchtung im Epithel (die Ventralfurche). Anschließend wird dieses Zellband in das Innere des Embryos invaginiert und bildet die Anlage des Mesoderms. Die Ventralfurchenbildung dient als hervorragendes Modelsystem, um groß angelegte Gewebeumlagerungen während der Embryonalentwicklung zu studieren, da sie der genetischen Manipulation zugänglich ist und leicht mikroskopisch untersucht werden kann.

Im ersten Teil dieser Arbeit zeigen wir, dass die zwei Gene *dizzy (dzy)* und *rap1* essentiell sind, um eine reguläre Ventralfurchenbildung zu gewährleisten. Durch Analyse von Live-Aufnahmen der Ventralfurchenbildung mittels automatischen Zell-Trackings zeigt sich, dass das maternale Fehlen von Dzy zur verspäteten apikalen Konstriktion ventraler Zellen führt, während das maternale Fehlen von Rap1 apikale Konstriktion größtenteils unterbindet. Als Folge davon bildet sich die Ventralfurche verlangsamt bzw. überhaupt nicht. In beiden Fällen ist das Aktomyosin nicht betroffen, jedoch ist der Aufbau apikaler Adhäsionskontakte beeinträchtigt: Beim Fehlen von Dzy findet dieser Aufbau verlangsamt statt, beim Fehlen von Rap1 vollzieht er sich nur fragmentarisch, wobei ein auffallender Anteil von DE-Cadherin im Cytoplasma mislokalisiert ist. Überexpression von Dzy oder Rap1 nach Invagination der Furche behindert die Bildung des mesodermalen Monolayers, da mesodermale Zellen zusammenklumpen und sich nicht vollständig voneinander lösen, in Korrelation mit dem nicht stattfindenden Abbau von Adhäsionskontakten in den Membranen. Zusammengenommen deuten diese Ergebnisse auf eine entscheidende Rolle von Dzy und

Rap1 beim Aufbau und möglicherweise der Erhaltung von Adhäsionskontakten während der Gastrulation.

Im zweiten Teil dieser Arbeit verfolgen wir einen Modellierungs-Ansatz, um die Analyse der Ventralfurchenbildung per Computersimulation zu unterstützen. Wir modellieren das Epithel als eine Schicht hexagonaler Zellen in einer 2D-Oberflächen-Ansicht und geben den Zellen bio-physikalische Eigenschaften wie Elastizität und Kontraktilität. Das Modell zeigt, dass ein Gradient ansteigender Kontraktilität von lateral nach ventral im Epithel vorhanden sein muss, um die Morphologie der Ventralfurche zu reproduzieren. Die Hypothese eines solchen Gradienten wird *in vivo* gestützt durch die Betrachtung von markiertem Myosin in Live-Aufnahmen. Basierend auf der kombinierten Analyse von *in silico*- und *in vivo*-Daten bezweifeln wir eine bestehende Hypothese zur Ventralfurchenbildung, da wir keine Hinweise für einen "Ratschen"-Mechanismus des Cytoskeletts finden, demzufolge Zellen ihren unvollständig konstringierten Apex zwischen zwei Kontraktionspulsen aktiv stabilisieren. Wir ziehen es vor, die Ventralfurchenbildung als stochastischen Prozess aufzufassen, bei dem Zellen autonome stochastische Aktomyosin-Kontraktionen ausführen, unter der Einschränkung durch ihre eigene Elastizität sowie den mechanischen Zusammenhalt im Epithel. Da diese stochastische Auffassung gut mit experimentellen Daten in Einklang steht, zeigen wir, dass die Ventralfurchenbildung mit weniger regulatorischer Komplexität als zuvor postuliert ablaufen kann.

5 INTRODUCTION

5.1 Adherens Junctions (AJs)

AJs are adhesion contacts typically found in epithelial cells. AJs consist of clusters of the transmembrane protein DE-cadherin (DE-Cad) that mediate adhesion to the neighbouring cell via homophilic interaction. On the cytoplasmic side, DE-Cad is complexed with different catenins (α-catenin, β-catenin, p120-catenin) physically linking the cadherin cluster to the actin cytoskeleton. Recent work has indicated that this linkage is much more dynamic and less intuitive than suggested by the classical textbook view that considered α- and β-catenin to be static molecular tethers (Desai et al., 2013; Drees et al., 2005; Gates & Peifer, 2005; Yamada et al., 2005). By establishing a mechanical link between the cytoskeleton and cell membranes, AJs serve as anchors to translate actomyosin contractions to cell shape change. In *Drosophila,* AJs are set up during cellularization (reviewed in Tepass et al. (2001)) and are critical prerequisites for the the constriction of ventral cells during the formation of the ventral furrow at gastrulation (Dawes-Hoang et al., 2005; Kölsch et al., 2007).

5.2 Ventral furrow formation

Gastrulation is the first major morphogenetic event during *Drosophila* embryogenesis and an outstanding model system to address the mechanisms by which cell shape changes evoke fast, large-scale tissue rearrangements. During *Drosophila* gastrulation a large portion of the ventral epithelium – defined through the presence of both Snail (Sna) and Twist (Twi) expression, but the absence of Huckebein (Hkb) expression (which is restricted to the poles) – invaginates into the interior of the embryo and constitutes the anlage of the mesoderm. This large tissue invagination is preceded by apical constriction of ventral cells leading to a long

indentation along the ventral epithelium, the so-called ventral furrow (reviewed in Leptin (1999), also see Video 1 (wt) for a lateral view, Video 3 (wt) for a surface view and Video 5 for a cross-sectional view of this process). Owing to its easy accessibility and its resemblance to vertebrate neural tube closure (reviewed in Suzuki et al. (2012)), the formation and invagination of the ventral furrow are attractive model systems to study large tissue rearrangements in development. Apical cell constriction appears to be a major driving force of tissue invagination since loss of apical constriction severely hampers tissue invagination both during *Drosophila* gastrulation (Leptin, 1999) and in vertebrate development (e.g.: Kinoshita et al., 2008; Plageman et al., 2011). In *Drosophila*, a considerable amount of experimental data has been obtained so far providing a coherent picture of the cell biology of apical constriction: Twist (Twi) – being a determinant of ventral fate (Simpson, 1983) – activates two targets, Folded Gastrulation (Fog) and T48, which work in parallel to localize RhoGEF2 to the apical membrane (Kölsch et al., 2007): Fog is an autocrine ligand triggering a G-protein coupled cascade involving the Gα-subunit Concertina (Cta) (Costa et al., 1994; Parks & Wieschaus, 1991). As suggested from studies in *Drosophila* S2 cells (Rogers et al., 2004), Cta then leads to the release of RhoGEF2 from microtubules making it available for localization to the apical membrane. Recruitment of RhoGEF2 to the apical membrane is thought to occur through the apical transmembrane protein T48 via a PDZ binding motif (Kölsch et al., 2007). The ventral localization of RhoGEF2 now triggers the accumulation of contractile actomyosin in the apices of ventral cells (Barrett et al., 1997; Dawes-Hoang et al., 2005; Häcker & Perrimon, 1998; Nikolaidou & Barrett, 2004; also see Fig. 25A). This apical actomyosin assembles into a contractile meshwork spanning the inner apical cell membrane (Martin et al., 2009). In parallel, adherens junctions are built up in a prominent apical belt around the epithelium. Actomyosin contractions occur in a discontinuous, asynchronous fashion and are thought to incrementally reduce the surface area of ventral cells in an alternation of Sna-

dependent contraction pulses and Twi-dependent stabilizations (Martin et al., 2009). This way, apical area of ventral cells is typically reduced in an incremental, step-like manner (Martin et al., 2009).

Although in section 6.2 of this work we question this postulated Twi-dependent stabilization mechanism, the genetic pathway leading from ventral fate determination to ventrally confined actomyosin contraction is generally agreed upon and fairly well understood (Fig. 25A). In contrast, it has remained unknown what signals ensure the well-timed assembly of apical adherens junctions at the onset of gastrulation. As mentioned above, presence of apical adherens junctions is a critical prerequisite to couple the contracting actomyosin to cell membranes and allow cells to undergo shape change (Dawes-Hoang et al., 2005; Martin et al., 2009; Roh-Johnson et al., 2012; Sawyer et al., 2009; Spahn et al., 2012). In section 6.1 of this work we show that apical junction assembly depends on the small GTPase Rap1 and its PDZ-GEF Dizzy. In section 6.2 we investigate how discontinuous, asynchronous cell contractions achieve apical constriction of a band of cells by contemplating a computational model of ventral furrow formation.

5.3 Dizzy – a PDZ-GEF for the small GTPase Rap1

Dizzy (Dzy) belongs to a highly conserved family of PDZ-GEFs that act on Rap GTPases (de Rooij et al., 1999). Guanine nucleotide exchange factors (GEFs) trigger the activity of GTPases by catalyzing the exchange of GDP by GTP, bound to the GTPase. In general, multiple GEFs can act on the same GTPase, and one GEF may also target multiple GTPases (reviewed in Schmidt & Hall (2002)). PDZ is the acronym for PSD95 (Postsynaptic density protein), Disc-large (found in septate junctions) and ZO-1 (found in the zonula occludens), three proteins in which this domain was first identified. Subsequently, PDZ domains have

been found in a number of other proteins, often involved in multiprotein complexes. PDZ domains can be bound by a PDZ binding motif, a short C-terminal motif occurring in many GEFs. Thus, PDZ domains are thought to enhance signalling specificity by providing a scaffold through which target proteins, such as GEFs, are organized into a signalling complex (reviewed in Garcia-Mata & Burridge (2007)). In addition, a class of GEFs for Rap or Rho GTPases feature PDZ domains themselves (PDZ-GEFs) (Kuiperij et al., 2003; Rumenapp et al., 1999). In *Drosophila*, the PDZ-GEF Dzy has been implicated in a variety of processes, such as eye or testis development (Lee et al., 2002; Wang et al., 2006), epithelial morphogenesis in wing discs and dorsal closure (Boettner & Van Aelst, 2007) and macrophage migration (Huelsmann et al., 2006; Siekhaus et al., 2010). In these processes, Dzy acts through the small GTPase Rap1 and regulates cell adhesion mediated by DE-Cad or integrins. Rap1 also has numerous functions during development throughout various model systems most of which are linked to regulation of adhesion to neighbouring cells or the extracellular matrix (reviewed in Boettner & Van Aelst (2009)). In particular, it has been shown that loss of Rap1 leads to defects in cell-cell adhesion, due to disturbed distribution of AJs in cell membranes (Knox & Brown, 2002). In addition, the formation of the ventral furrow has been found to depend on maternally provided Rap1 (Asha et al., 1999).

Zygotic loss of Dzy is recessive semi-lethal as homozygous *dzy* escapers are very rare, while maternal loss of Dzy, as seen in offspring from escaper mothers, leads to early defects in embryogenesis with an aberrant morphology during gastrulation (Ott, 2010). This prompts the hypothesis that maternal Dzy plays a role in ventral furrow formation. This hypothesis is in congruence to Dzy acting on Rap1 since maternal Rap1 has long been known to be involved in ventral furrow formation (Asha et al., 1999; Sawyer et al., 2009), albeit without being studied in sufficient detail. In section 6.1 of this work, the ventral furrow phenotypes of *dzy* and *rap1* are characterized.

5.4 Computational approaches to *Drosophila* gastrulation

As mentioned above, a large pool of experimental data has been gathered concerning factors involved in *Drosophila* gastrulation. However, the mechanisms of formation and invagination of the ventral furrow cannot be fully comprehended without considering the physical aspects involved in a tissue rearrangement of this magnitude. Thus, a number of computational models have been developed to address the question how shape change of epithelial cells, such as apical constriction, can facilitate the invagination of tissue from a physical point of view. Mostly, these models simulate tissue invagination in a 2D-representations of the embryo in cross-section (Conte et al., 2012; Brodland et al., 2010; Conte et al., 2009; Hočevar & Ziherl, 2011; Pouille & Farge, 2008; Hočevar Brezavšček et al., 2012). These studies have made aware that apical constriction in ventral cells may not be sufficient to assure proper invagination of the furrow, and pushing forces arising in the lateral epithelium may be required to internalize the tissue (Conte et al., 2009; Conte et al., 2012). It has also been investigated how shape change affects the mechanical tension of cells and how inhomogeneity of tension in the epithelium determines the site of invagination (Hočevar Brezavšček et al., 2012).

To keep the nomenclature consistent throughout this article, we choose to clearly differentiate between successive stages of *Drosophila* gastrulation (reviewed in Leptin (1999)) and use the term "ventral furrow formation" only to describe the early stage of gastrulation, spanning from the completion of cellularization to the formation of a band of constricted cells along the ventral epithelium. In particular, we prefer to clearly separate "furrow formation" from "furrow invagination" which refers to the subsequent stage when the mesoderm anlage folds into the interior of the embryo (Fig. 19A; Video 5). While the biomechanics of furrow invagination have been thoroughly addressed as mentioned above, the formation of the furrow

itself, i.e. the emergence of a ventral band of constricted cells, has not caught much attention yet in computational modelling. Although much progress has been made identifying the genetic players involved in apical constriction, it is an open question what essential regulatory inputs are required to make cells of the ventral epithelium undergo a joint constriction leading to the formation of a band of constricted cells. Computational modelling is a premier method to address this issue since simulating a complex process *in silico* can clarify which mechanisms are critical to explain *in vivo* observations or whether postulates drawn from experimental data may be expendable.

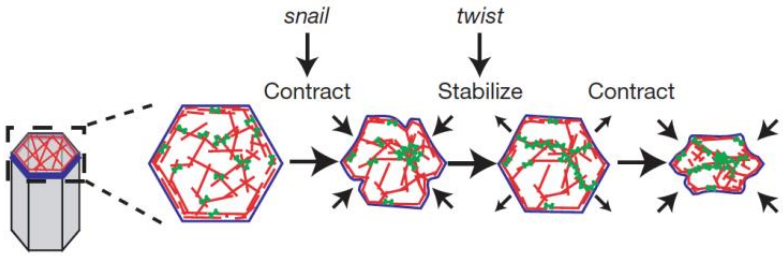

Fig. 1: The ratchet model. Alternating phases of Sna-dependent contractions and Twi-dependent stabilizations are supposed to incrementally reduce cell surface area during ventral furrow formation (Taken from Martin et al. (2009)).

In a well-noticed article (Martin et al., 2009) apical constriction was proposed to occur in an incremental fashion with ventral cells triggering ± three contraction pulses, while actively stabilizing the partly constricted surface between contraction pulses via a Twi-dependent mechanism (Martin et al., 2009; see Fig. 1). However, the molecular nature of this postulated "ratchet"-mechanism has remained elusive, and it has not been explored whether this mechanism represents a consistent and parsimonious concept to explain the experimental data obtained from live-recordings. Driquez and colleagues (Driquez et al., 2011) present 1D and 2D computational models addressing the formation of the furrow, assuming a two-phase process where Sna–dependent random oscillations trigger a second, Fog–dependent phase to constrict the apical surfaces in a rigorously regulated fashion. These assumptions are largely

based on data in Pouille et al. (2009) and Martin et al. (2009). However, their models do not provide direct representations of the apical surface of the ventral epithelium. What is more, their models are constructed based on very detailed assumptions concerning the regulation of apical constriction and, thus, cannot answer the question whether less regulatory input may also be sufficient to explain the experimental data.

In section 6.2 of this work we adopt a popular so-called vertex model to describe physical properties of cells (such as tension, elasticity and contractility) in the ventral epithelium during furrow formation. In contrast to earlier approaches, this model directly depicts the epithelium in an apical surface view allowing direct comparison to live-recordings of the furrow taken in surface view. The model proves capable of accurately reproducing ventral furrow formation both qualitatively and quantitatively. Based on combined evidence from our model and experimental data we show that the dynamics of apical cell constriction can be well explained without postulating an underlying ratchet mechanism and discuss a more parsimonious concept of ventral furrow formation.

6 RESULTS

6.1 Rap1 and its PDZ-GEF Dizzy regulate the establishment of adherens junctions required for ventral furrow formation

In this section, we show that Dzy is involved in the regulation of ventral furrow formation (VFF), since lack of maternally provided Dzy results in a slowdown of apical constriction in ventral cells, correlating with a slowdown of apical AJ assembly around the epithelium. We extend previous studies on the role of Rap1 in VFF as we find the formation of apical AJs to critically depend on Rap1. In the absence of maternal Rap1 the major AJ component DE-Cadherin (DE-Cad) is aberrantly dispersed within cells of the entire epithelium and is not

accumulated into an apical junction belt. In addition, we show that Dzy and Rap1 cause defects when ectopically expressed in the internalized mesoderm. After epithelial-to-mesenchymal transition (EMT) mesodermal cells are impeded in their migration and monolayer formation.

6.1.1 Ventral furrow formation requires maternal contribution of Dzy and Rap1.

We generated germline clones (GLC), eliminating the maternal contribution of Dzy or Rap1, to address their early function in the *Drosophila* embryo. We find that VFF is the first process to be dependent on Dzy as it is severely disturbed in the GLC (Fig. 2). In wildtype embryos the ventral furrow forms during stage 6 (Fig. 2 D,D') and has closed at stage 7 (Fig. 2G,G'). In contrast, in *dzy* GLC the furrow is rudimentary at stage 6 (Fig. 2E,E') and is closed incompletely at stage 7 (Fig. 2H,H').

Dzy activates the small GTPase Rap1 in other morphogenetic events of *Drosophila* (Boettner & Van Aelst, 2007; Huelsmann et al., 2006). Since Rap1 has also been implicated in VFF (Asha et al., 1999; Sawyer et al., 2009), the phenotypes of *rap1* GLC were compared to *dzy* GLC. VFF is more severely affected in *rap1* GLC: at stage 6 no tissue indentation is visible at the ventral embryo surface (Fig. 2F,F') and no furrow has formed at stage 7 (Fig. 2I,I'), leaving the mesoderm primordium not internalized. These VFF phenotypes of *dzy* or *rap1* GLC are independent of the zygotic genotype of the embryo. They are seen in embryos lacking both maternal and zygotic Dzy or Rap1 contribution and in embryos merely lacking the maternal contribution.

The failure to form a proper ventral furrow is not due to defects in pattern formation in *dzy* or *rap1* GLC. The mesodermal transcription factors Twi (Fig. 2) and Sna (Fig. 3G–I) and the dorsal determinant *pnr* (Fig. 3A–C) are expressed in their normal dorsoventral domain during

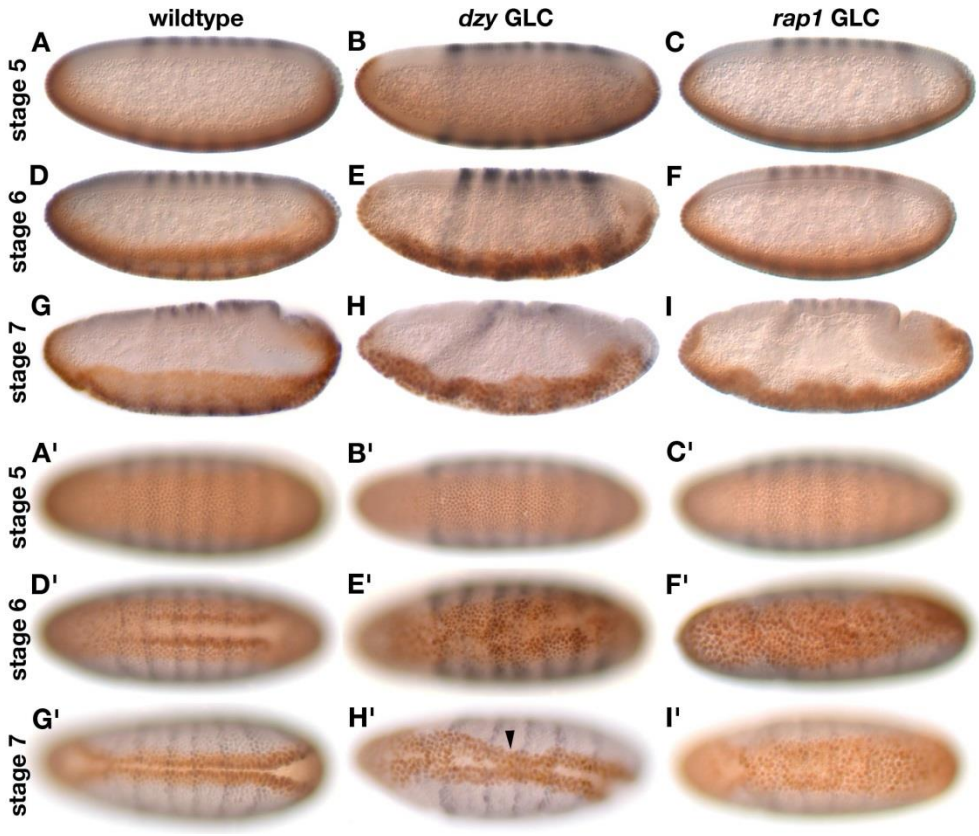

Fig. 2. Maternally provided Dzy and Rap1 are required for proper VFF. Wildtype embryos (A,A',D,D',G,G'), *dzy* GLC (B,B',E,E',H,H') and *rap1* GLC (C,C',F,F',I,I') stained for Twi (brown) and Eve protein (black). **A–C'**: Cellularization is not affected in *dzy* or *rap1* GLC. **D–F'**: During stage 6 a deep ventral furrow forms in wildtype (D,D'), but only a shallow groove forms in *dzy* GLC (E,E'). In *rap1* GLC a furrow is not evident (F,F'). **G–I'**: At stage 7 the mesoderm is fully invaginated in wildtype (G,G') while the furrow is only partially closed in *dzy* GLC (H,H', arrowhead). In *rap1* GLC the ventral furrow has failed to form (I,I'). Anterior left; A–I: sagittal view; A'–I': ventral view (same embryos).

and after cellularization in *dzy* and *rap1* GLC. Hence, loss of Dzy or Rap1 does not interfere with dorsoventral patterning. Terminal patterning is not affected in *dzy* and *rap1* GLC, either. For instance, *hkb* RNA is expressed at the anterior and posterior pole just like in wildtype (Fig. 3D–F), in contrast to earlier reports stating that *hkb* mRNA is reduced in *rap1* GLC (Mishra et al., 2005). The posterior midgut (PMG) invagination and the germ band extension commence in *dzy* or *rap1* GLC like in wildtype (Fig. 2, Video 1). This can easily be followed via movement of the pole cells as they are anchored to the epithelium of the PMG

primordium. In wildtype and in *dzy* and *rap1* GLC the pole cells initially move towards dorsal with essentially the same speed (Video 1). Consequently, some aspect of the cellular machinery that executes the shape changes during VFF specifically depends on Dzy and Rap1.

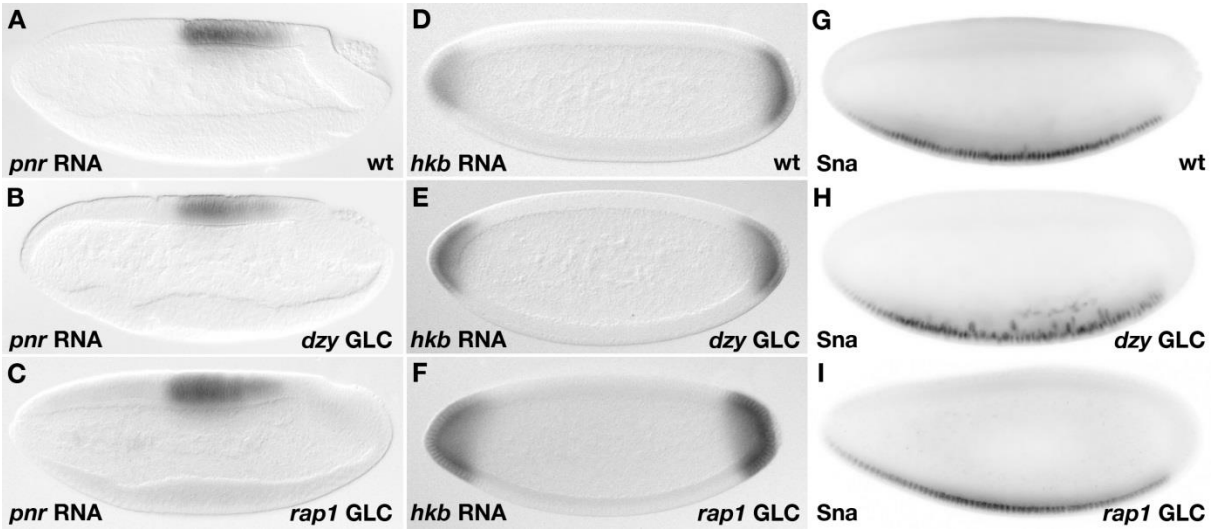

Fig. 3. Dorsoventral and anteroposterior axes are properly established in *dzy* and *rap1* GLC. A–C: *In situ* hybridization for *pnr* shows that the dorsal fate in *dzy* (B) and *rap1* GLC (C) is properly established in comparison to wildtype (A). **D–F**: Terminal patterning is normal in *dzy* (E) and *rap1* GLC (F) as *hkb* RNA localizes to the anterior and posterior end of the embryo like in wildtype (D). **G–I**: Antibody staining for Sna validates that the ventral fate is properly established in *dzy* (H) and *rap1* GLC (I), as compared to wildtype (G).

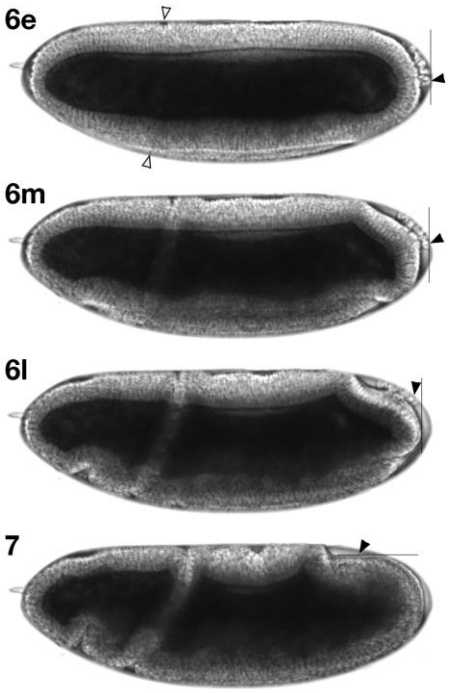

Fig. 4. Embryonic fine staging during ventral furrow formation. The sub-stages used in the manuscript are defined by the early movement of the pole cells. **Stage 6e**: The pole cells have not yet moved (arrowhead), but first signs of the cephalic furrow (between open arrowheads) are visible. **Stage 6m**: The cephalic furrow is clearly visible. The prospective PMG has flattened and moved the pole cells dorsally, but the most posterior cell of the embryos is still a pole cell. **Stage 6l**: The epithelium underlying the pole cells has adopted a convex shape and has moved further dorsally so that the pole cells are not any longer the most posterior cells of the embryo. **Stage 7**: The PMG invagination has deepened and moved anterodorsally so that the pole cells have reached a horizontal position. Time-intervals between images 250 sec.

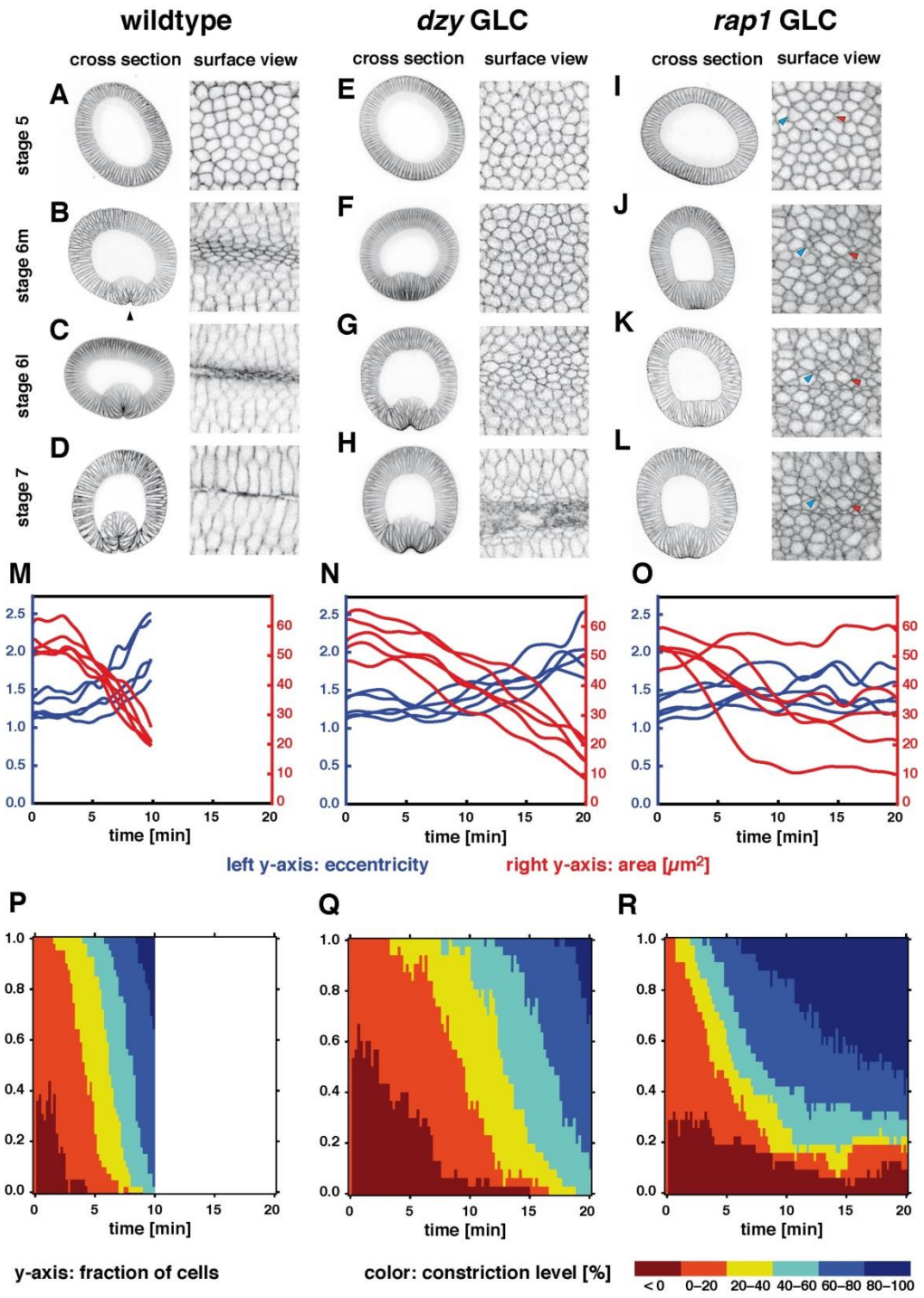

Fig. 5. Maternal loss of *dzy* or *rap1* affects constriction of ventral cells. A–L: Cross sections stained for Neurotactin (left) and stills of confocal live-imaging using Spider:GFP (right) of wildtype (A–D), *dzy* GLC (E–H) and *rap1* GLC (I–L). **Wildtype**: After completion of cellularization (A) cells from a mid-ventral band constrict their apices and the prospective mesoderm starts to invaginate, visible as an indentation in cross-sections (B, arrowhead). The indentation deepens (C) and the mesoderm has been entirely internalized into the ventral furrow by stage 7 (D). ***dzy*:** Cellularization proceeds normally (E), but cell constriction is severely delayed (F) leading to a slow-forming and non-persistent ventral furrow (G,H). ***rap1***: After normal cellularization (I) apical constriction occurs in a disperse pattern resulting in a random arrangement of constricted and unconstricted cells

(I–L, blue and red arrowheads, resp.), but the ventral furrow never forms. Cross-sections: ventral down; at 50% egg length. Surface views taken at 5 µm depth. **M–O**: Plots of apical area (red) and cell eccentricity (blue) over the first 20 minutes of gastrulation from 5 mid-ventral cells. In the wildtype, plots stop at 10 min when mid-ventral cells have been internalized. **P–R**: Histograms showing the time-dependent distribution of constriction levels among mid-ventral cells, coded by colour. Constriction levels indicate the amount of apical area decrease relative to time point 0 (100% constriction = reduction to zero area; 0% constriction = no change in area; <0% = area enlargement). In wildtype nearly all mid-ventral cells have reached strong constriction levels (60-100%) after 10 minutes. In *dzy* GLC the ventral epithelium needs about twice as long to achieve an equal fraction of constricted cells. In *rap1* GLC unconstricted or even bloated cells remain throughout gastrulation indicated by the red fractions.

For further analysis of the morphogenetic events of VFF in wildtype and mutant embryos we introduce a fine staging of stage 6 (Fig. 4): 6e (early), 6m (middle) and 6l (late). This staging is based on the movement of the pole cells indicating the progress of PMG invagination which is largely synchronous to the progress of VFF in wildtype and not affected in *dzy* and *rap1* GLC.

6.1.2 Apical constriction of ventral cells is compromised in *dzy* and *rap1* germline clones.

In wildtype, VFF is thought to be brought about by fast and extensive shape changes of ventral cells. To analyze possible alterations of these shape changes in *dzy* and *rap1* GLC, cell membranes were marked in cross sections of embryos immunostained for Neurotactin (Fig. 5A-L, respective left panels) or in surface views of live embryos expressing Spider:GFP (Fig. 5A-L, respective right panels). In wildtype, immediately after cellularization is completed, mid-ventral cells flatten apically and begin to constrict their apices. The apical constrictions are enhanced and the cells shorten in the apicobasal direction, thereby forming a tissue indentation (Fig. 5B). The indentation deepens (Fig. 5C) so that an epithelial tube is closed and fully internalized during stage 7 (Fig. 5D). In *dzy* GLC, mid-ventral cells flatten at stage 6m, but do not shorten leading to a high columnar epithelium (Fig. 5F). Apices are less

constricted than in wildtype, the furrow is shallow at stage 6l (Fig. 5G) and not completely closed at stage 7 (Fig. 5H).

The entire process of VFF is remarkably fast. In order to obtain a quantitative picture of the process of apical constriction and of the defects in *dzy* and *rap1* GLC, we tracked mid-ventral cells in time-lapse recordings of gastrulating embryos. In wildtype, apical cell area is quickly reduced. Within approximately 10 minutes all mid-ventral cells are strongly constricted and disappear into the furrow (Fig. 5M,P; Videos 1-3). Concomitant with total apical area reduction, mid-ventral cells become eccentric, i.e. they constrict noticeably less in anterior-posterior than latero-ventral direction (Fig. 21A; Fig. 5M, Video 2), probably due to asymmetric tension along both axes (Martin et al., 2010; see also section 6.2.3).

In *dzy* GLC, apical constriction is noticeably slowed down in mid-ventral cells, but still causes ventral cells to eventually develop a ventral furrow by reducing apical area and gaining eccentricity similar to wildtype (Fig. 5N,Q; Videos 1, 2). Strikingly, although a ventral furrow has finally formed after about double the time compared to wildtype, the furrow fails to close completely (Figs 2H') and even slightly opens up again (Video 3).

rap1 GLC show a more drastic phenotype. Apical constrictions do not take place evenly in the band of mid-ventral cells, but occur in an apparently disperse pattern. Most cells undergo strong area reduction, while others only constrict weakly, remain entirely unconstricted or become even bloated (Fig. 5I-L,O,R; Fig. 6; Videos 2,3). Often even higher constriction levels are reached in comparison to wildtype (Fig. 5P,R, dark blue fraction). However, wildtype cells might reach the same level of constriction, but at a time they have already disappeared into the furrow. Mid-ventral cells in *rap1* GLC stretch in apicobasal direction throughout stages 6 and 7 (Fig. 5J–L, see also Fig. 9G6l), but do not gain a markedly eccentric shape (Fig. 5O; Video 2). Despite the strong constriction of most mid-ventral cells

in *rap1*, the ventral epithelium does not form a furrow and the prospective mesoderm is not internalized (Fig. 5I-L; Videos 1-3).

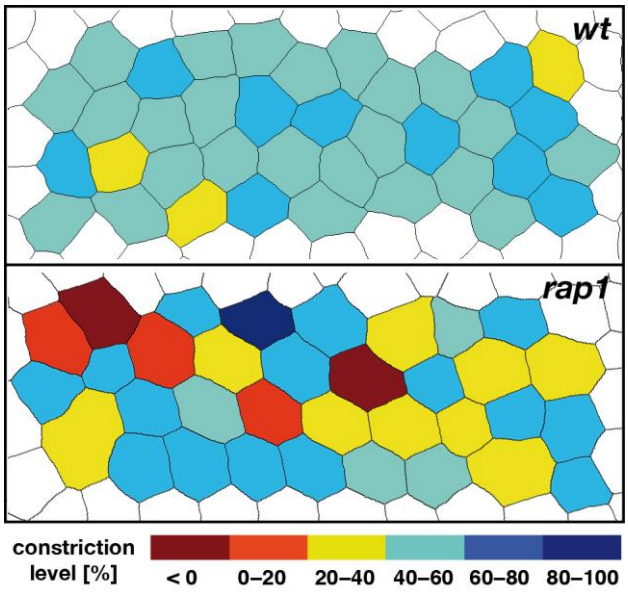

Fig. 6. Apical constriction occurs in a random spatial pattern in *rap1* GLC. Cell outlines from the ventral epithelium at the onset of gastrulation in wildtype and *rap1* GLC. Cell areas are coloured according to the level of constriction they reach within the next 10 minutes. The capability of executing apical constriction does not appear to follow a spatial pattern, but seems to be randomly distributed in the prospective mesoderm of *rap1* GLC.

Thus, loss of maternal Dzy results in lagging apical constrictions leading to a considerable slowdown and instability of the ventral furrow, while loss of maternal Rap1 renders apical constriction highly variable among mid-ventral cells and prevents formation of the ventral furrow.

6.1.3 Apical assembly and contraction of the actomyosin filament system is not affected in *dzy* or *rap1* germline clones.

For cell shape change to occur, an actomyosin filament system has to assemble and to contract while being tethered to the cell membrane in order to transmit the exerted force. As shown above, apical constrictions during VFF are compromised in *dzy* and *rap1* GLC, so we asked if the actomyosin filament system is properly localized and contractile in ventral cells.

In wildtype, non-muscle myosin heavy chain (MyoII) localizes to the furrow canals during cellularization (Young et al., 1991; compare Fig. 7A). While remaining basally throughout the dorsal and lateral epithelium, MyoII specifically relocalizes to the apex in ventral cells at the

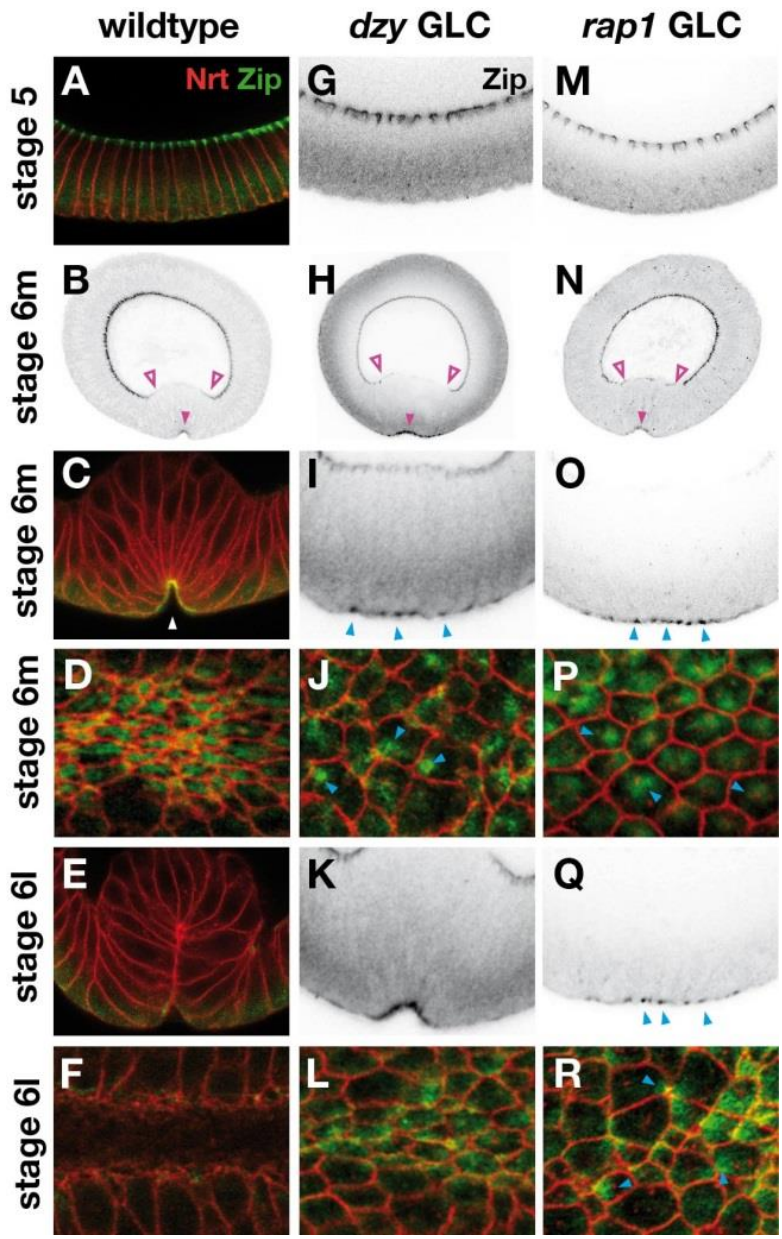

Fig. 7. The apical actomyosin meshwork is unaffected in *dzy* and *rap1* germline clones. Localization of MyoII (Zip) in wildtype (A–F), *dzy* GLC (G–L) and *rap1* GLC (M–R) shown in both cross-sections and surface sections. **Wildtype**. **A:** MyoII is localized to the cellularization front during stage 5. **B:** After completion of cellularization, MyoII disappears from the basal side (empty arrowheads) and relocalizes to the apex (arrowhead) in mid-ventral cells. **C:** Apical constriction takes place making MyoII appear as a contiguous band along apices of mid-ventral cells (arrowhead). **D:** Surface sections show coalesced MyoII within constricted cells. **E,F:** After invagination MyoII signal is diminished in internalized cells. ***dzy* & *rap1* GLC**. **G,M:** Localization of MyoII to the cellularization front is unchanged. **H,N:** Basal disappearance and apical relocalization in ventral cells also occur normally. **I,J,O,P:** MyoII coalesces (arrowheads), but is not in touch with cell membranes. **K,L:** In *dzy*, cells are eventually constricted during late gastrulation, and MyoII appears contiguous. **Q,R:** In *rap1*, coalesced MyoII appears discontiguous as cell constriction remains incomplete (arrowheads). Depth of surface sections: 2 µm. In *dzy* and *rap1* cross-sections (G, I, K, M, O, Q) the Nrt channel has been omitted for better visualization of MyoII.

onset of VFF. MyoII coalesces, concomitant with apical constriction of these cells, which gives MyoII a dense, contiguous appearance (Fig. 7B-D). After mesodermal cells have been internalized, signal intensity of MyoII quickly vanishes in these cells indicating that the actomyosin is disassembling (Fig. 7E,F).

In *dzy* and *rap1* GLC, the specific ventral relocalization of MyoII is unchanged: Like in wildtype, MyoII is present at the furrow canals during cellularization (Fig. 7G,M), before it specifically disappears from the basal side in ventral cells and localizes to the apex (Fig. 7H,I,N,O). The localization of the other structural component of the actomyosin filament system, F-Actin, is also unchanged in *dzy* and *rap1* GLC (data not shown). Furthermore, RhoGEF2, the key component conferring contractile actomyosin, is properly localized to the apices of ventral cells at early gastrulation in *dzy* and *rap1* GLC (Fig. 8). In *rap1* GLC, MyoII coalesces within mid-ventral cells during stage 6m (Fig. 7O,P, arrowheads). However, unlike wildtype (Fig. 7C,D), this coalesced MyoII appears largely detached from cell membranes since many cells are unconstricted.Also in stage 6l coalesced MyoII is visible in unconstricted

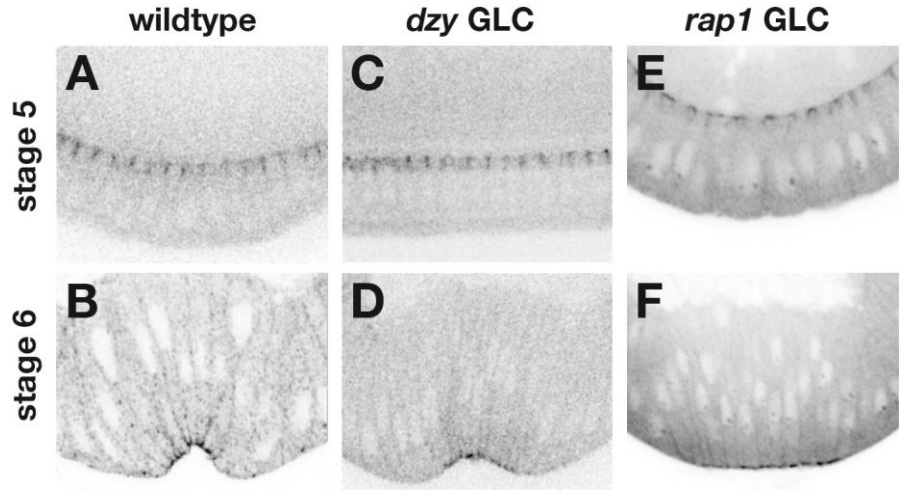

Fig. 8. RhoGEF2 is properly localized to apices of ventral cells in *dzy* and *rap1* GLC at the onset of VFF. Wildtype, *dzy* GLC and *rap1* GLC stained for RhoGEF2. **Stage 5:** During cellularization RhoGEF2 localizes basally to the cellularization front in wildtype (A), *dzy* GLC (C) and *rap1* GLC (E). **Stage 6:** At the onset of VFF, RhoGEF2 vanishes basally and accumulates in the apices of ventral cells (B). This apical accumulation is unaffected in ventral cells of *dzy* GLC (D) and *rap1* GLC (F).

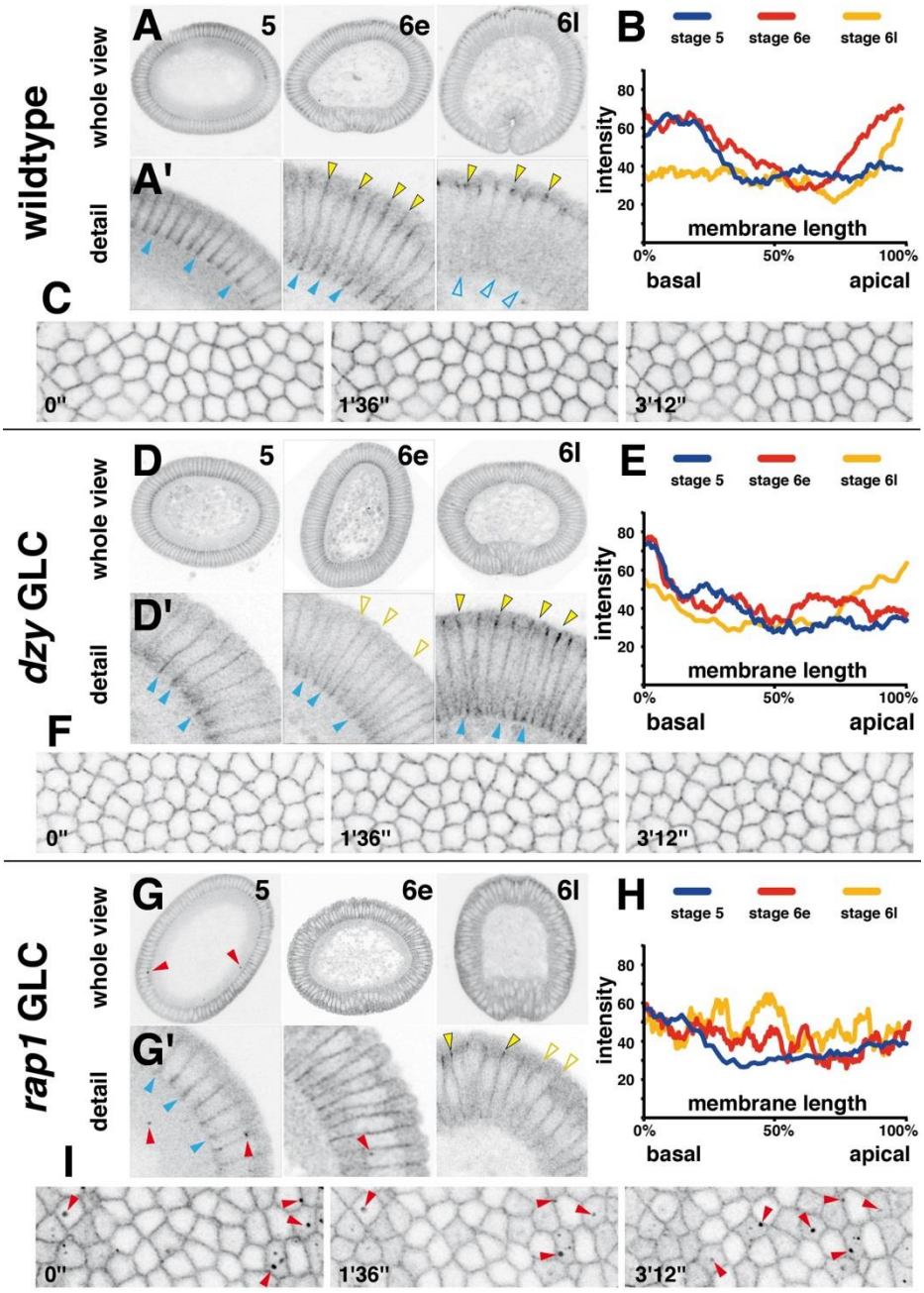

Fig. 9. Localization of DE-Cad to apical membranes is slowed down in *dzy* germline clones and largely defective in *rap1* germline clones. DE-Cad:GFP in fixed specimen (cross sections in A, A', D, D', G, G'; ventral down) and in live embryos (ventral surface views in C, F, I at 5 µm depth) as well as plots of DE-Cad:GFP intensity along membranes going from basal to apical in cross-sections of individual representative cells (B, E, H). **A, A':** In wildtype, DE-Cad is concentrated at the cellularization front during stage 5 (blue arrowheads). At the onset of gastrulation (stage 6e) an accumulation of DE-Cad is visible at the apical side (yellow arrowheads) while the basal accumulation is still present (blue arrowheads). In stage 6l the basal accumulation has vanished (blue empty arrowheads) while the apical accumulation has developed into a prominent belt around the entire

epithelium (yellow arrowheads). **B:** The basal peak in stage 5 indicates the localization of DE-Cad to the cellularization front (blue curve). At stage 6e the basal peak remains and another apical peak comes up (red curve). At stage 6l the basal peak has disappeared, but intensity strongly peaks in the apical domain (yellow curve). **D, D':** In *dzy* GLC, DE-Cad localizes normally to the cellularization front during stage 5 (blue arrowheads), but the emergence of an apical accumulation is not evident by stage 6e (yellow empty arrowheads) and is first visible in stage 6l (yellows arrowheads). Higher magnifications are provided separately in Fig. 12. **E:** DE-Cad intensity plots reveal normal basal localization during stage 5, but a missing apical peak in stage 6e (red) and a pertinent basal peak in stage 6l (yellow). **G, G':** In *rap1* GLC, DE-Cad localizes normally to the cellularization front during stage 5 (blue arrowheads), but appears diffuse at stage 6e. Apical accumulation only occurs locally at late gastrulation (stage 6l, compare filled to empty arrowheads). Instead, particles of DE-Cad can be detected, which are not restricted to membranes (red arrowheads). **H:** Intensity plots show an unaltered basal concentration during stage 5 (blue), but a highly disperse distribution at stage 6e (red). In stage 6l many cells still exhibit a disperse DE-Cad distribution, in particular the lack of apical accumulation (yellow). **C, F, I:** Stills of time-lapse movies starting at completion of cellularization, i.e. onset of gastrulation. In *rap1* GLC, conspicuous large particles of DE-Cad float through the cytoplasm (I, red arrowheads), which are not seen in wildtype (C) and *dzy* GLC (F). Varying cytoplasmic signal among different cells reflects varying apicobasal nuclear positions since nuclei move towards basal during the course of gastrulation (Kam et al., 1991; also see Fig. 10).

or incompletely constricted cells (Fig. 7Q,R, arrowheads), resulting in a discontiguous and torn impression. This coalesced MyoII indicates that the actomyosin filaments have contracted. Apparently not in all cells, however, does the actomyosin contraction efficiently pull along the membranes indicating compromised attachment of the cytoskeleton to cell membranes. Similar conclusions have been drawn in other studies which revealed coalesced MyoII in unconstricted cells (Dawes-Hoang et al., 2005; Martin et al., 2010; Sawyer et al., 2009). Also in *dzy* GLC, coalesced MyoII is evident within unconstricted cells at stage 6m (Fig. 7I,J, arrowheads). Only at later gastrulation cells finally constrict, and MyoII shows a contiguous appearance (Fig. 7K,L) that is similar to wildtype at an earlier time point of VFF.

Thus, we conclude that the actomyosin filament system is contractile in both *dzy* and *rap1* GLC since MyoII does coalesce. In *dzy* GLC, however, actomyosin possibly fails to properly

attach to cell membranes before late gastrulation. In *rap1* GLC, attachment seems to vary among mid-ventral cells, ranging from sufficiently functional to defective, resulting in a broad distribution of achieved constriction levels (Fig. 5R).

6.1.4 Accumulation of DE-Cad into an apical belt depends on Dzy and Rap1.

Adherens junctions (AJs) in epithelia are aggregates of DE-Cadherin (DE-Cad) that are coupled to the actin cytoskeleton and provide a membrane-anchor to the contractile actomyosin to allow cells to undergo shape changes. As actomyosin is correctly localized and appears functional, but does not seem capable of properly constricting ventral cells in *dzy* and *rap1* GLC, we investigated junction formation by means of DE-Cad:GFP, in both living and fixed specimen. During gastrulation DE-Cad undergoes characteristic changes in localization which occur likewise in ventral, lateral and dorsal cells. Due to the lack of morphological change, documentation is facilitated in lateral and dorsal cells (Fig. 9). The analogous events in ventral cells are documented in Fig. 11. In addition to the descriptions of qualitative changes in localization, we also measured pixel intensities along membranes going from basal to apical in order to put our observations about DE-Cad localization onto a quantitative basis (Figs. 9B,E,H; 11C,F,I).

Like MyoII, DE-Cad localizes to the ingressing cellularization front during stage 5 in wildtype, thus appearing basal in late stage 5 cross-sections (Fig. 9A5, A'5, B). Towards the end of cellularization DE-Cad starts to prominently accumulate in the apical domain around the circumference of the epithelium indicating the establishment of the apical adhesion belt at the onset of gastrulation (Figs. 9A6e, A'6e, B; 11A,C). As gastrulation proceeds, the remaining basal DE-Cad accumulation dissolves while the apical belt grows more pronounced (Fig. 9A6l, A'6l, B). Concomitantly with this apical junction assembly mid-ventral cells constrict their apices indenting the ventral epithelium (Figs. 9A6e; 11B,C). In previous

studies Armadillo (Arm; β-catenin) has also been shown to accumulate apically at the end of cellularization consistent with the set-up of the apical junction belt immediately prior to gastrulation (Dawes-Hoang et al., 2005; Hunter & Wieschaus, 2000). Ventral cells exhibit the same apical localization of DE-Cad at the end of cellularization as do lateral and dorsal cells (Fig. 11A-C); however, possibly since the apical cortex commences flattening in these cells, the dome-like eversions are missing in ventral cells letting DE-Cad appear more apical than in lateral and dorsal cells (compare Fig. 9A'6e to 11A; 9A'6l to 11B). Also, the basal accumulation is lost earlier in ventral cells (compare Fig. 9A'6e to 11A).

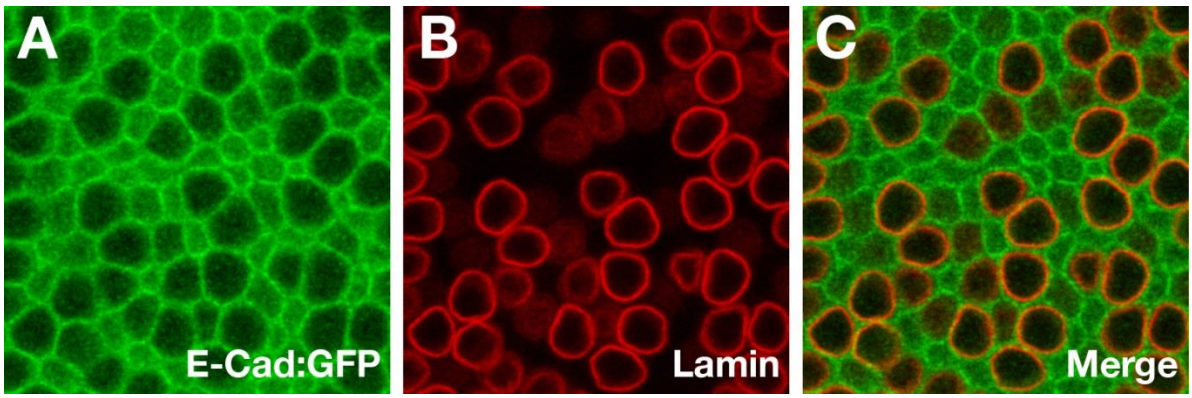

Fig. 10. Varying cytoplasmic DE-Cad signal reflects apicobasal position of the nucleus. Surface section (5 µm depth) through ventral cells of a *rap1* GLC expressing DE-Cad:GFP, stained for Lamin to mark nuclei at stage 6l. DE-Cad:GFP (A) shows heterogeneous cytoplasmic signal correlating with the position of the nucleus (B). Cytoplasmic signal vanishes where the section plane goes through a nucleus (C).

In *dzy* GLC, DE-Cad localizes basally during stage 5 in accordance with cellularization proceeding normally (Fig. 9D5, D'5, E). However, at the onset of gastrulation the establishment of apical junctions is delayed in the entire epithelium as apical accumulation of DE-Cad has not taken place by stage 6e (Fig. 9D6e, D'6e, E; Fig. 11D,F; Fig. 12) and is visible no earlier than stage 6l, accompanied by the first apical constrictions and tissue indentation (Fig. 9D6l, D'6l, E; Fig. 11E,F; Fig. 12).

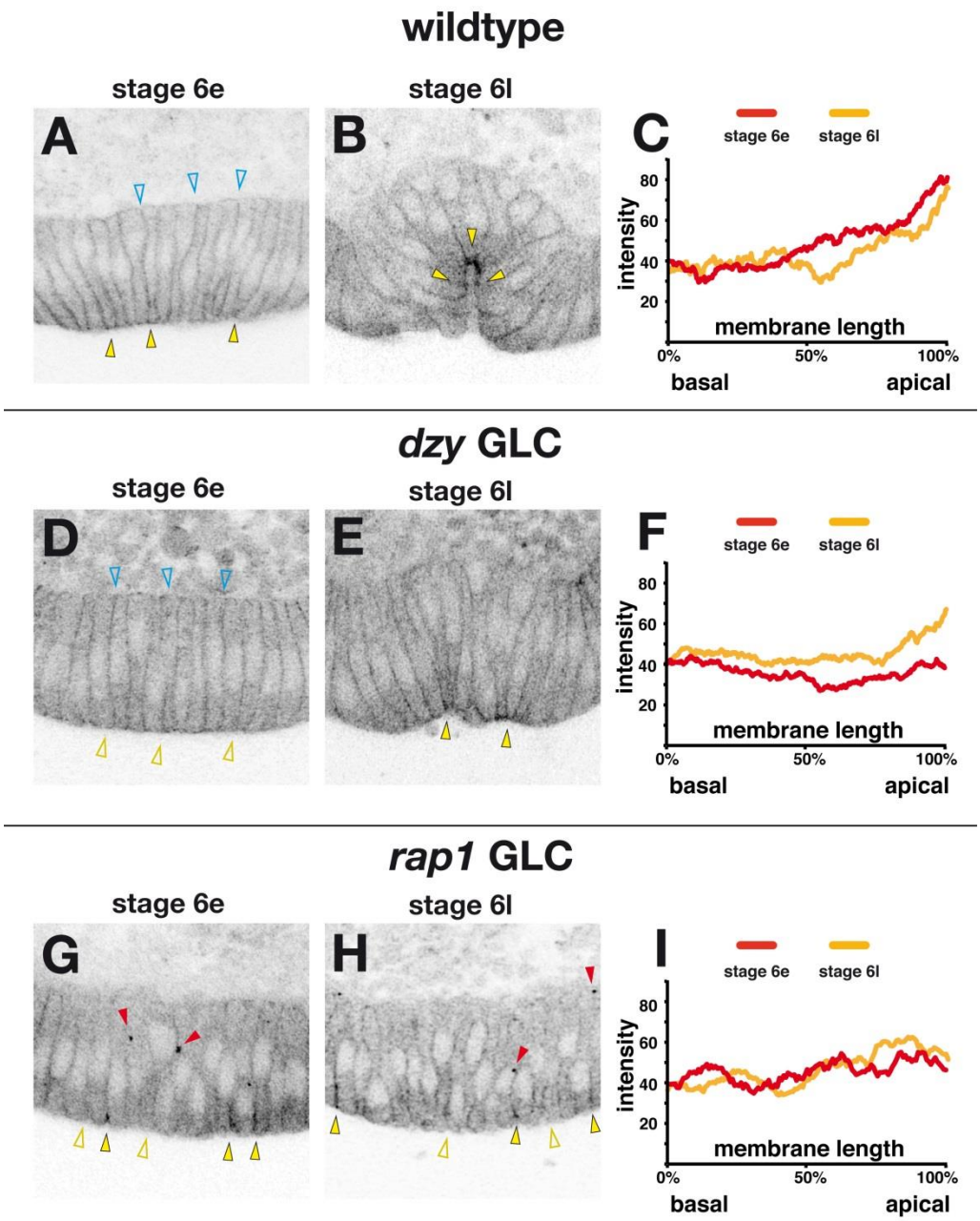

Fig. 11. Apical accumulation of DE-Cad is slowed down in *dzy* germline clones and occurs only fragmentarily in *rap1* germline clones. Ventral details of fixed specimen expressing DE-Cad:GFP (A,B,D,E,G,H). DE-Cad:GFP intensity plots along membranes going from basal to apical in individual representative ventral cells (C,F,I). Stage 5 has been omitted as events are identical to dorsal and lateral cells (see Fig. 9). **A:** In wildtype, DE-Cad accumulates apically at the onset of gastrulation (yellow arrowheads). Basal accumulation has vanished in ventral cells (blue empty arrowheads). **B:** Ventral cells undergo apical constriction with DE-Cad strongly accumulated apically (yellow arrowheads). **C:** Intensity plots show apical peaks at stage 6e (red) and 6l (yellow), but unlike in lateral and dorsal cells, a basal peak is missing at stage 6e in ventral cells. **D:**

In *dzy* GLC, the basal accumulation is lost like in wildtype in ventral cells (blue empty arrowheads), but apical accumulation is missing (yellow empty arrowheads) at stage 6e. **E:** In stage 6l apical accumulation begins to emerge in ventral cells (yellow arrowheads). **F:** Intensity profiles show the apical peak at stage 6l (yellow), which is still missing at stage 6e (red). Basal peaks are missing in ventral cells, like in wildtype. **G,H:** In *rap1* GLC, apical accumulation occurs only fragmentarily in a subset of ventral cells (yellow arrowheads) while being largely missing otherwise (yellow empty arrowheads). In addition, ectopic accumulations are visible in ventral cells (red arrowheads). **I:** Intensity profiles show a diffuse pattern in most ventral cells.

In *rap1* GLC, DE-Cad also localizes basally to the cellularization front (Fig. 9G5, G'5, H), but in addition, striking punctate ectopic accumulations of DE-Cad are evident in the cells (Figs. 9G,G'; 11G,H, red arrowheads). Also in confocal live-imaging peculiar DE-Cad:GFP rich particles can be seen floating through the cytoplasm in ventral, lateral and dorsal cells of the epithelium that are not found in wildtype or *dzy* GLC (Fig. 9C,F,I; Video 4). DE-Cad appears largely dispersed along lateral membranes and only fragmentary apical accumulation is evident, but a complete circumferential apical belt is not established (Figs. 9G,G',H; 11G-I). Interestingly, accumulation of the minor AJ component Arm (β-catenin) into an apical belt appears to be unaffected (Fig. 13).

We conclude that Dzy and Rap1 are not required for localizing DE-Cad to AJs at the cellularization front, but for its accumulation into an apical belt at the onset of gastrulation. This process is considerably slowed down in *dzy* GLC and largely defective in *rap1* GLC. As consequence, the cytoskeleton cannot attach to cell membranes during early gastrulation in *dzy* GLC since AJs are not in place yet. Thus, first actomyosin contractions are without effect on cell constriction. In *rap1* GLC, the AJ belt remains incomplete resulting in a varying capability of attaching the cytoskeleton, so actomyosin contractions lead to a varying degree of constriction among mid-ventral cells (Fig. 5R; Fig. 7).

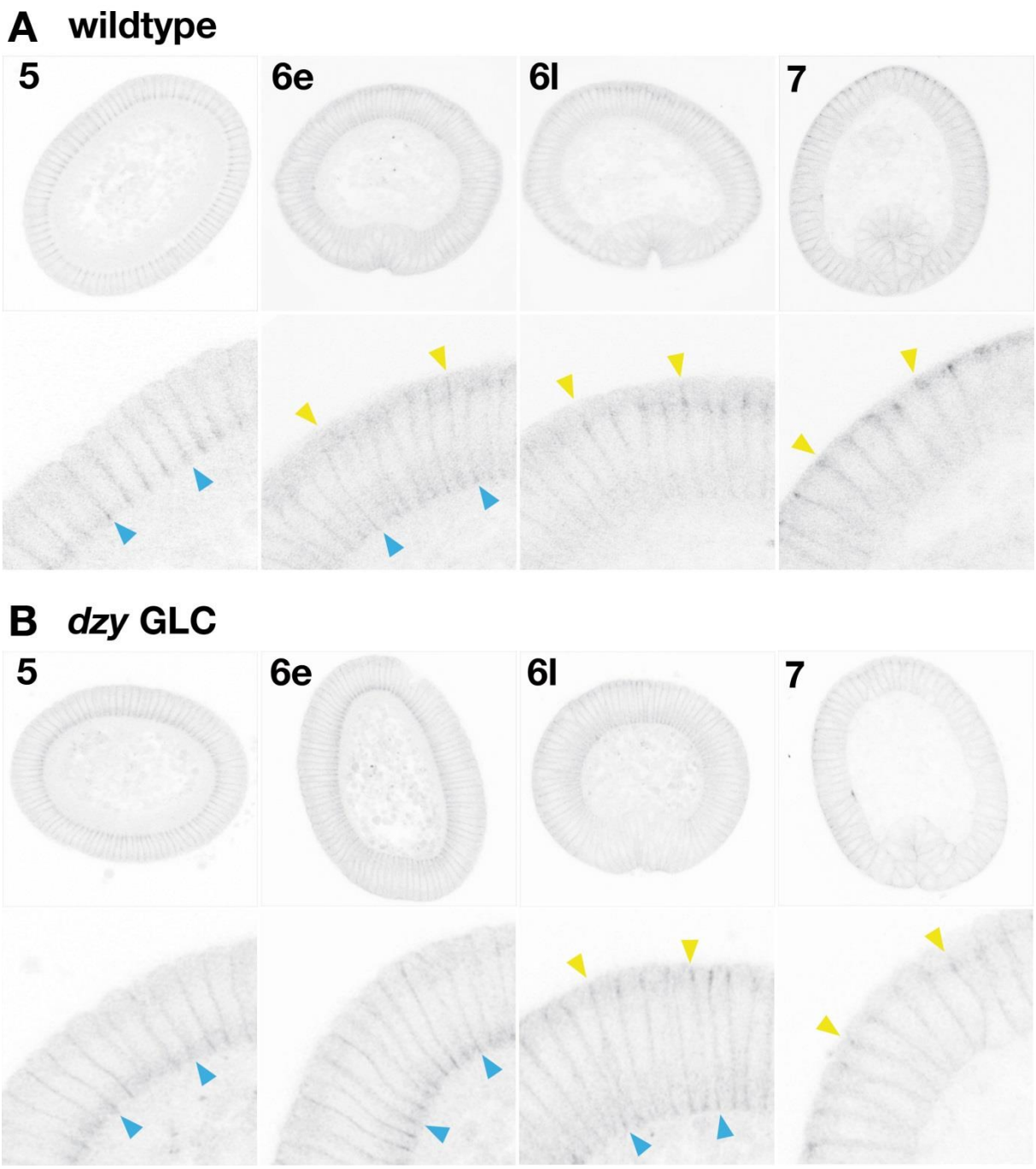

Fig. 12. Accumulation of DE-Cad into an apical belt is slowed down in *dzy* germline clones. Cross-sectioned embryos of wildtype (A) and *dzy* GLC (B) expressing DE-Cad:GFP in whole views and corresponding detail views. **Wildtype:** An apical accumulation of DE-Cad is visible at early gastrulation (A6e, yellow arrowheads), in addition to the basal accumulation representing the completed cellularization front (A6e, blue arrowheads). During the course of gastrulation this basal accumulation disappears and the apical accumulation grows into a prominent belt (A6l, 7). ***dzy* GLC**: The apical accumulation is missing at early gastrulation (B6e), but emerges belatedly during late gastrulation (B6l, yellow arrowheads) and also grows into an apical belt (B7, yellow arrowheads)

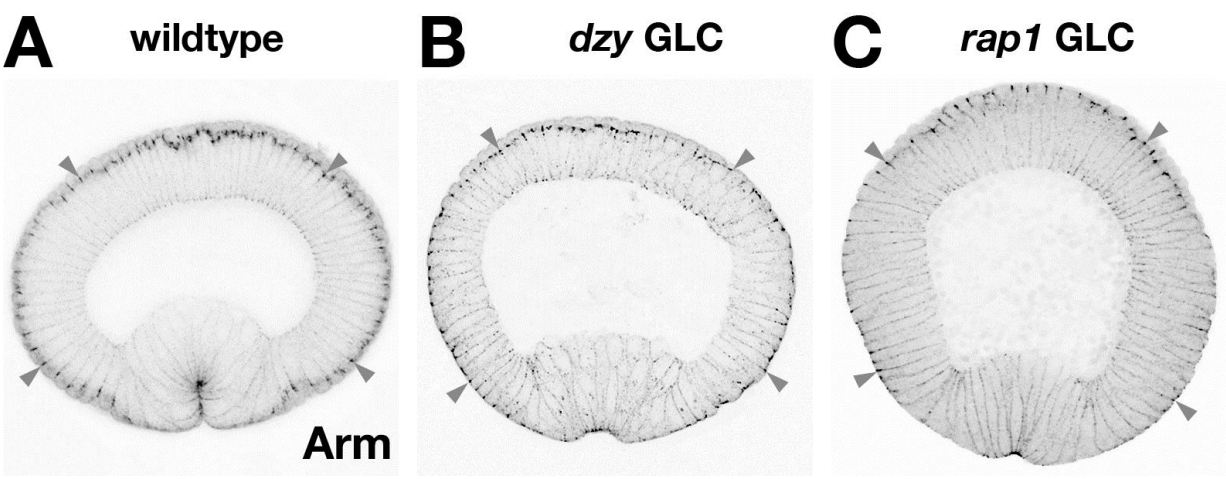

Fig. 13. Accumulation of Arm into an apical belt is not affected in *rap1* germline clones. Stage 6l cross-sections of wildtype, *dzy* and *rap1* GLC stained for Arm. Arm has formed a circumferential apical belt around the epithelium in *dzy* and *rap1* GLC (B, C, arrowheads) similar to wildtype (A, arrowheads).

6.1.5 3D reconstruction reveals abnormal cell shape change in *rap1* germline clones during ventral furrow formation

In addition to fixed cross-sections and live-recordings we also analyzed cell shape change during gastrulation using three-dimensional cell reconstruction. As noted above (Fig. 5I-L), maternal loss of Rap1 leads to an irregular arrangement of constricted and unconstricted cells in the ventral epithelium during gastrulation. 3D reconstruction reveals that the aberrant cell morphology seen in *rap1* GLC is not confined to the apical region: In those cells having achieved apical constriction, constriction is often not confined to the apex (like in wildtype) but spans far towards the basal end. Also, cells lacking apical constriction may be constricted further basal – a phenomenon not seen in wildtype cells, either (Fig. 14A,B: stage 6). As gastrulation proceeds, this phenomenon grows more dramatic with cells acquiring a slender, stalk-like appearance although the apical surface may or may not be constricted (Fig. 14A,B: stage 7). 3D reconstruction also tackles a long standing debate concerning the basal movement of nuclei associated with apical constriction in ventral cells: It had been suggested

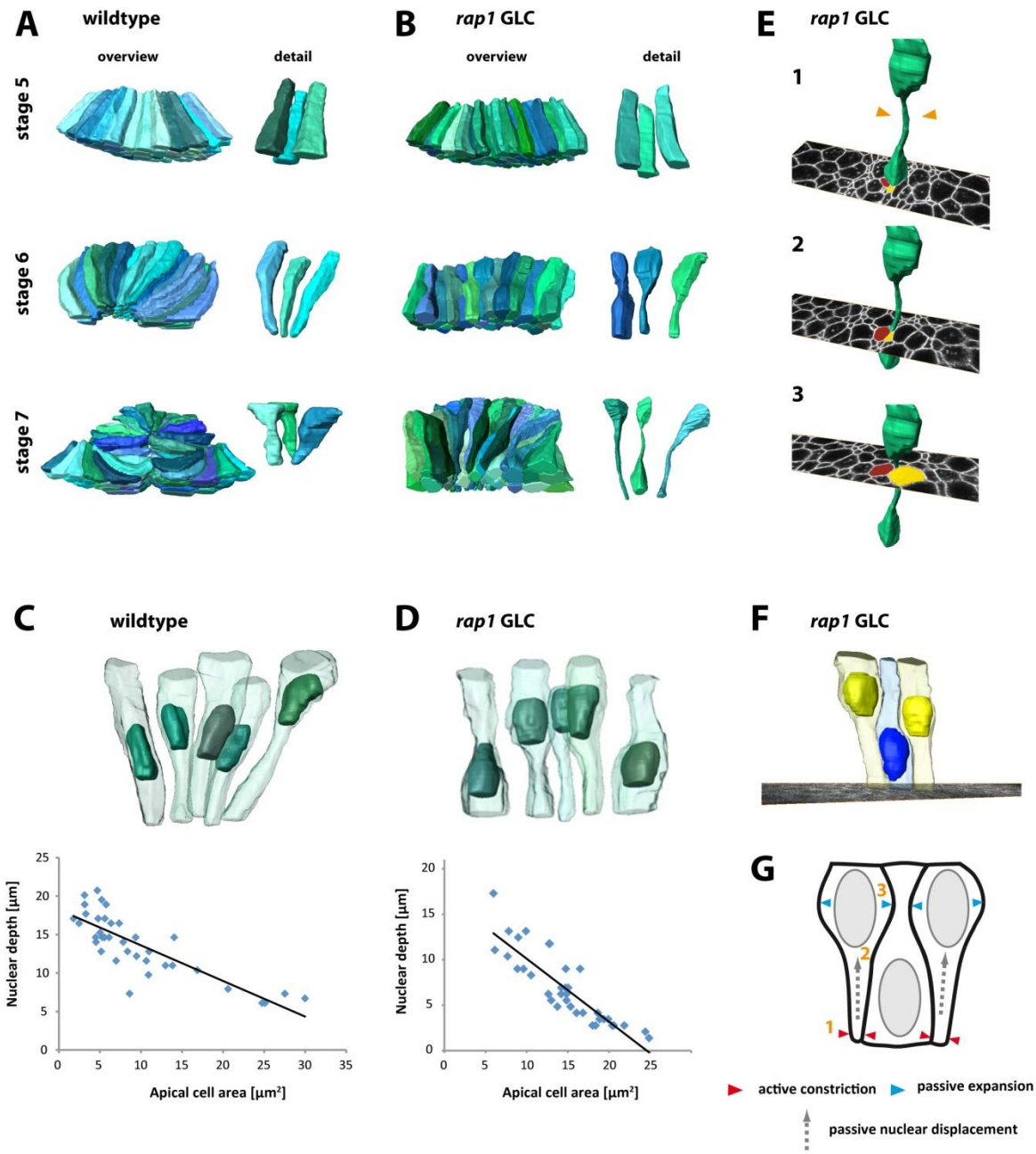

Fig. 14. Cell shape change during ventral furrow formation. 3D reconstructions of ventral cells obtained from confocal image stacks. **A:** In wildtype, cells have a columnar shape at the end of cellularization (stage 5). During gastrulation cell apices are constricted giving ventral cells the appearance of acuminate tubes (stage 6). After ventral cells have invaginated (stage 7), they shorten in the apicobasal axis, changing from a tube into a wedge shape. **B:** In *rap1* GLC, cellularization is unaffected with cells having a normal columnar shape (stage 5). During

gastrulation some cells have a constricted apex, but ectopic constriction is often seen further basal (stage 6). At late gastrulation, most cells have become slender and stalk-like but only a subset has a constricted apex (stage 7). **C,D:** 3D reconstructions of both cell outlines and cell nucleus obtained from confocal image stacks of double-labelled embryos (stage 6). Apical cell area negatively correlates with nuclear depth (= apicobasal distance of the nucleus from the cell apex). **E:** Ectopic constriction (green cell: arrowheads in (1)) in *rap1* GLC is accompanied by extended diameters of adjacent cells (red and yellow) in the same plane (3). **F:** 3D reconstruction of nuclei shows that ectopic constriction occurs in cells with basally displaced nuclei in their neighbour cells. **G:** Model of ectopic constriction seen in *rap1* GLC. As some cells manage to actively constrict their apex (1), the nuclei become passively displaced towards the basis in these cells (2). As a result, the basal side swells and squeezes the basis of a neighbouring cell that failed to constrict its apex so the nucleus remains at the apical side (3).

that apical constriction and nuclear apical-to-basal movement be independent processes (Leptin & Grunewald, 1990). However, since the reduction of apical cell surface area clearly correlates with nuclear basal depth and no instance is observed where the nucleus has moved basal although the apex has remained unconstricted (Fig. 14C,D), our data strongly argue in favour of a passive nuclear movement towards the cell basis. This would lead to a parsimonious model by which the nucleus becomes passively displaced towards the basal end when the cell constricts its apex. The same conclusion was drawn in a recent study using a very similar methodology (Gelbart et al., 2012).

Since myosin is normally localized to the cell apices in *rap1* GLC (Fig. 7M-R), the ectopic, more basal constriction seen in many cells (Fig. 14B,E) is unlikely to be a consequence of active cell contraction. Instead, it is probably a passive compression caused by basally shifted nuclei in neighbouring cells. Since a subset of cells manages to constrict the apex, the nuclei are pushed towards the basal side in these cells squeezing adjacent cells which failed to constrict apically and, consequently, have the nucleus still at the apical side (Fig. 14E-G). In *dzy* GLC, 3D reconstructions do not differ from wildtype (not shown), apart from exhibiting a considerable slow-down in passing the stages of gastrulation, as described above (Figs. 9, 12).

6.1.6 The *rap1* phenotype can be partially rescued by blocking endocytosis

In mammalian cell culture, Rap1 has been implicated in the stabilization of E-cadherin aggregates in the membranes by facilitating the binding of p120-catenin to E-cadherin, thus preventing its endocytosis (Hoshino et al., 2005). Since the floating DE-cadherin:GFP particles observed in *rap1* GLC (Fig. 9I; Video 4) possibly represent endocytic vesicles indicating unstable membrane integration of DE-Cad, we sought to rescue the *rap1* phenotype by blocking endocytosis. A heat-sensitive *shibire* allele *(shi^{ts})* effectively inhibits dynamin-mediated endocytosis in *Drosophila* when shifted to the restrictive temperature of 32°C (Levayer et al., 2011), but unfortunately, we did not succeed in creating a *shi; DE-Cad:GFP; rap1 FRT/TM3* fly stock since a critical intermediate genotype did not prove viable. Instead, we attempted to block endocytosis in *rap1* GLC through the application of drugs. Following a recently published procedure (Rand et al., 2010) we developed a protocol to permeabilize young *Drosophila* embryos through application of a limonene containing wash buffer. Incubating cellularizing embryos in this buffer made them permeable to medium sized molecules, such as rhodamine (479 Da) or chlorpromazine (319 Da), while maintaining full viability (Fig. 15B). Chlorpromazine is a blocker of clathrin-mediated endocytosis and has been used in *Drosophila* to rescue phenotypes related to increased endocytosis (Levayer et al., 2011). Application of chlorpromazine had noticeable effects as the number of floating DE-Cad:GFP particles was significantly reduced (Fig. 15A). The failure to undergo cell constriction and to form a proper ventral furrow could not be rescued, however, even if higher chlorpromazine doses were applied (not shown). Filipin, a blocker of COPII-mediated endocytosis, had no rescuing effect on the furrow phenotype, either (not shown).

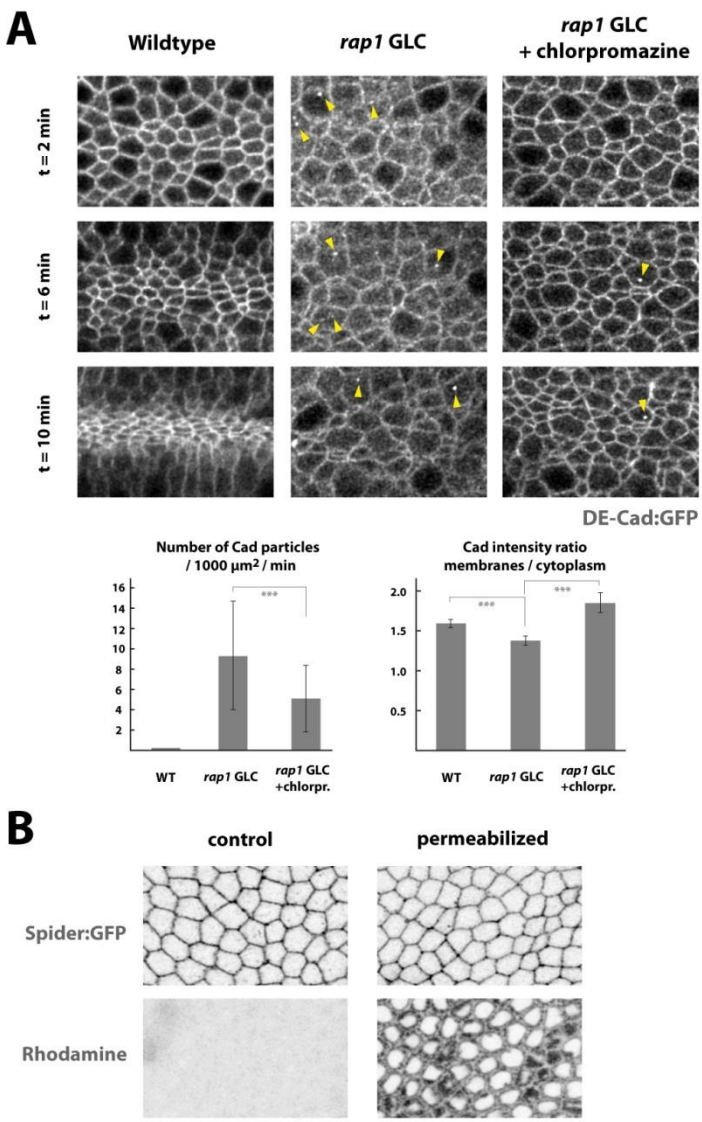

Fig. 15. Chlorpromazine alleviates but does not rescue the *rap1* phenotype. A: DE-Cad:GFP in live-recordings of gastrulating wildtype, *rap1* GLC and *rap1* GLC treated with 200 µM chlorpromazine. *rap1* GLC show floating DE-Cad:GFP particles in the cytoplasm (arrowheads) and overall increased levels of DE-Cad:GFP intensity in the cytoplasm (relative to membrane). Chlorpromazine treatment significantly decreases particle number and decreases DE-Cad:GFP intensity in the cytoplasm (relative to membrane), but does not rescue defective apical constriction and the failed ventral furrow. **B:** Intracellular rhodamine signal was used to assess successful permeabilization of embryos. Embryos were incubated in 1 mM rhodamine after incubation in Lemon3 solution (right) or PBS (left).

6.1.7 Dzy and Rap1 both localize cortically prior to ventral furrow formation, but are strongly reduced in invaginated cells.

Dzy and Rap1 have both been found to localize to AJs during later developmental events (Boettner & Van Aelst, 2007; Knox & Brown, 2002; Wang & Hartenstein, 2006). Here, we were interested in the subcellular localization of Dzy and Rap1 immediately prior to and

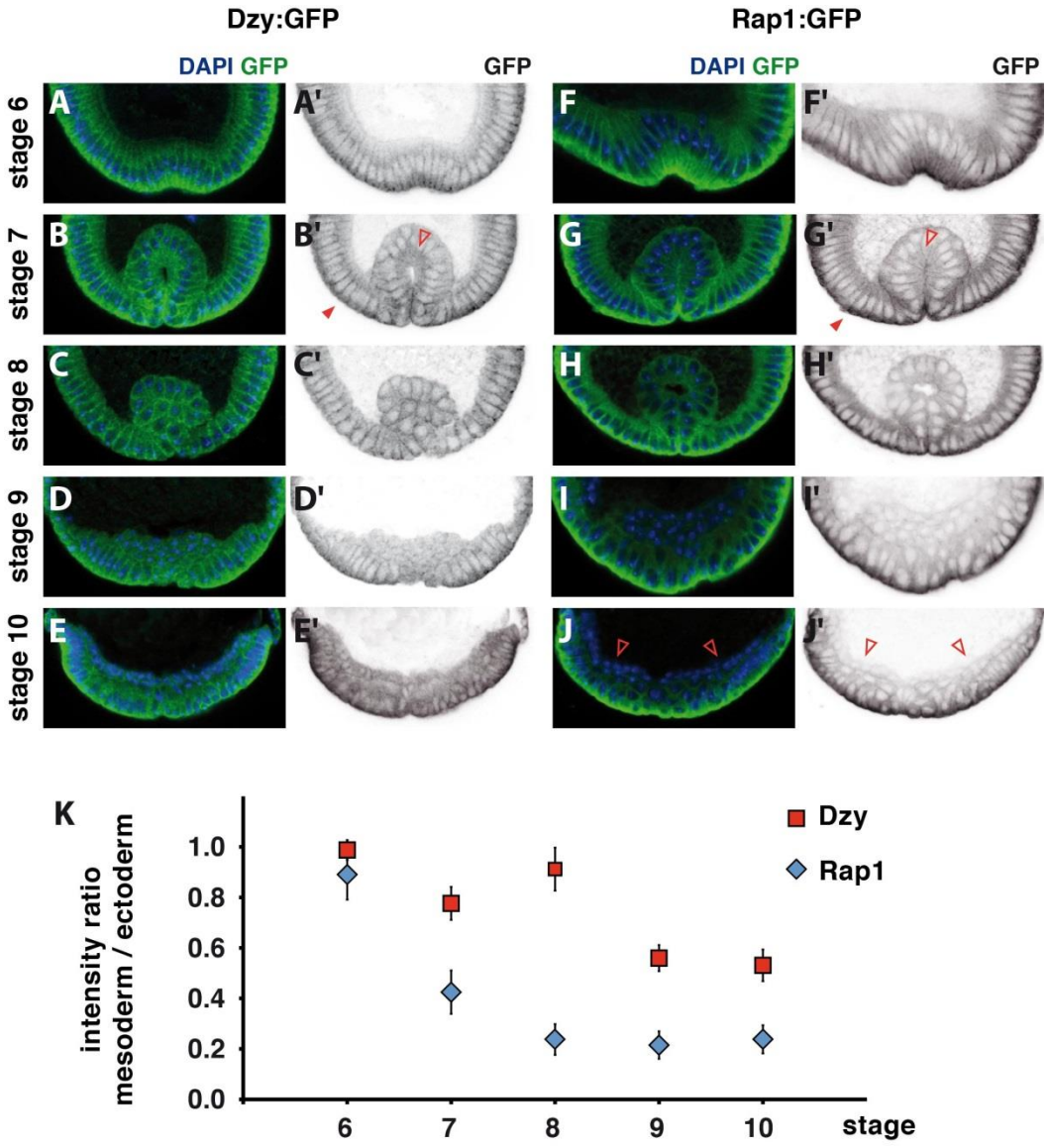

Fig. 16. Both Dzy and Rap1 localize to the cortex during ventral furrow formation, but fade in internalized cells. A-J': Localization of Dzy:GFP (A–E') and Rap1:GFP (F–J') during stages 6-10, detected by anti-GFP staining. At the onset of VFF both Dzy and Rap1 are concentrated in the cortex of cells around the entire epithelium (A,A',F,F'). As soon as the mesoderm has been invaginated in stage 7, levels of both proteins starts to fade in cells that have completed internalization (B,B',G,G', empty vs. filled arrowheads). Intensity further declines during stages 8-10 when the mesodermal tube collapses and cells migrate towards dorsal on the ectoderm (C–J'). Rap1 shows a stronger decrease compared to Dzy rendering the mesoderm almost invisible in the GFP-channel (arrowheads in J,J'). Both proteins remain strongly concentrated in the cortices of ectodermal cells. **K:** Graph showing the normalized mean GFP-intensity in the mesoderm (normalized to the ectoderm). Essentially starting at an 1:1 ratio at stage 6 both relative intensities have strongly declined by stage 10.

during gastrulation. As gastrulation starts, both proteins are distributed along the lateral cell membranes in all cells of the epithelium but concentrate in the cortex (Fig. 16A,A',F,F') in agreement with a role in apical AJ establishment as well as previous findings (Sawyer et al., 2009). Intriguingly, while this cortical enrichment remains present in the ectoderm throughout and after gastrulation, both Dzy:GFP and Rap1:GFP signals start to fade in mesodermal cells as soon as these have been internalized in stage 7 (Fig. 16B,B',G,G',K). Later the signal intensity further decreases in mesodermal cells, but is maintained in the ectoderm (Fig. 16C-E',H-J'). By stage 10 the relative mesodermal intensity has fallen by 40% for Dzy and by 80% for Rap1 (Fig. 16K), indicating that both protein levels decrease considerably in the mesoderm after VFF has been accomplished.

Thus, Dzy and Rap1 are similarly localized cortically in the epithelium from stage 6 onwards consistent with being involved in the set-up and possibly in the maintenance of epidermal apical AJs. Conversely, both proteins are substantially reduced in internalized cells of the prospective mesoderm. This raises the question whether the down-regulation of Dzy and Rap1 is relevant for further development of the mesoderm, in particular for its mesenchymal properties.

6.1.8 The diminishment of Dzy and Rap1 is required to allow mesodermal migration.

After completion of VFF the internalized mesoderm quickly loses its epithelial character and undergoes epithelial-to-mesenchymal transition (EMT): The invaginated tube collapses and cells lose their tight adhesion to each other. After EMT, the cells migrate towards dorsal on the ectoderm, forming a monolayer during stage 9 to 10 (Figs. 16C-E; 17A). This process is accompanied by the loss of AJs and the diminishment of DE-Cad (Oda et al., 1998).

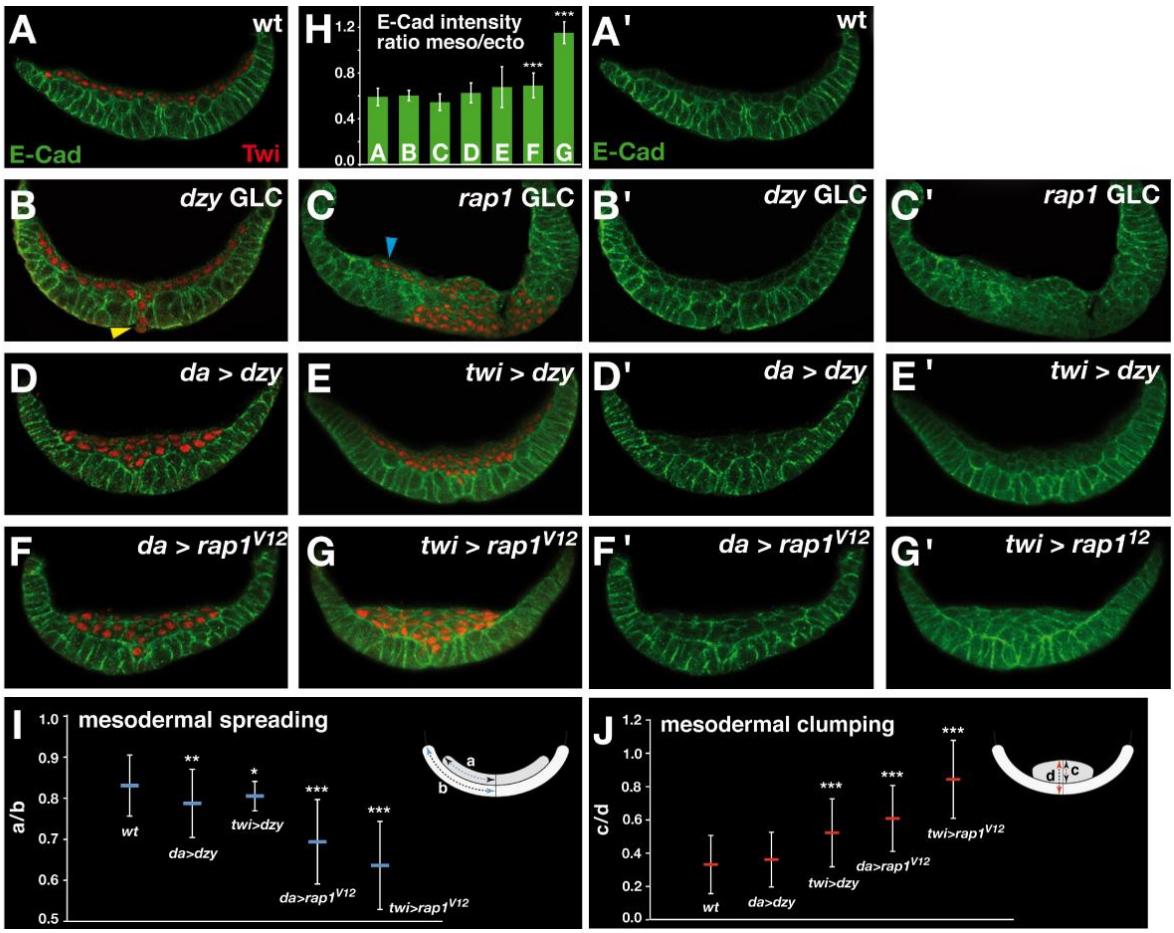

Fig. 17. Overexpression of Dzy or constitutively active Rap1 impairs mesodermal migration. **A–G**: Morphology of the invaginated mesoderm (marked by Twi) in stage 10 embryos of wildtype, *dzy* GLC, *rap1* GLC and upon overexpression of Dzy or constitutively active Rap1^{V12} by means of *da::gal4* or *twi::gal4* drivers (for better visual assessment of DE-Cad intensity the red channel has been omitted in A'-G'). **A**: In wildtype, the invaginated tube has collapsed and mesodermal cells have spread towards dorsal along the ectoderm forming a monolayer. **B**: In *dzy* GLC the mesoderm has spread towards dorsal and formed a normal monolayer although a minor part has not been internalized (yellow arrowhead). **C:** In *rap1* GLC the major part of the mesoderm is not internalized. A small internalized fraction shows unaffected monolayer formation (blue arrowhead). **D,E**: When Dzy is overexpressed ubiquitously (D) or in the prospective mesoderm only (E), the mesoderm fails to fully spread and often does not form a monolayer. **F,G**: Upon overexpression of Rap1^{V12} this phenotype is even stronger; the mesoderm shows pronounced clumping and defective monolayer formation. **H**: Plots of normalized DE-Cad intensity in the mesoderm (normalized by ectoderm) for the genotypes shown in A–G. Rap1^{V12} overexpression yields significantly elevated levels of DE-Cad intensity in mesodermal cells. **I,J:** Quantification of the non-monolayer phenotypes upon Dzy or Rap1^{V12} overexpression. Mesodermal spreading was measured by relating the mesodermal extension along the ectoderm (a) to the full stretch from the ventral most point to the

amnioserosa within the ectoderm (b). Mesodermal clumping was quantified by relating the thickness of the mesoderm (c) to the thickness of mesoderm plus ectoderm (d) above the ventral most point of the embryo.

Dzy and Rap1 are involved in the establishment and possibly the maintenance of the apical adhesion belt in epithelial cells, but on the other hand their expression level quickly decreases in the more motile mesodermal cells. Therefore, we wondered if the diminishment of Dzy or Rap1 is a requirement for EMT and subsequent mesenchymal migration. We ectopically expressed Dzy or the constitutively active form $Rap1^{V12}$ ubiquitously or specifically in the mesoderm. In both cases no effects are observed prior to or during VFF, but after EMT subsequent migration and monolayer formation of mesenchymal cells are affected considerably. Mesodermal cells show clumping and reduced spreading by stage 10, causing the cells to line up in several layers (Fig. 17D-G,I,J). In case of ectopic expression of constitutively active Rap1 these morphogenetic defects are accompanied by significantly elevated relative levels of DE-Cad in mesenchymal cells (Fig. 17H). Thus, ectopic activity of Rap1 maintains DE-Cad and thereby possibly strengthens cell-cell-adhesion. We do not find mesodermal migration to be defective in *dzy* GLC (Fig. 17B) or, unlike previously reported (McMahon et al., 2010), in *rap1* GLC (Fig. 17C). As observed in other VFF mutants, the mesoderm has the capability to move inside the embryo even though VFF is affected (Seher et al., 2007; Seher & Leptin, 2000). This indicates that a normal invagination is not essential for mesoderm internalization. Indeed, in *dzy* GLC the bulk of the mesoderm has been internalized by stage 10, in spite of the VFF defects, and shows normal monolayer formation. Only a minor fraction remains outside (Fig. 17B, arrowhead). In *rap1* GLC the ventral furrow phenotype is more severe, the overwhelming majority of the prospective mesoderm has not been internalized and broadly separates right and left of the neuroectodermal primordia (Fig. 17C). Only a small fraction has reached the interior, but this fraction seems to have normal mesenchymal properties as cells form a regular monolayer (Fig. 17C, arrowhead).

We propose that ectopic presence of Dzy or of constitutively active Rap1 in invaginated mesodermal cells is sufficient to affect mesenchymal development by impairing cell spreading, possibly due to increased cell-cell adhesion. We deduce that the reduction of Dzy and active Rap1 is necessary for mesodermal cells to allow for efficient migration and monolayer formation.

We conclude that Rap1 plays a pivotal role in the establishment and possibly also the maintenance of adherens junctions during embryogenesis in the sense that the presence or absence of Rap1 is critical to assemble or to disassemble adherens junctions, respectively, probably through regulation of DE-Cad endocytosis. Being a GEF for Rap1, Dzy plays a similar role in junction regulation, but considering the obvious discrepancy between the *dzy* and *rap1* phenotypes, alternative GEFs must work on Rap1 to take effect during gastrulation and are promising objects for further investigation.

6.2 A computational model of ventral furrow formation

In this section we adopt a so-called 2D vertex model to simulate the formation of the ventral furrow. We show that the ventral furrow can be well reproduced by a simple biophysical model. The model suggests that cells undergo apical constriction following a gradient of contractility in the ventral epithelium which renders cells more contractile the closer they lie to the ventral midline. The model predicts previous experimental findings, such as the gain of eccentric morphology of constricting cells and an incremental fashion of apical cell area reduction. Analysis of the model indicates that this incremental area reduction is a natural consequence of the physical constraints when cells in a mechanically coherent epithelium execute stochastic contractions. We underpin results from the model through *in vivo* analysis of ventral furrow formation in wildtype and *twi* mutant embryos. Our results show that ventral

furrow formation can be accomplished as a "tug-of-war" between stochastically contracting, mechanically coupled cells and may require less rigorous regulation than previously thought.

6.2.1 A vertex model of ventral furrow formation

We aimed at building a computational model that would allow direct visual and quantitative comparison to confocal live-recordings taken in surface view. Critical events associated with furrow formation (actomyosin contraction, adherens junction assembly, apical constriction) take place at the apical side of ventral cells, so imaging in surface view was frequently used as the method of choice to investigate the cell biological mechanisms of ventral furrow formation (e.g.: Martin et al., 2010; Martin et al., 2009; Oda & Tsukita, 2001; Roh-Johnson et al., 2012; Sawyer et al., 2009). In order to construct a model, key physical properties of epithelial cells must be mathematically described. The ventral epithelium is modelled in a surface view as a sheet of hexagonal cells (Fig. 18A). Cells are considered elastic, i.e. dilating or compressing the cell surface requires physical force (Fig. 18B: a), and cell membranes are under tension (Fig. 18B: b). Also, dilating or compressing cell edges requires physical force due to the underlying actin cytoskeleton (Fig 18B: d). During ventral furrow formation cells are supposed to be contractile, i.e. they apply force to reduce their surface area (Fig. 18B: c). Other than in previous variants of this vertex model we let contractile energy depend on cell area rather than cell perimeter since actomyosin contractions during ventral furrow formation have been shown to occur across the apical cell surface and are not restricted to a circumferential actomyosin ring (Martin et al., 2009). These four force contributions (area elasticity, line tension, contractility and line elasticity: Fig. 18B) are added for all cells in the sheet to obtain a so-called energy function which describes the total energy in the sheet at a certain time-point (Fig. 19B). In general, cells will aspire to take on a a morphology that yields the most favourable physical configuration, i.e. the lowest total energy. Similar models

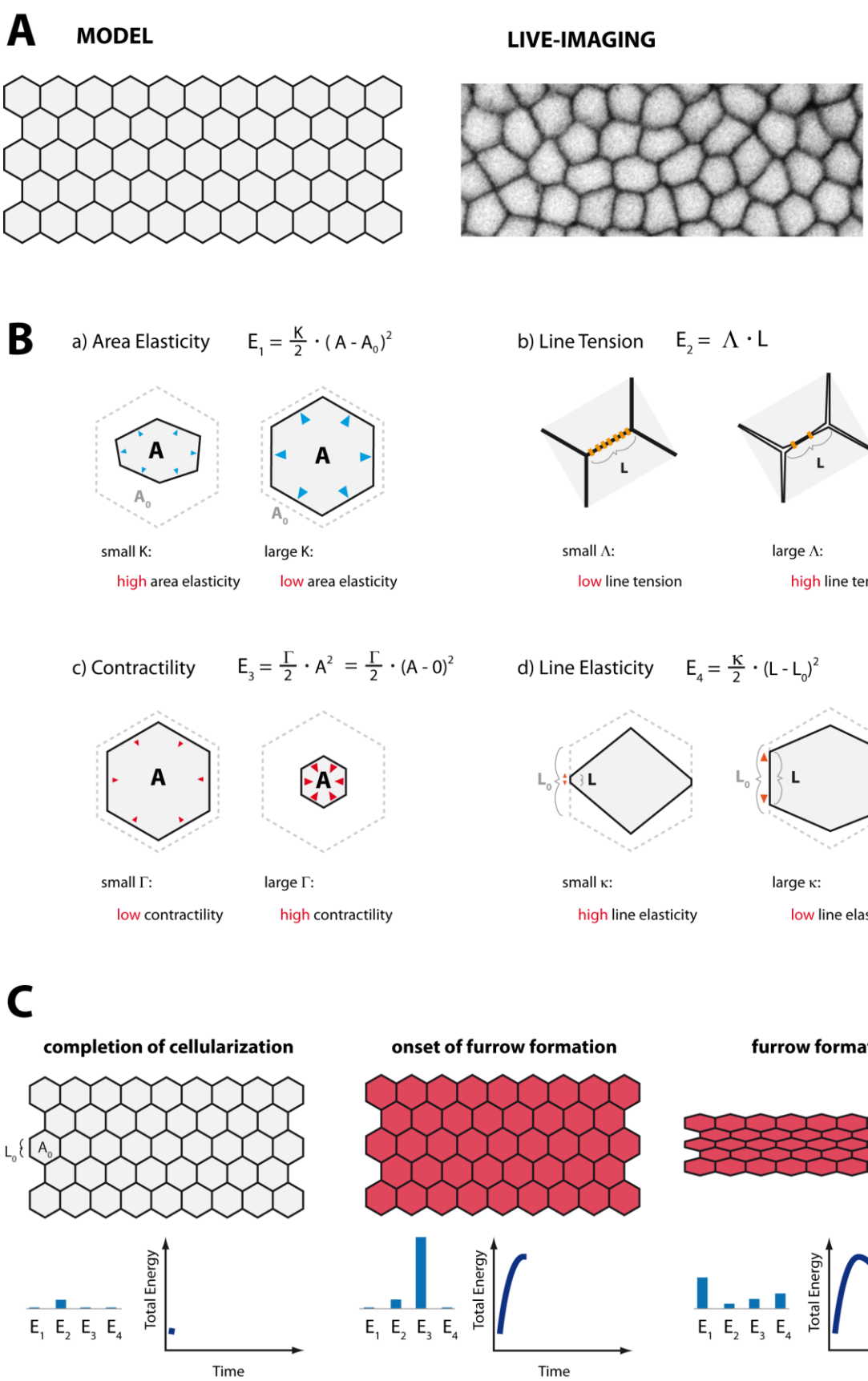
A
MODEL
LIVE-IMAGING
B
a) Area Elasticity $E_1 = \frac{K}{2} \cdot (A - A_0)^2$
b) Line Tension $E_2 = \Lambda \cdot L$
A
A_0
L
small K:
high area elasticity
large K:
low area elasticity
small Λ:
low line tension
large Λ:
high line tension
c) Contractility $E_3 = \frac{\Gamma}{2} \cdot A^2 = \frac{\Gamma}{2} \cdot (A - 0)^2$
d) Line Elasticity $E_4 = \frac{\kappa}{2} \cdot (L - L_0)^2$
L_0
small Γ:
low contractility
large Γ:
high contractility
small κ:
high line elasticity
large κ:
low line elasticity
C
completion of cellularization
onset of furrow formation
furrow formation
E_1 E_2 E_3 E_4
Total Energy
Time

Fig. 18: Biophysical model of ventral furrow formation (I). A: The ventral epithelium is modelled as a sheet of hexagonal cells. **B:** a) Area elasticity describes the cell's resistance against compression or dilation of its surface area brought about through the cytoskeleton underlying the cell cortex. Depending on the assumed elasticity parameter K, the cell is compressed/dilated more or less easily. When the cell has its preferred surface area A_0, the elastic energy E_1 equals zero, and the cell cortex is in a relaxed condition. K is assumed constant in this model. b) Line tension (strictly spoken, only Λ should be referred to as line tension since $E_2 = \Lambda \cdot L$ is an energy) describes the one-dimensional representation of surface tension of the cell membrane. Line tension can decrease with increased cell-cell adhesion brought about through adherens junctions. Λ is assumed constant in this model. c) Contractility describes the cell's attempt to reduce surface area via contraction of the subcortical actomyosin (i.e. with respect to contractility, the preferred area equals zero). The strength of contractility depends on the assumed contractility parameter Γ. Γ is allowed to vary in time and among different cells (Fig. 19D,E). d) Line elasticity describes resistance of cell edges against compression or dilation brought about through the cytoskeleton underlying the lateral cell membranes. Depending on the assumed elasticity parameter κ, cell edges are compressed/dilated more or less easily. When cell edges have their preferred length L_0, the elastic energy E_4 equals zero, and the edges are in a relaxed condition. κ is assumed constant in this model. - To calculate the total energy in the sheet at a certain time-point, these four energy contributions of all cells in the sheet are added up (Fig. 19B). **C:** At completion of cellularization the cell sheet is assumed to be in a relaxed condition with cells having their preferred area and preferred edge lengths and not being contractile yet. Thus, E_1, E_3 and E_4 equal zero and total energy is minimal. At onset of furrow formation the actomyosin localizes to the apical cortex and makes the cells contractile (red colour). E_3 and, consequently, total energy is massively increased forcing the cells to undergo area reduction to reclaim an energetically favourable morphology. During furrow formation cells reduce their area, thus contractile energy (E_3) decreases, but elastic energy (E_1 and E_4) increases owing to the compression of cell cortices and edges. Total energy reaches a local minimum when contractile and elastic forces balance each other and area reduction ceases.

have previously proved advantageous to study epithelia in *Drosophila* in various developmental contexts (Farhadifar et al., 2007; Kafer et al., 2007; Landsberg et al., 2009; Nagai & Honda, 2001; Nagai & Honda, 2009; Osterfield et al., 2013; Rauzi et al., 2008).

After completion of cellularization cells are assumed to be in a relaxed state as they have taken on their preferred area and preferred edge lengths and are not contractile yet (Fig. 18C). When gastrulation starts and cells become contractile, they will reduce their surface area in order to achieve a more favourable morphology. Area reduction continues until the increase in elastic energy balances the contractile force and further area reduction is no longer energy-efficient (Fig. 18C). The extent of area reduction is largely dictated by the ratio of

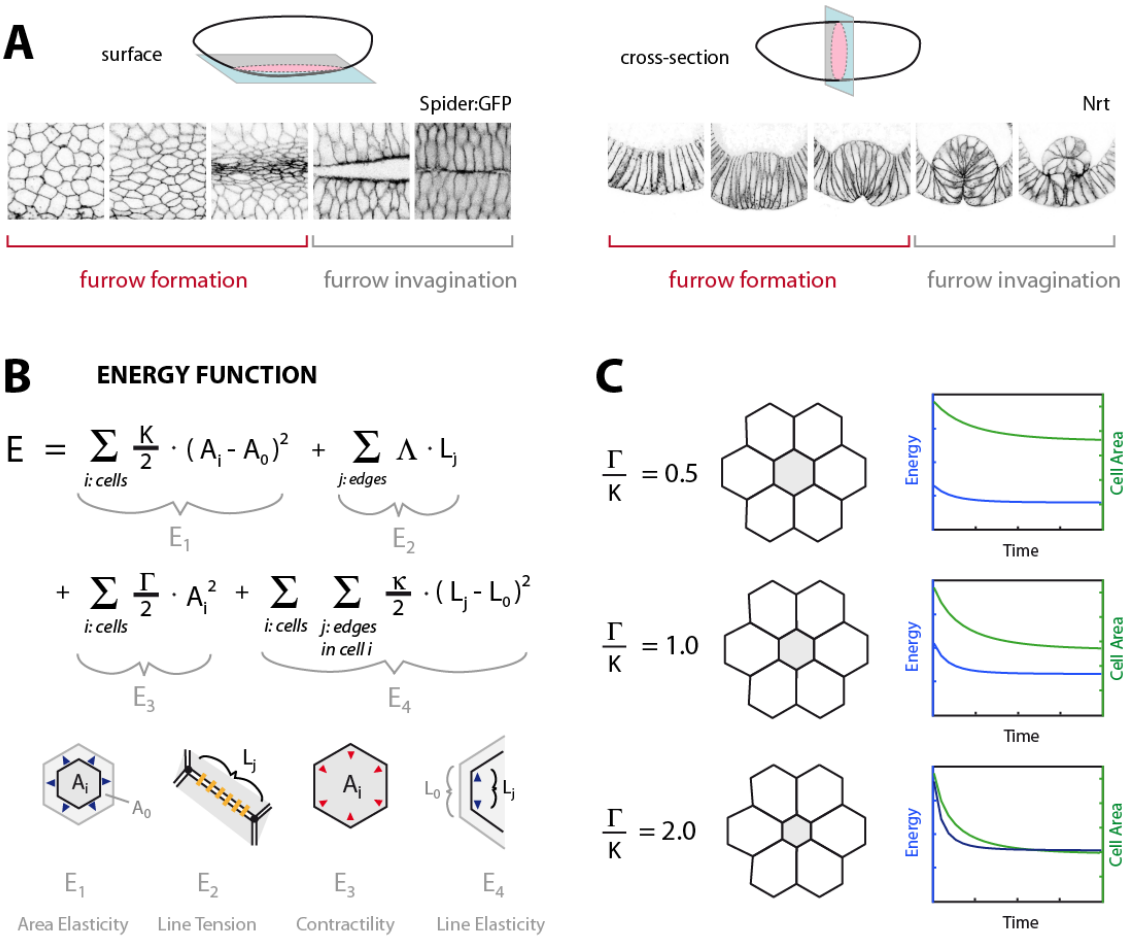
A
surface
Spider:GFP
furrow formation
furrow invagination
cross-section
Nrt
furrow formation
furrow invagination
B
ENERGY FUNCTION
E = Σ (K/2)·(A_i - A_0)^2 + Σ Λ·L_j
i: cells
j: edges
E_1
E_2
+ Σ (Γ/2)·A_i^2 + Σ Σ (κ/2)·(L_j - L_0)^2
i: cells
j: edges in cell i
E_3
E_4
A_i
A_0
L_j
L_0
E_1
Area Elasticity
E_2
Line Tension
E_3
Contractility
E_4
Line Elasticity
C
Γ/K = 0.5
Γ/K = 1.0
Γ/K = 2.0
Energy
Cell Area
Time
D
CUTOFF MODEL
Γ
ventral midline
CELL ROW
E
GRADIENT MODEL
Γ
ventral midline
CELL ROW
F
Accumulated intensity
Distance from midline
Spider:GFP
MyosIn:mCherry
G
Avg. myosin int. [per µm²]
4000
3500
3000
2500
2000
0
10
20
30
40
Distance from midline [µm]
H
Zip
RhoGEF2
200
100
0
mean pixel int.
cell

Fig. 19: Biophysical model of ventral furrow formation (II). A: Surface sections (left) and cross-sections (right) of the ventral epithelium of the *Drosophila* embryo during ventral furrow formation and furrow invagination. Image series span approximately 20 minutes real-time (Nrt: Neurotactin). **B:** Energy contributions considered for the vertex model of the epithelium in surface view. E_1 represents area elasticity with A_i being the surface area of cell *i* and A_0 its preferred area (equal for all cells). E_2 represents line tension arising along cell edges. E_3 represents contractility (preferred area equals zero in this case). E_4 represents line elasticity with preferred edge length L_0 (equal for all cells). E describes the total energy in the sheet at a certain time point. **C:** Reduced model with seven cells with different ratios of contractility and area elasticity in the central cell (grey). Contractility is set to zero in the surrounding cells. **D:** Cutoff model of contractility: Cells in an antero-posterior strip on the ventral epithelium have equal non-zero contractility while cells lying outside are non-contractile. **E:** Gradient model of contractility: Contractility gradually decreases the further away a cell is located from the ventral midline. **F:** Still of a confocal live-recording with myosin labelled in red (green Spider:GFP). Accumulated myosin intensity is measured by integrating pixel intensity for each pixel row in the image (dotted line: ventral midline). **G:** Scatter plot of myosin intensity (per μm^2), averaged over the time of furrow formation, against cell distance from the ventral midline. The closer the cell lies to the midline, the higher is its average myosin intensity. **H:** Cross-sections of embryos fixed during ventral furrow formation and immunostained for Zipper (myosin, left) or RhoGEF2 (right). For each cell (identified in the parallel channel with membranes labelled by anti-Nrt, not shown) an apical ROI was drawn and mean pixel intensity was measured.

contractility and the opposing area elasticity (Fig. 19C). We prefer to strictly discern between the notions "contraction" and "constriction" as we use "contraction" to describe intrinsic actomyosin contraction activity and "constriction" to refer to the observable effect of this contraction on cell shape, i.e. apical area reduction. By this rationale, cell contraction would usually imply constriction; however, a cell may execute contractions but fail to constrict if, for instance, the actomyosin in not properly attached to the cell membranes as observed in *dzy* or *rap1* GLC (see section 6.1). Also, due to the opposing elastic forces, enduring contractility does not necessarily imply enduring constriction as the cell will finally arrive in a state where force balance is reached (Fig. 19C).

For our purposes, all cells are assumed to have identical area elasticity, line elasticity and line tension, but we let contractility vary within the sheet (Fig. 19D,E). In gastrulating embryos, constriction only occurs in ventral cells (defined here as all cells which become internalized during furrow invagination). However, among these cells different constriction levels are

achieved since cells lying closer to the ventral midline yield higher constriction than those lying further lateral before they become invaginated (Oda & Tsukita, 2001; Sweeton et al., 1991; see also Figs. 19A, 20C). This prompts the question whether all ventral cells have the same contractility or whether contractility varies among them. Assuming temporally constant contractility in a first approach, we set up two model variants with regard to how contractility varies spatially within the sheet. It may be that only a narrow antero-posterior strip of ventral cells is contractile, while the remaining ventral cells are non-contractile (as are lateral cells). Alternatively, contractility may gradually decline the further away a cell is located from the ventral midline. Accordingly, in the first variant (named "Cutoff") a sharp boundary between contractile and non-contractile cells is assumed: Central cells are contractile ($\Gamma > 0$) while the remainder is non-contractile ($\Gamma = 0$) (Fig. 19D). In the alternative model variant (named "Gradient"), contractility gradually decreases from the ventral midline towards lateral cells (Fig. 19E). Experimental evidence supports this notion of a contractility gradient as intensity measurements of apical myosin reveal a gradual decrease from ventral to lateral during furrow formation (Fig. 19F-H), consistent with a gradual decrease of constriction levels achieved (Oda & Tsukita, 2001). Interestingly, upstream regulators of myosin activation, such as RhoGEF2 (Fig. 19H), Fog (Costa et al., 1994), and Twi (Leptin, 1991) also show a gradual expression in the ventral epithelium. These data would favour the hypothesis of a ventral-to-lateral contractility gradient, but, nonetheless, both model variants are implemented and tested for their performance.

6.2.2 A contractility gradient, combined with stochastic contraction dynamics, accurately reproduces ventral furrow formation

With temporarily constant contractility enabled, both the cutoff and the gradient model result in the emergence of a band of constricted cells with lateral cells moving towards the midline,

as seen in live-imaging data (Fig. 20A-C; Videos 6-8). The degree of constriction as well as the morphological appearance of ventral cells are well reproduced but can change dramatically if alternative energy parameters are used (Videos 9,10). In any case, the cutoff model leads to a very artificial furrow morphology as strongly constricted cells of the central rows directly adjoin strongly dilated cells, located more lateral (Fig. 20A). Such an appearance is not seen in live-recordings where a more gradual transition from constricted to unconstricted cells can be observed (Fig. 20C; Oda & Tsukita, 2001). In contrast, the gradient model well reproduces this gradual shift and results in a more realistic overall morphology (Fig. 20B).

Next, we sought to let contractility vary in time. Live-imaging shows that apical myosin intensity starts weak in ventral cells and grows stronger during ventral furrow formation (Martin et al., 2010; Martin et al., 2009) (Fig. 20D). Thus, temporarily constant contractility appears not to be an appropriate assumption. We modelled increasing myosin activity by letting contractility start at zero at the onset of gastrulation and increase in time (see Materials & Methods). Indeed, this adjustment adds a noticeable improvement to the model. Constriction now starts more subtle resembling *in vivo* data for which a slow rate of constriction at the onset of furrow formation has been documented (Oda & Tsukita, 2001; Sweeton et al., 1991) (Video 11). However, all cells still follow the same deterministic time-course which is not seen in live-imaging where constriction appears more heterogeneous (Video 6). Also, actomyosin contractions have been shown to occur in a very dynamical, asynchronous fashion as it appears to coalesce in a stochastic fashion, autonomously in each ventral cell (Martin et al., 2009) (Fig. 20D). This dynamics behaviour would not be well represented by a simple linear increase in contractility, identical in all cells. Thus, we extended the model by letting contractility feature cell-autonomous stochastic

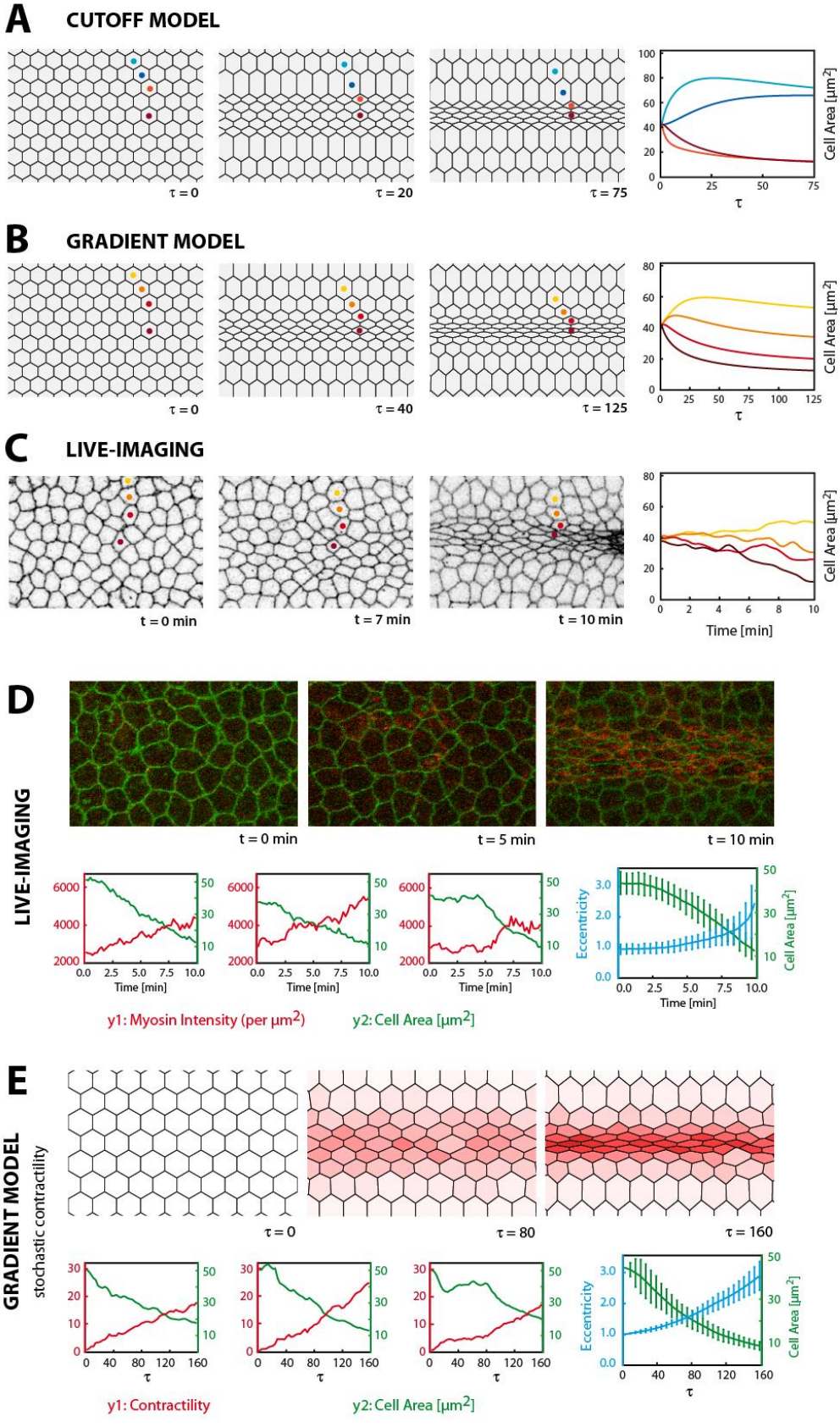
A
CUTOFF MODEL
τ = 0
τ = 20
τ = 75
Cell Area [µm²]
τ
B
GRADIENT MODEL
τ = 0
τ = 40
τ = 125
Cell Area [µm²]
τ
C
LIVE-IMAGING
t = 0 min
t = 7 min
t = 10 min
Cell Area [µm²]
Time [min]
D
LIVE-IMAGING
t = 0 min
t = 5 min
t = 10 min
Time [min]
Eccentricity
Cell Area [µm²]
y1: Myosin Intensity (per µm²)
y2: Cell Area [µm²]
E
GRADIENT MODEL
stochastic contractility
τ = 0
τ = 80
τ = 160
Eccentricity
Cell Area [µm²]
y1: Contractility
y2: Cell Area [µm²]

Fig. 20: Reproduction of ventral furrow formation. A-C: Morphology of the ventral epithelium in the cutoff (A) or gradient (B) model with plots of apical area of indicated cells. In the gradient model constriction levels gradually decrease with distance from the ventral midline (B), comparable to live-imaging (C). In the cutoff model (A), constricted cells (= contractile cells, red) directly abut unconstricted cells (= non-contractile cells, blue). τ refers to time-steps in the model. Area designations in μm^2 are obtained after normalization to live-imaging data (see Materials & Methods). **D:** Live-recording of furrow formation spanning 10 minutes real-time with labelled membranes (green, Spider:GFP) and myosin (red sqh:mCherry). Myosin contraction occurs in a stochastic fashion and autonomously in each cell. Plots depict cell area and myosin intensity in three cells. Right plots depicts cell area and eccentricity (see Fig. 21A), averaged over all ventral cells (mean ± s.d.). **E:** Simulation of the gradient model with time-dependent, stochastic contractility (coded by colour). Plots depict cell area and contractility in three cells. Right plots depicts cell area and eccentricity, averaged over all ventral cells (mean ± s.d.).

fluctuations (Fig. 20E) (see Materials & Methods). This way, each cell in the sheet executes an individual contraction dynamics which follows a linear trend but shows stochastic noise mimicking the dynamical action of the actomyosin (Fig. 20E; Video 13). Simulation of this model yields very close resemblance to live-imaging data since a band of constricted cells is well reproduced and the more heterogeneous cell morphology realistically accounts for the appearance in live-recordings (Fig. 20D,E; Videos 6,12,13).

We conclude that a sharp boundary between contractile and non-contractile cells in the *Drosophila* ventral epithelium proves unlikely as such an arrangement would not match experimental data observed. In contrast, simulation of a contractility gradient, especially when combined with stochastic, asynchronous dynamics reproduces live-imaging data well and appears to be a good basis to computationally describe ventral furrow formation.

6.2.3 The model predicts anisotropic constriction

The good performance of the model opens the possibility to utilize it for predictive purposes, i.e. explore to what extend the model can explain phenomena observed *in vivo*. While undergoing apical constriction, cells of the ventral furrow exhibit another conspicuous shape change as they gain an eccentric morphology (Martin et al., 2010; Sweeton et al., 1991). Apical constriction does not occur uniformly but asymmetrically ("anisotropically", Martin et al., 2010) as cells reduce their latero-ventral diameter much stronger than the antero-posterior diameter leading to eccentric morphology (Figs. 20D, 21A). The model readily predicts eccentricity in constricting cells (Fig. 20E). We hypothesized that two features of the model may contribute to anisotropic constriction: The contractility gradient and the geometry of the cell sheet. On a square-shaped sheet with constant contractility, constriction occurs without significant anisotropy, i.e. cells do not acquire an eccentric morphology (Fig. 21B). However, if on the same square-shaped sheet a contractility gradient is enabled, the ventral cells acquire distinct eccentricity due to anisotropic constriction (Fig. 21C). As contractility only varies along the dorso-ventral axis in the gradient, contractile action along the antero-posterior axis will not differ between cells lying in the same row and will balance out on average. Thus, little net constriction is achieved in this axis. Conversely, even under constant contractility, considerable eccentricity is achieved when the cell sheet is expanded in the antero-posterior axis, mimicking the rectangular geometry of the *Drosophila* ventral epithelium (Fig. 21D) which likely causes different tensions in both axes as concluded previously (Martin et al., 2010). Consequently, the model shows that anisotropic constriction will naturally arise when cells are arranged in a rectangular geometry and contract according to a dorso-ventral gradient.

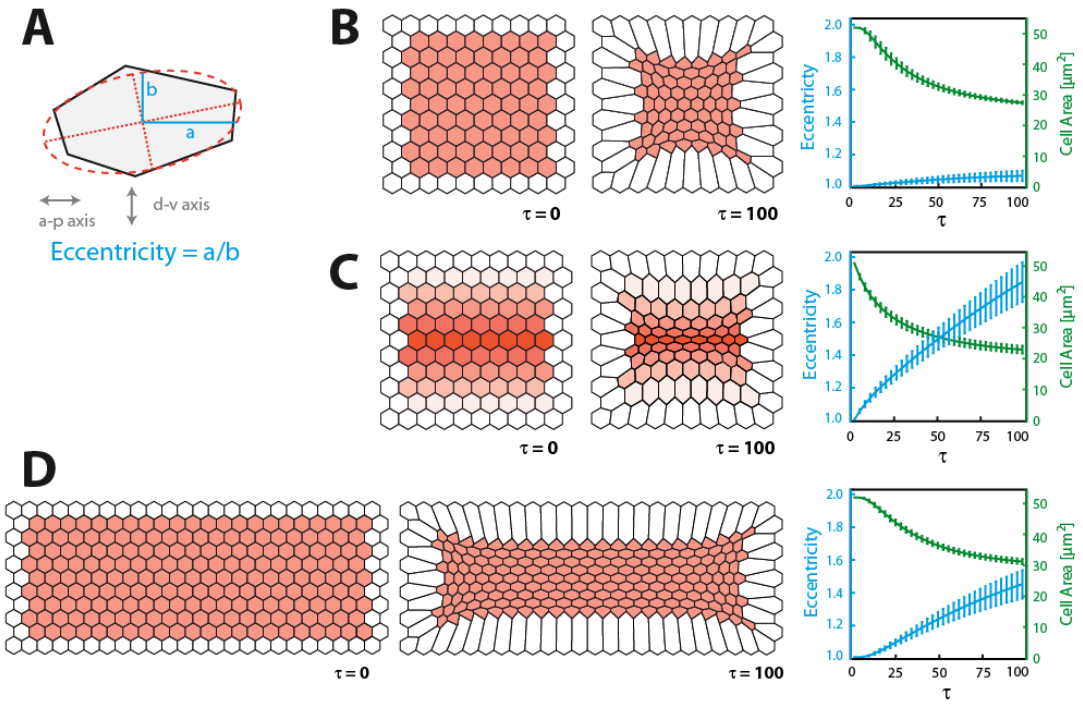

Fig. 21: Anisotropic constriction. A: Anisotropy of constriction results in eccentric cell morphology that is quantified by relating the antero-posterior to the dorso-ventral cell dimension after fitting an ellipse to the cell (after Martin et al. (2010)). **B:** Model with constant contractility (red) on a square shaped sheet (white border cells non-contractile). Bar plots represent mean ± s.d. over 6 ventral cells from the central region. **C:** Model with a gradient of contractility on the same cell sheet as in B. Bar plots represent mean ± s.d. over 6 ventral cells from the central region. **D:** Model with constant contractility on a rectangular sheet (white border cells non-contractile). Bar plots represent mean ± s.d. over 42 ventral cells from the central region

6.2.4 The model predicts incremental cell area reduction

We next investigated in more detail if the stochastic gradient model would quantitatively reproduce apical constriction. The stochastic contractility dynamics implemented in our model renders apical constriction highly variable, consistent with live-imaging analysis where the temporal dynamics of apical constriction also shows a high variability (Fig. 22A,B). The rate of constriction can vary considerably over time in a single cell, and cells may even show temporary dilations (Fig. 22B-2, arrowhead) – a phenomenon also seen in live-imaging

analysis (Fig. 22A-2 arrowhead). A feature that has caught much attention in the analysis of ventral furrow formation *in vivo* is the appearance of stagnation periods – a time interval over which cell area remains nearly constant before area reduction recommences (Martin et al., 2009; Fig. 22A-3, brackets). It had been hypothesized that these stagnation periods represent a stereotypical phenomenon of apical constriction and are brought about by a cytoskeletal stabilization mechanism (ratchet) that is active between discontinuous contraction pulses (Martin et al., 2009). This stabilization is supposed to be genetically controlled through Twi via an unknown mode of action (Martin et al., 2009). Interestingly, stagnation periods readily show up in area graphs in the model (Fig. 22B-3, brackets). It must be deduced accordingly, that these stagnation periods which were considered visual manifestations of an underlying stabilization mechanism (Martin et al., 2009), can arise passively since they are predicted by a model which does not include any such stabilization mechanism (Fig. 19B). Stagnation periods are not seen if stochastic fluctuations are disabled in the model (Fig. 22C). Consequently, it is stringent to hypothesize that stochastic fluctuations in contractility may cause stagnations in area reduction. Indeed, contractility rate and constriction rate show a significant correlation (Fig. 22D) strongly suggesting that stagnation in area reduction is linked to stagnation in contractility. It is noteworthy that contractility rate and constriction rate appear slightly shifted against each other (Fig. 22D): The correlation takes on its maximum if the contractility rate is slightly shifted forward in time (Fig. 22E). This phenomenon is in congruence with the cell responding to increasing intrinsic contractility by reducing its area and has also been found in live-imaging analysis (Martin et al., 2009). We tested if temporary periods of constant contractility would imply stagnations in area reduction by considering a reduced model where we focused on a single cell surrounded by six neighbours (Fig. 22F). All cells in the reduced system have the same constants for area elasticity, line tension and line elasticity that were used for the standard simulations.

However, contractility is only handed to the central cell and allowed to rise from zero in a step-like manner by implementing a period of constancy (Fig. 22F). In fact, the central cell quickly runs into a local "plateau" of constant area after contractility has ceased to rise and will recommence constriction only after contractility has begun to increase again (Fig. 22F). This observation becomes comprehensible when considering the energy in the system which will quickly fall to a local minimum after the cessation of contractility increase (Fig. 22F, arrow). Thus, stagnations are the consequence of temporary force balance between temporarily constant contractility and the opposing elastic forces within the cell. Due to the stochastic nature of contractility in the model temporary periods of nearly constant contractility may arise from time to time and will allow local force balance, resulting in stagnations in area reduction (Fig. 22D, grey bars).

Although the intrinsic contractility can be well assumed to occur in a cell-autonomous fashion, constriction (or more general, cell shape change) will certainly not occur independently from adjacent cells since the cells are part of a mechanically coherent epithelium. Therefore, one has to take the possibility into account that contractions of adjacent cells may have a considerable effect on each other's shape change. For instance, temporary increase of cell area, seen both in live-imaging analysis and in the model (Fig. 22A,B,D, arrowhead), is likely caused by contracting neighbours which will dilate the cell due to their mechanical coherence. We sought to test the influence of neighbour contractility by first considering the reduced system in which we now allow neighbour cells to be contractile as well. In a reference simulation with the central cell featuring increasing contractility and without neighbour contractility, the area is reduced without stagnation (Fig. 22G-1). However, when we allow contractility in neighbour cells to rise, the contractility of the central cell will be counteracted to an extent which depends on the strength of neighbour

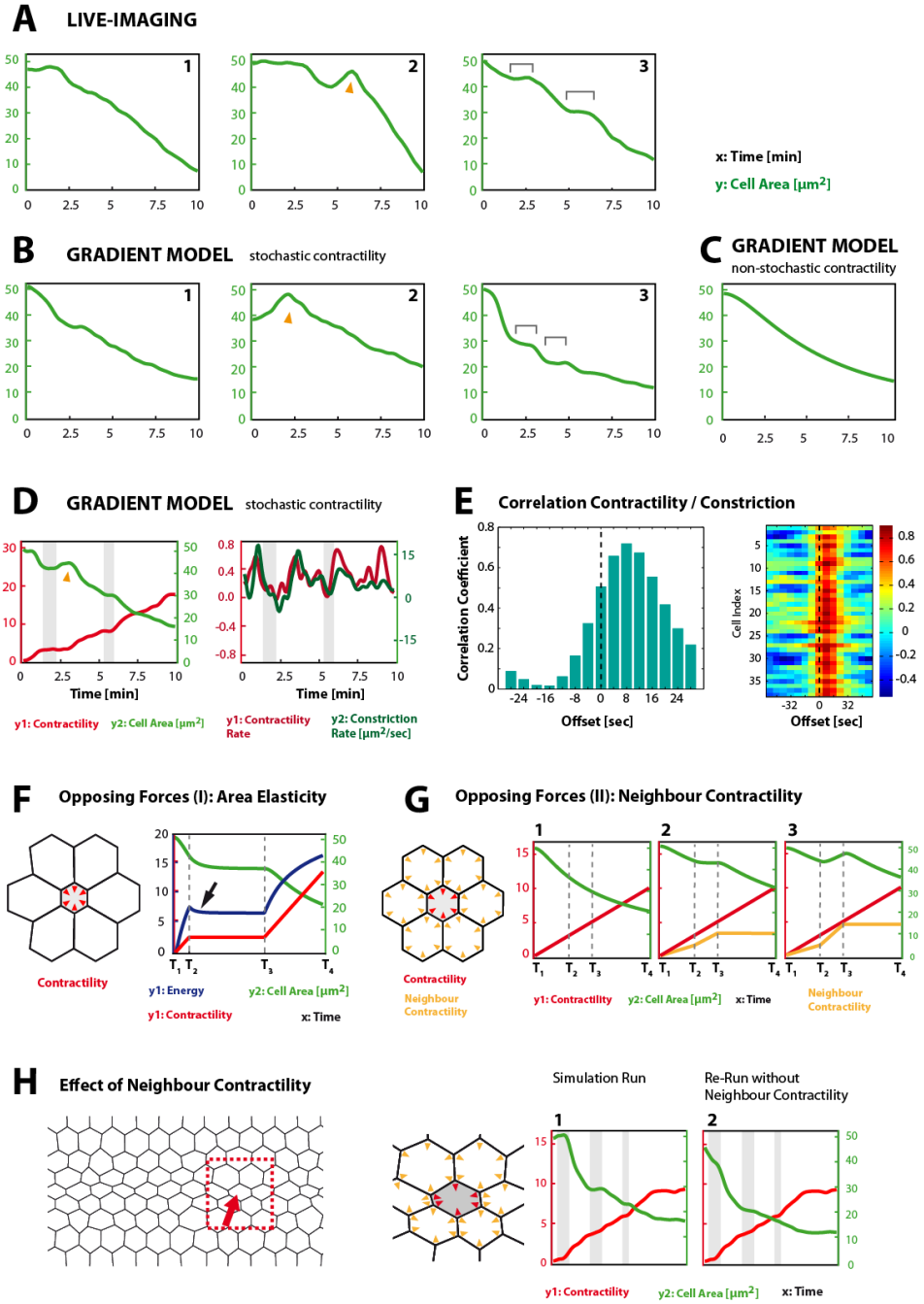

Fig. 22: Analysis of incremental area reduction. A: Graphs of apical area typically obtained in live-recordings. Cells may become temporarily dilated (2, arrowhead) or show stagnation periods (3, brackets). Most graphs do not show unambiguous stagnations or other noticeably irregularities (1). **B:** Graphs of apical area typically obtained in the gradient model with stochastic contractility. Like in live-imaging, cells may show temporary dilations (2, arrowhead) and stagnation periods (3, brackets). **C:** If stochasticity is omitted ($\gamma_2 = 0$, see Materials & Methods), all graphs of ventral cells equal each other, and stagnation periods are missing. **D:**

Stagnation periods often coincide with periods of temporarily constant contractility (grey underlay) indicating correlation between contractility rate and area reduction rate (=constriction rate). **E:** Correlation coefficients between contractility rate and constriction rate in a single cell (left) or for a total of 38 ventral cells (right), plotted against the offset by which contractility rate is shifted forward in time. Contractility rate precedes constriction by ca. 8 sec., comparable to results obtained from live-imaging analysis (see Fig. 2e in (Martin et al., 2009)). Time designations are obtained after normalizing the computational time-steps required to reach furrow completion to 10 min real-time (see Materials & Methods). **F:** Reduced model, consisting of one contractile central cell and six surrounding non-contractile cells. In the central cell contractility rises linearly but remains constant between T_2 and T_3. The total energy quickly falls into a local minimum (arrow) and area is not further reduced until contractility begins to rise at T_3. **G:** Reduced model, consisting of six contractile cells. When contractility of the central cell rises linearly while neighbour contractility is set to zero, area is reduced without stagnations (1). When neighbour contractility rises between T_2 and T_3, area reduction of the central cell stagnates (2). Depending of the strength of neighbour contractility increase, the cell can even become temporarily dilated (3). **H:** Detail of a simulation run of the gradient model with stochastic contractility. Area and contractility of the marked cell (arrow) plotted to the right (1). When contractility of all surrounding cells (yellow) is manually switched to zero and the simulation run is identically replicated otherwise (i.e. all remaining cells execute the same contraction dynamics as in the previous run), stagnations periods disappear or become vague (2, grey underlays).

contractility. Under moderate neighbour contractility the area of the central cell will stagnate (Fig. 22G-2), while under strong neighbour contractility it may even become temporarily expanded (Fig. 22G-3). This demonstrates that cell shape change cannot be considered independent from neighbouring cells in the epithelium. Indeed, neighbour contractility proves to have significant impact on cell shape of single cells when turning back from the reduced model to the full stochastic gradient model: Simulation runs of the model were recorded in which a cell showed stagnation periods and therefore incremental area reduction. When these simulation runs were repeated under identical settings, except that the contractile activity of the neighbouring cells were manually set to zero, stagnation periods and incremental area reduction were lost (Fig. 22H). Consequently, the model shows that: (i) an active stabilization mechanism as postulated by the ratchet model is not mandatory in order to observe occasional

stagnation periods in surface reduction, and (ii) cells do not need to undergo regulated alternating phases of contraction and stabilization in order to efficiently reduce surface area.

Based on these finding we assume that analogous mechanisms work during apical constriction in ventral furrow formation *in vivo*. As cells are tightly coupled via adherens junctions and execute asynchronous stochastic actomyosin contractions, cell constriction will be constrained by contraction activity of neighbouring cells. Consequently, we hypothesize that stagnations in area reduction could be explained through the counterbalancing effects of elastic forces within the cell and the contractile action of neighbouring cells.

6.2.5 *twi* mutants can be modelled with randomly reduced contractility

Finally, we wanted to test if our gradient model would also prove sufficient to reproduce mutant phenotypes. Twi acts a major regulator of ventral furrow formation as upon loss of Twi the ventral furrow is severely compromised and does not invaginate (Leptin & Grunewald, 1990). Indeed, apical constriction is largely missing in *twi* mutants with only a subset of ventral cells undergoing area reduction which is also considerably slowed down (Fig. 23A). However, in contrast to a previous report (Martin et al., 2009) we do not find cell area to markedly oscillate between reduction and dilation (Fig. 23A; Video 14). In particular, temporary dilations are rare and are also observed in wildtype (see above, Fig. 22A). Immunostaining reveals that myosin fails to properly localize to the apices in ventral cells upon the onset of gastrulation at stage 6 in *twi* mutants but remains stuck at the basal sides (Fig. 23B-1). Also RhoGEF2, being a critical requirement for apical actomyosin localization, does not properly localize to the apices in *twi* mutants (Kölsch et al., 2007; see also Fig. 23B-2) – as expected based on the genetic model of furrow formation (Fig. 25A). Faint apical localization of myosin is visible not earlier than stage 7, but occurs fragmentarily as only a subset of cells accumulate detectable myosin (Fig. 23B-3). Thus, we assume that apical

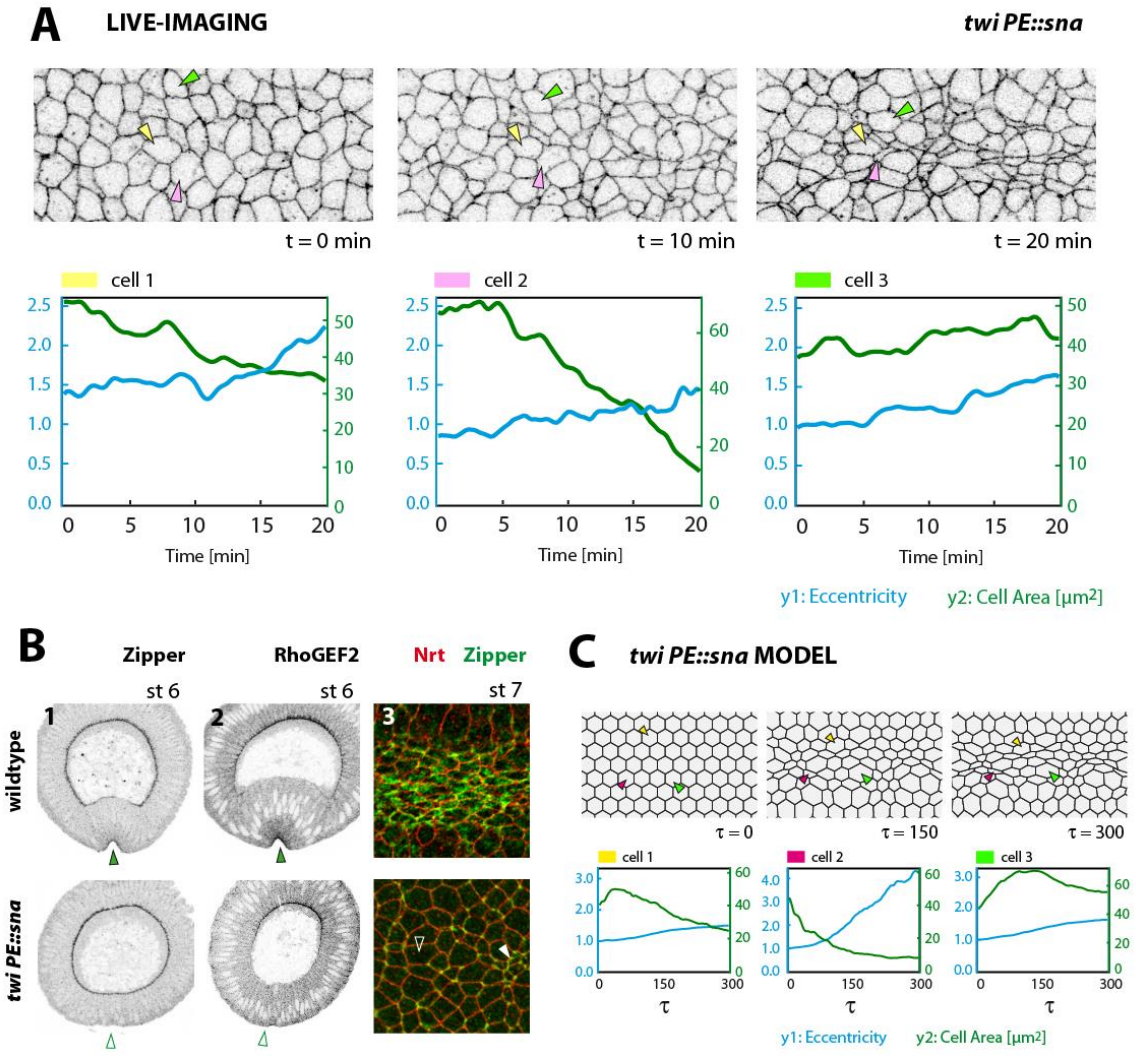

Fig. 23: Ventral furrow phenotype of *twi* mutants. A: Stills of a live-recording of a *twi* mutant spanning 20 minutes after completion of cellularization (Spider:GFP). Plots depict apical area and eccentricity for three indicated cells. **B:** Localization of myosin (Zip) and RhoGEF2 in wildtype and *twi* mutant embryos, fixed during ventral furrow formation. 1 and 2 cross-sections (stage 6), 3 surface section (2 µm below surface, stage 7). Myosin and RhoGEF2 localize to the apices in ventral cells in the wildtype (1,2: arrowheads). In *twi* this apical localization fails at stage 6 (1,2: empty arrowheads). At stage 7 low levels of myosin accumulate apically, but only in a subset of ventral cells (3: filled arrowhead, compare to cell under empty arrowhead) **C:** Stills of a simulation run with reduced contractility, varying randomly in the sheet (see Materials & Methods). Plots depict apical area and cell eccentricity for three indicated cells.

constriction in *twi* mutants is largely absent because of incomplete actomyosin localization – in concordance with the presumed role of Twi as a master regulator of ventral furrow

formation (Leptin & Grunewald, 1990) (Fig. 25A). We sought to model this weak, fragmented myosin accumulation by randomly scaling down contractility within the cell sheet while letting all other parameters unaltered (see Materials & Methods). Thus, contractility is now generally lowered, but this defect affects different cells to a different degree. Introducing this variability turns out to be sufficient to disrupt the formation of the ventral furrow in the model. Ventral cells now constrict to a variable extent leading to a highly irregular appearance, as seen in live recordings (Fig. 23C; Video 15). Both constricted and unconstricted cells can be found in a random spatial arrangement. As in live-imaging, eccentricity is markedly reduced among cells (Fig. 23C), possibly because many cells can now undergo unconstrained constriction due to the reduced counterforce exerted by neighbour cells which fail to contract. Thus, the model shows that randomly reduced contractility as derived from experimental data proves sufficient to explain the irregular constriction in *twi* mutants and the disruption of the ventral furrow. On the contrary, these data give no clear indication that the *twi* phenotype supports the notion of a cytoskeletal stabilization mechanism.

In summary, the presented computational model proves capable of accurately simulating ventral furrow formation *in silico*. Analysis of the model suggests that the previously postulated regulatory complexity is not required to let cells effectively undergo apical constriction. Experimental data does not unequivocally support the notion of a complex cytoskeletal stabilization mechanism, either. Since scientific concepts aim at explaining experimental data using the simplest (= most parsimonious) interpretation possible to account for all available data (Gauch, 2003), we propose that ventral furrow formation occurs as a stochastic process where a genetic cascade triggers temporarily and spatially restricted actomyosin contractility which leads to surface area reduction under the physical constraints of elasticity and mechanical cohesion between cells (Fig. 25).

7 DISCUSSION

7.1 Role of Dzy and Rap1 in ventral furrow formation

In the first part of this work we found that both the PDZ-GEF Dzy and its target Rap1 are required for ventral furrow formation (VFF) during *Drosophila* gastrulation. In the absence of Dzy the establishment of the circumferential adhesion belt is slowed down while in the absence of Rap1 only a fragmentary adhesion belt is formed (Fig. 9). In the case of *dzy*, this slowdown in apical junction assembly translates into a slowdown of apical cell constriction, since the cytoskeleton cannot attach to membranes during early gastrulation. Thus, first actomyosin contractions do not evoke cell shape change (Fig. 24). In the case of *rap1*, junction assembly is much more severely affected, and only a fragmentary apical junction belt forms during gastrulation (Fig. 9). This results in a variable capability of mid-ventral cells to undergo constriction since only variable levels of apical AJs are available to connect to the contracting actomyosin (Fig. 24). Dzy and Rap1 localize cortically during and after gastrulation consistent with a role in junction assembly and possibly maintenance. Levels of both proteins are diminished in the mesoderm once it has been internalized (Fig. 16). Overexpressing Dzy or $Rap1^{V12}$ in the mesoderm results in an inhibition of mesodermal spreading (Fig. 17), possibly by keeping up DE-Cad mediated adhesion. Our findings underline the roles of the PDZ-GEF Dzy and its GTPase Rap1 as critical factors regulating the dynamics of adherens junction formation in *Drosophila* gastrulation.

7.1.1 Dzy guarantees the fast assembly of the apical junction belt required for ventral furrow formation.

Apical constriction of ventral cells is known to be a major driving force of VFF and much progress has been made in deciphering the signal cascade leading from ventral fate

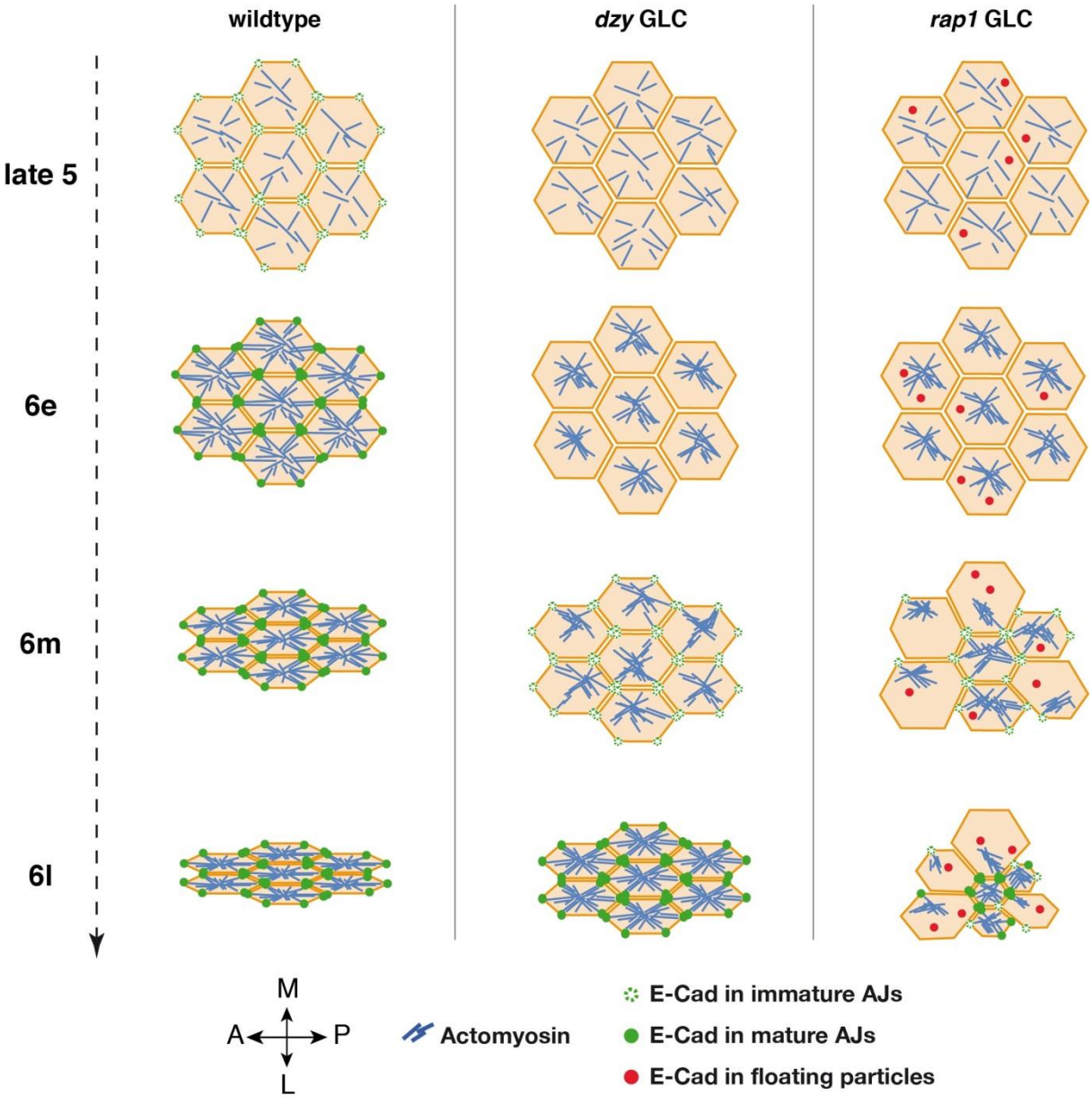

Fig. 24. Model of cell shape changes in wildtype, *dzy* germline clones and *rap1* germline clones during ventral furrow formation. Schematic depiction of mid-ventral cells in apical surface views (L: lateral; M: medial; A: anterior; P: posterior). **Wildtype. late 5:** Towards completion of cellularization DE-Cad begins to accumulate in apical AJs, and the actomyosin filament system starts to assemble. **6e:** The contracting actomyosin has attached

to a belt of mature AJs and started to constrict apical cell area. **6m/6l:** Actomyosin contractions continue and cell apices are further constricted. ***dzy* GLC**. **late 5:** Apical actomyosin assembly begins, but the establishment of apical AJs is delayed. **6e:** The actomyosin has readily assembled but does not find sites to attach to. Thus, initial contractions do not induce cell shape change. **6m:** Apical AJs begin to form providing weak attachment sites. Thus, first cell constrictions can be evoked by the contracting actomyosin. **6l:** The apical AJ belt has finally formed, so actomyosin contraction can be fully translated into cell constriction, eventually. ***rap1* GLC**. **late 5:** Apical actomyosin begins to assemble, but DE-Cad is not accumulated apically. In addition, stable integration of DE-Cad in cell membranes is affected so particles of DE-Cad float through the cytoplasm. **6e:** Actomyosin assembly is completed and contractions start, but are not translated into cell shape change as apical AJs are missing. **6m:** Apical AJs begin to form in some cells generating attachment sites for the contracting actomyosin. Thus, apical constriction can commence in a subset of ventral cells, while others remain unconstricted. **6l:** Ventral cells have constricted according to the number of available apical AJs leading to a random arrangement of constricted and unconstricted cells. Constricted cells have achieved a high level of constriction since neighbouring unconstricted cells have not exerted a counterforce.

determinants to an assembly of a contractile actomyosin at the apices of ventral cells (Barrett et al., 1997; Dawes-Hoang et al., 2005; Häcker & Perrimon, 1998; Kölsch et al., 2007; Morize et al., 1998; Parks & Wieschaus, 1991). Also, the importance of tight coupling between the contracting actomyosin and the cell membranes mediated by AJs has been previously highlighted (Sawyer et al., 2009). Although MyoII has been implicated as a downstream target of dzy during dorsal closure (Boettner & Van Aelst, 2007), we cannot attribute the slowdown in cell shape change during VFF seen in dzy GLC to a slowdown in apical assembly of the actomyosin apparatus. Unlike what has been reported for dorsal closure, actomyosin exhibits the same relocalization to the apex of ventral cells at the end of cellularization in *dzy* GLC and in wildtype. Furthermore, we find MyoII coalesced into balls within unconstricted cells when gastrulation starts, supporting the notion of a contracting actomyosin meshwork (Fig. 7). Coalesced MyoII within unconstricted cells has also been reported previously for ventral cells in *arm* (Dawes-Hoang et al., 2005), *cno* and *rap1* GLC (Sawyer et al., 2009) all of which exhibit defective cell constriction. In these studies, this

observation was considered an indication of contracting actomyosin that is detached from cell membranes. Our findings are consistent with this view (Figs 7,9).

Previous work has revealed that ventral cells are not constricted by continuous contraction and that circumferential actomyosin cables do not contribute significantly to the constriction. Instead a medially localized actomyosin meshwork is thought to reach out to make contact to AJs at the cell membranes and executes discontinuous contraction pulses to constrict the apex (Martin et al., 2009). Our observation that apical constriction still occurs in *dzy* GLC, later than in wildtype, but apparently as soon as AJs are in place, are in accordance with these findings. Thus, apical constriction is not irrecoverably affected if AJs are not ready at the onset of gastrulation. Actomyosin contraction appears to take place in a dynamical and repeated pulsed fashion over the entire time-span of gastrulation allowing cells to constrict eventually, despite an initial delay in AJ formation (Fig. 7J,L; Fig. 24).

A puzzling feature of the *dzy* phenotype is the failure of the ventral furrow to finally close although ventral cells have undergone complete, albeit delayed, apical constriction (Fig. 5M,N; Video 3). We propose that the invagination of the mesoderm has to occur within a critical time slot, which is missed in *dzy* GLC due to the delay in AJ establishment and, consequently, apical cell constriction. In fact, the ventral furrow of *dzy* GLC very much resembles the ventral furrow of a wildtype embryo 5 to 10 minutes earlier (compare frame 51 to frame 88 in Video 2; frame 10 to 15 in Video 3). Still, the furrow is not properly sealed in the end, less tissue moves inside and often the furrow opens up again (Video 3). This supports the notion that apical constriction alone is not sufficient to internalize the ventral furrow. Computer simulations have indicated that apical constriction alone is incapable of generating a tissue invagination and have postulated ectodermal pushing as a second source of force to internalize the ventral furrow (Conte et al., 2009). Such a force could be exerted by turgor

pressure in medio-lateral direction within the cellular blastoderm. The ventral furrow may serve as a "predetermined breaking line", where the tissue can give in to the inherent pressure. The delay in VFF of *dzy* GLC leads to a temporal overlap with germband extension and PMG invagination that immediately follow the internalization of the ventral furrow in wildtype (Campos-Ortega & Hartenstein, 1985). Both processes are likely to reduce the epithelial pressure in medio-lateral dimension since they expand the epithelium in the antero-posterior dimension. Consequently, pressure might have already become too low to generate the force required to push in the mesoderm when the "breaking line" has finally emerged. In addition, it cannot be ruled out that the ventral furrow is not properly closed and opens up again in *dzy* GLC because of a failure in sealing the edges of the furrow.

7.1.2 Rap1 ensures membrane association and apical accumulation of DE-Cad.

In contrast to *dzy* GLC, only a fragmentary AJ belt is formed in *rap1* GLC as DE-Cad is diffusely distributed in the membranes and shows delayed and incomplete apical accumulation (Fig. 9). In addition, DE-Cad reveals a striking cytoplasmic mislocalization to floating particles that are seen in *rap1* GLC only (Fig. 9, Video 4). Although the nature of these particles remains to be clarified, we speculate they represent DE-Cad rich membrane vesicles originating from the cell membrane. It has been reported earlier (Sawyer et al., 2009) that initial AJ assembly is unaffected in *rap1* GLC, but this conclusion was based on anti-Arm staining which look unaffected in our analysis as well (Fig. 13). Thus, Rap1 seems to act on DE-Cad specifically to assure its proper localization. In mammalian cells regulation of DE-Cad endocytosis has long been recognized as a cellular mechanism to modulate AJs (de Beco et al., 2009; Le et al., 1999). In this context, Rap1 has been implicated in having a key role in stabilizing DE-Cad in membrane-bound aggregates as it is thought to enhance binding of DE-Cad to p120-catenin, which may serve as a cap protecting DE-Cad from being

endocytosed (Hogan et al., 2004; Hoshino et al., 2005). On the other hand, p120-catenin appears to play only a minor role in *Drosophila* (Fox et al., 2005; Myster et al., 2003; Pacquelet et al., 2003). Therefore, Rap1 must be involved in additional mechanisms to stabilize adherens junctions during furrow formation. As suggested by a recent study (Wang et al., 2013), Rap1 might mediate α-catenin-dependent coupling between adherens junctions and the actin cytoskeleton to confer to junctional stability.

Despite the accordance with previous studies (Sawyer et al., 2009), the unaffected apical accumulation of Arm in *rap1* GLC (Fig. 13) was surprising, especially since loss of DE-Cad is reported to entail loss of Arm in various tissues (Tepass et al., 1996). However, Arm is also involved in many other DE-Cad independent processes, e.g. acting as a signal molecule or transcription factor, so a requirement of DE-Cad for its localization does not appear coercive.

Albeit the precise mechanism remains to be investigated, we assume that in the absence of maternal Rap1, confinement of DE-Cad to cell membranes and accumulation into stable apical junctions is severely compromised. Instead, only fragmentary junctions are formed whose stability may vary stochastically. Thus, AJ fragmentation may affect different cells to a different degree. As a consequence, ventral cells show a broad distribution of constriction capability ranging from complete constriction to a total failure of constriction (Fig. 5O,R; Fig. 24). It may be recognized that apical constriction does not appear to be slowed down in those cells of *rap1* GLC that are capable of undergoing constriction (Fig. 5O,R; Video 2). A reason for this could be the lack of constriction in surrounding cells, so constricting cells experience considerably less opposing force from their neighbours in the epithelium. This could allow them to constrict faster and make up the inefficient actomyosin attachment in their membranes. Similarly, the lack of constriction in neighbours may allow constricting cells to constrict uniformly ("isotropically"), rather than become eccentric like wildtype cells (Fig.

5M,O). Due to the discontiguous actomyosin meshwork in the ventral epithelium, tension in the anteroposterior axis will be strongly reduced so constricting cells are not forced into an eccentric morphology. Indeed, previous work has shown that mid-ventral cells can undergo isotropic constriction when anteroposterior tension is disrupted by inflicting tears upon the supracellular actomyosin meshwork (Martin et al., 2010). Surprisingly, in spite of the large fraction of mid-ventral cells with high constriction levels, *rap1* GLC do not form a ventral furrow. We assume that the minor fraction of unconstricted and bloated mid-ventral cells has an inhibitory influence on VFF, possibly by interrupting the "predetermined breaking line".

Thus, *rap1* and *dzy* differ qualitatively in their maternal phenotypes because loss of Dzy only delays establishment of AJs whereas loss of Rap1 additionally entails a fragmentation of the AJ belt and massive cytoplasmic mislocalization of DE-Cad. This discrepancy is not in conflict with the concept of Dzy acting exclusively via Rap1, but strongly argues in favour of Rap1 being regulated by additional GEFs besides Dzy (see below).

7.1.3 A possible general role of Dzy and Rap1 in junction formation and maintenance

It must be emphasized that the effects on AJ assembly seen in *dzy* and *rap1* GLC are not confined to the prospective mesoderm but occur around the entire epithelium consistent with the localization of Dzy and Rap1 in wildtype (Fig. 16). *dzy* and *rap1* have been recognized as "ventral furrow mutants" because apical constriction of ventral cells is the earliest process in embryogenesis requiring a properly built apical AJ belt.

With the apical adhesion belt being a prominent feature of ectodermal cells, internalized mesodermal cells show substantially weaker DE-Cad intensity (Oda et al., 1998; also see Fig. 17A,H) indicating that junctions are disassembled in order to reduce cell-cell adhesion and allow mesenchymal migration. Overexpression of Dzy or $Rap1^{V12}$ impairs this mesenchymal

migration significantly, $Rap1^{V12}$ noticeably stronger than Dzy alone (Fig. 17H,I,J). This is very plausible given that Dzy works via Rap1 which is considerably reduced in the internalized mesoderm (Fig. 16K). Migration defects upon $Rap1^{V12}$ overexpression are accompanied by significantly risen relative amounts of DE-Cad in mesenchymal cells (Fig. 17) suggesting the possibility that the downregulation of Rap1 is required to allow AJs to become disassembled in the mesoderm. Accordant results have been found in the *Drosophila* testis where reduction of AJs can be restored to wildtype level through overexpression of constitutively active Rap1 (Wang et al., 2006). It remains to be seen by what mechanism AJs are disassembled in the internalized mesoderm and how the remarkably fast diminishment of Dzy and Rap1 is triggered. Conceivably, processes accompanying epithelial-to-mesenchymal transition such as mechanical alterations in the cytoskeleton could trigger degradation signals since these processes have been found to have potential signalling ability in other systems (Howard et al., 2011).

7.1.4 How are Dzy and Rap1 embedded in the cascade relaying cell signalling to morphogenesis?

As discussed above, the discrepancy between the maternal phenotypes of *dzy* and *rap1* implies the necessity of other GEFs acting on Rap1 during gastrulation. C3G is a tempting candidate as it has been shown to interact with Rap1 in mammalian cell culture as well as in *Drosophila* (Dupuy et al., 2005; Ishimaru et al., 1999). Furthermore, it exhibits GEF activity on *Drosophila* Rap1 in vitro (Shirinian et al., 2010).

In addition to uncovering alternative activators of Rap1 it will be interesting to identify players upstream of Dzy. Despite its cyclic nucleotide binding domain there is no indication so far that Dzy is activated by cAMP signalling (Kuiperij et al., 2003; Pham et al., 2000). However, like several proteins involved in cell polarity, Dzy bears a PDZ domain through

which it possibly binds to a membrane scaffold typically involved in mediating quick linkage between signalling molecules and structural proteins (Bilder, 2001). Indeed, the PDZ protein MAGI-1 has been shown to serve as a scaffold for the vertebrate homologue of Dzy (Mino et al., 2000) and is a good candidate for a protein giving the relevant spatial cue. Unravelling the architecture of such a signalling scaffold will be key to understanding how an epithelium can be reorganized so rapidly to allow the extraordinarily fast morphogenesis of the ventral furrow.

7.2 Computational modelling aids in the analyis of ventral furrow formation

Computational modelling serves as a valuable addition to the methods toolbox when investigating a complex developmental process like ventral furrow formation. In the second part of this work we adopted a well-established vertex model to computationally describe apical constriction during ventral furrow formation. We found that the ventral furrow is realistically reproduced in the model if contractility is assumed to follow a dorso-ventral gradient in the ventral epithelium and cells execute autonomous contraction dynamics. The model predicts that constriction will be anisotropic, demonstrating that cells are forced into eccentric morphology due to the physical constraints in the epithelium and do not require intrinsic polarization. Moreover, the model predicts that constriction may temporarily stagnate during the course of furrow formation leading to incremental cell area reduction. Analysis of the model revealed that this incremental area reduction occurs passively as a result of opposing forces arising from elasticity and from contraction of adjacent cells. In particular, it is not required to postulate an active stabilization mechanism to achieve incremental area reduction in the model. Analysis of *twi* mutants does not make a stabilization mechanism a mandatory postulate *in vivo*, either. Therefore, we conclude that the model presented here

serves as a promising basis for a parsimonious concept of apical constriction during ventral furrow formation.

7.2.1 Genetic definition of the spatiotemporal domain of the ventral furrow

The state-of-the-art genetic model of ventral furrow formation (Costa et al., 1994; Dawes-Hoang et al., 2005; Häcker & Perrimon, 1998; Ip & Gridley, 2002; Kölsch et al., 2007; Leptin, 1999) states that the maternal ventral fate determinant Dorsal (Dl) directs ventrally confined expression of the two zygotic ventral fate determinants Twi and Sna which function as master activators of ventral furrow formation. Twi acts through two downstream pathways (Fog/Cta and T48) to achieve the apical accumulation of RhoGEF2 which in turn triggers apical accumulation of contractile actomyosin (Dawes-Hoang et al., 2005; Kölsch et al., 2007; Nikolaidou & Barrett, 2004) (Fig. 25A). Measurements of myosin intensity in fixed or live specimen unequivocally show that actomyosin activity is not equal throughout the ventral epithelium but is higher the closer the cell is located to the ventral midline (Fig. 19F-H). In fact, the apparent heterogeneity of constriction levels prior to furrow invagination (Leptin & Grunewald, 1990; Oda & Tsukita, 2001; Fig. 20C; Video 6), i.e. cells close to the midline being noticeably more constricted than those lying further lateral, makes the notion of a contractility gradient a very reasonable concept. Considering the epistasis of ventral furrow formation (Fig. 25A), it is plausible to hypothesize that the graded expression of Twi (Leptin, 1991) might translate into the graded activation of Fog (Costa et al., 1994), and indirectly of RhoGEF2 and finally myosin (Figs. 19F-H, 25A). A simple alternative hypothesis to explain actomyosin contraction being present in ventral cells but absent in lateral cells, would be a sharp border separating contractile from non-contractile cells – possibly mediated by the cutoff-like expression pattern of Sna (Leptin, 1991). As shown in our model, this hypothesis leads to an artificial morphology and does not match live data (Fig. 20A). We therefore

propose that contractility in the ventral epithelium follows a gradual pattern *in vivo*, as predicted by the computational model and supported by myosin intensity measurements. A similar contraction probability gradient has also been hypothesized in a previous computational approach (Driquez et al., 2011). The molecular role of Sna in ventral furrow formation is still enigmatic since its known function of repressing neuroectodermal genes gives no explanation why Sna is absolutely critical for apical actomyosin localization and shape change in ventral cells (Ip & Gridley, 2002; Leptin & Grunewald, 1990; Martin et al., 2009) (Fig. 25A).

Twi has been proposed to serve an additional, albeit uncharacterized, function during ventral furrow formation since upon *twi*-RNAi cell stabilization was supposed be specifically lost: cells now wildly oscillate between constriction and dilation as though being unable to stabilize their partly constricted surface (Martin et al., 2009). We cannot, however, reproduce this phenotype in *twi* mutants. Instead, we find that cell constriction is largely abolished since only a subset of ventral cells undergoes area reduction reaching varying degrees of constriction; in any case, we do not find cells to execute oscillations that would be more excessive than in wildtype (Fig. 23A; Video 14) Thus, it appears questionable whether a specific loss of such a postulated stabilization mechanism is unambiguously evident based on the *twi* phenotype. Interestingly, the *twi* phenotype can be reproduced in our computational model if contractility is randomly reduced across the cell sheet mimicking the weak, fragmentary apical myosin localization in *twi* mutants (Fig. 23C). These data suggest that incomplete apical myosin accumulation can explain the defects in cell constriction seen in *twi* mutants. The remaining, fragmentary apical myosin localization seen in *twi* (Fig. 23B-3) must be brought about through Sna via an unexplored mechanism (Fig. 25A) since no apical myosin is seen in *sna twi* double mutants at any time (not shown). Consequently, we favour to stick to the genetic model in Fig. 25A as it sufficiently accounts for results gained from both

experimental and modelling approaches so far. In particular, we prefer not to postulate an additional role of Twi in stabilization of contracting actomyosin since we feel that the phenotype does not make this conclusion sufficiently coercive. In fact, our vertex model

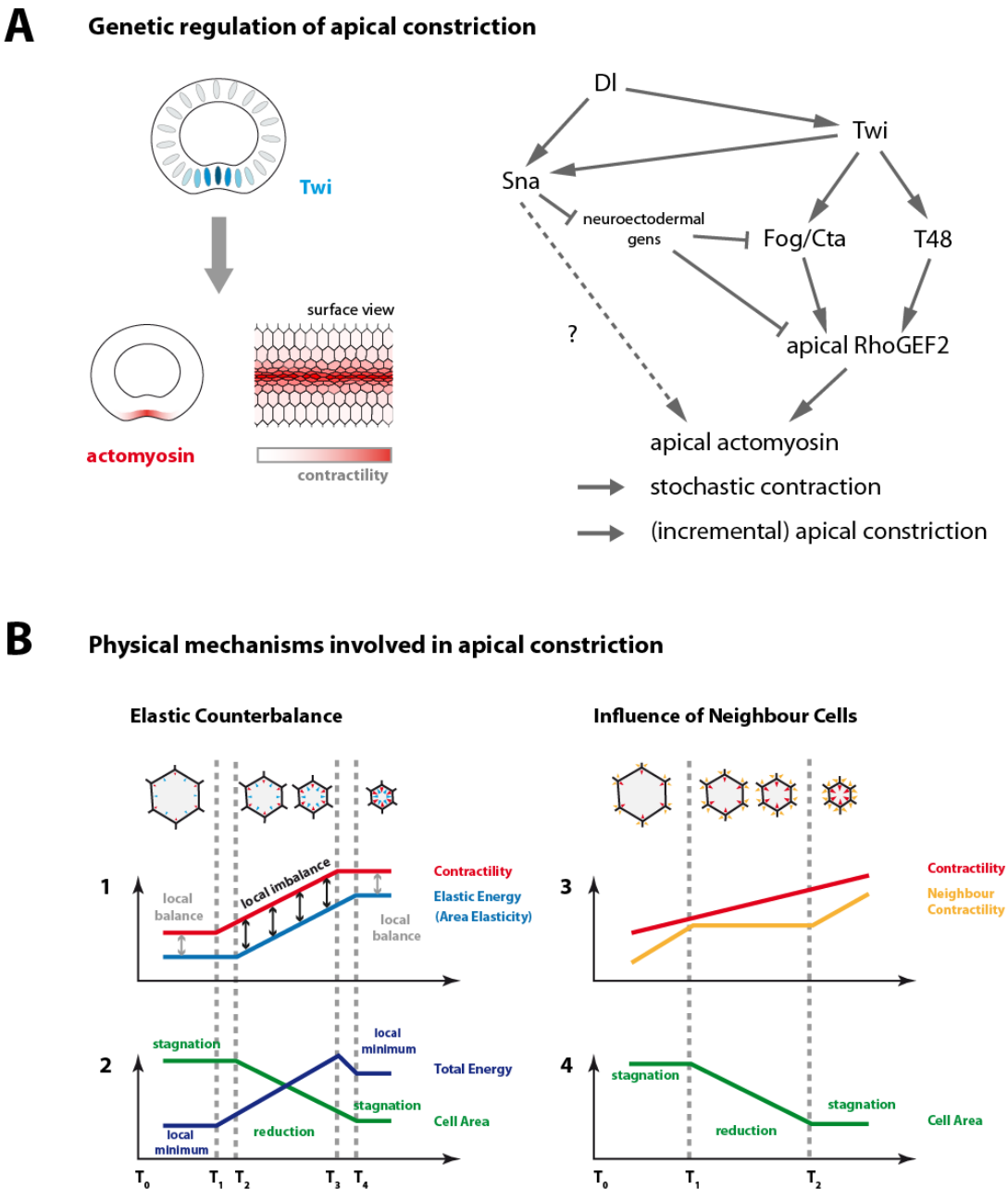

Fig. 25: Proposed mechanisms driving apical constriction during ventral furrow formation. A: Genetic cascade leading from the ventral determinant Dorsal *(*Dl*)* to shape change of ventral cells (right). Twi activates downstream targets leading to the apical accumulation of contractile actomyosin. Stochastic actomyosin contractions then reduce apical cell area. Area reduction may exhibit an incremental fashion due to stochastic

interplay with opposing forces (see B). We suppose that the graded expression of Twi may translate into graded accumulation of apical actomyosin and thus graded contractility (left). Twi also enhances Sna expression, but the Sna-dependent contribution to apical actomyosin assembly (seen in *twi PE::sna* mutants, Fig. 23B) remains to be resolved. **B:** Two physical mechanisms contributing to incremental area reduction, as suggested by the computational model: Intrinsic elastic counterbalance (left) and extrinsic contractive counterforce exerted by neighbour cells (right). Both mechanisms may work alternatively or in concert to cause temporary stagnations in area reduction. Left: As long as contractile and elastic forces are balanced, cell area remains constant (1,2: T_0 to T_1). When contractility begins to rise (1: T_1), the cell responds by reducing its area after a short delay (2: T_2). As a consequence of this area reduction, i.e. compression, elastic energy begins to rise (1: T_2). When contractility has ceased to rise (1: T_3), the cell arrives at a new area level where contractile and elastic forces are in balance and total energy is locally minimized (1,2: T_4). Right: Contractive forces exerted by neighbouring cells can temporarily outweigh the contractive force in the central cell preventing net area reduction (1,2: T_0 to T_1 and T_2 onwards). In the graph, "neighbour contraction" refers to the average contractive forces taken over all adjacent cells.

demonstrates that incremental area reduction occurs in a frequency comparable to *in vivo* and without rigorous direct regulation of alternating contraction and stabilization periods. Thus, in order to minimize complexity and to keep the genetic model parsimonious, it should first be considered whether occasional stagnation periods seen in live-imaging analysis could be merely physical phenomena as suggested by our model (Fig. 25B) rather than manifestations of a genetically controlled mechanism.

7.2.2 Self-regulatory considerations of apical constriction

We suggest that the joint constriction of a band of cells in the epithelium seen during ventral furrow formation is best regarded as the outcome of stochastic autonomous contractions which are genetically constrained to a short time-slot and to a limited spatial domain. A genetic cascade facilitates a gradual apical accumulation of contractile actomyosin which contracts in a stochastic fashion to reduce apical cell area. These contractions are carried out

autonomously in each cell and are opposed by elastic resistance within the cell as well as by contractions of neighbouring cells. As our model shows, no further regulatory input like a ratchet mechanism is required to achieve joint cell constriction in the epithelium with occasional stagnation of area reduction in individual cells. Laser ablation experiments could possibly help to quantify the extent by which adjacent cells affect each other's shape change *in vivo*. Similar experiments had shown that mechanical coupling between contracting cells in the amnioserosa largely affect shape changes of adjacent cells during dorsal closure (Solon et al., 2009).

It has not been fully understood what mechanical role the joint apical constriction plays for tissue invagination. Absent or severely disturbed apical constriction as seen in *sna*, *twi, RhoGEF2* or *rap1* mutants prevents tissue invagination (Häcker & Perrimon, 1998; Leptin & Grunewald, 1990; Spahn et al., 2012). However, computational approaches have suggested that apical constriction alone is not sufficient to achieve furrow invagination since the lateral epithelium may in fact be a critical driving force to guarantee regular tissue internalization (Conte et al., 2009; Conte et al., 2012). Joint apical constriction may cause a small indentation in the ventral epithelium which will subsequently act as a weak spot or predetermined breaking line allowing quick tissue invagination by the sudden release of pressure in the epithelium. Computational modelling highlights the importance of a physical perspective when studying tissue morphogenesis and shows that only a minimal genetic regulation may be required to drive complex processes in embryonic development. Thus, extension of the vertex model into the third dimension will be a promising endeavour to investigate this process and will further elucidate the mechanisms by which tissues undergo a massive morphogenetic movement like ventral furrow formation.

8 MATERIALS & METHODS

8.1 Fly stocks and genetics

dzy$^{\Delta 1}$, *dzy*$^{\Delta 8}$, *dzy*$^{\Delta 12}$ (Huelsmann et al., 2006), *dzy-GFP* (*dPDZ-GEF*^{EGFP}) and *UAS-dzy* (*UAS-dPDZ-GEF*^{EGFP}) (Boettner & Van Aelst, 2007), *Df(2L)ED380* (Ryder et al., 2007), *spider-gfp* (Morin et al., 2001), *DE-Cad:GFP* (*ubi-DE-Cad-GFP)* (Oda & Tsukita, 2001), hsFLP1.22; *FRT*$^{2L\text{-}40A}$ and *hsFLP1.22; ovo*$^{D13L\text{-}2X48}$ *FRT*$^{3L\text{-}2A}$ (Chou et al., 1993; Chou & Perrimon, 1992), *da-gal4* (Hinz et al., 1994), *twi-gal4* (Giebel et al., 1997), *UAS-rap1*^{V12} (Boettner et al., 2003); *rap1-gfp* and *rap1*$^{P[5709]}$*FRT*$^{3L\text{-}2A}$ (Knox & Brown, 2002). *sqh:mCherry* (Martin et al., 2009) (*spaghetti-squash (sqh)* encoding myosin regulatory light chain); *twi*^{EY53} (Simpson, 1983); *P[sna*$_g$*]* (Brönner et al., 1994) (*PE::sna,* this construct drives *sna* expression using a *twi*-independent enhancer element, so a *twi* loss-of-function will not be superimposed by additional partial loss of *sna)*.

The analysis of *dzy* GLC was performed with either of the *dzy* alleles, since no difference was visible in their phenotypes. They are considered *dzy* nulls since GLC of the deficiency *Df(2L)ED380* show the same early embryonic phenotype (not shown). The DE-Cad:GFP fusion protein provides full DE-Cadherin function and does not elicit any adverse effects on embryogenesis or viability (Oda & Tsukita, 2001). *rap1*$^{P[5709]}$ is an insertion of P{lacW} into *rap1* deleting the C-terminal 37 amino acids including the GTP binding sequence and the prenylation site (N. Brown, personal communication). GLC were produced according to standard methods (Chou & Perrimon, 1992). Flies were reared and crossbred following standard procedures.

8.2 Staging of embryos

Developmental stages were distinguished following Campos-Ortega & Hartenstein (1985). For the fine temporal staging during VFF we distinguished an early (6e), a middle (6m) and a late stage 6 (6l) based on the position of the pole cells, as documented in Fig. 4.

8.3 Immunohistochemistry and *in situ* hybridization

Embryos were fixed by heat-methanol treatment (modified after Müller & Wieschaus (1996)) or by 3.7% formaldehyde according to standard procedures. Primary antibodies: mouse anti-Arm (N2 7A1; 1:100; *DSHB*); rat anti-DE-Cad (DCAD2; 1:100; *DSHB*); sheep anti-DIG-AP (1:2000; *Roche*); rabbit anti-Eve (1:2000; Frasch et al., 1987); rabbit anti-GFP (1:2000; *Molecular Probes*); mouse anti-Nrt (BP106; 1:10; *DSHB*); rabbit anti-Sna (1:2000; Reuter & Leptin, 1994); rabbit anti-Twi (1:5000; Roth et al., 1989); rabbit anti-Zip (1:1000; Kiehart & Feghali, 1986); *zipper* encoding myosin II). rabbit anti-RhoGEF2 (1:10000; Großhans et al., 2005). mouse anti-Lamin (LMN1; 1:20; *DSHB*). Secondary antibodies, labelled with Alexa 488 (*Molecular Probes*), Cy3 or biotin (*Jackson Labs*), were used at 1:500. DAPI (1:3000 of a 5 mg/ml stock; *Sigma*) was used to visualize nuclei. The signal of the biotinylated antibodies was enhanced using Vectastain 'ABC Elite Kit' (1:100; *Vector Laboratories*) and detected with H_2O_2 (0.003%; *Fluka*) and 3,3'-diaminobenzidine (DAB, 0.25mg/ml; *Sigma*) for a brown staining, with the same reagents in combination with 0.01% $NiCl_2$ and 0.01% $CoCl_2$ to create a blue staining. Alexa 594-conjugated phalloidin (*Molecular Probes*) was used at 1 U/ml.

In situ hybridization was performed essentially as described in (Tautz & Pfeifle, 1989). DIG-labelled *pannier* (*pnr*) (Ramain et al., 1993) and *huckebein (hkb)* (Brönner et al., 1994) RNA probes were generated from full-length cDNA clones in pNB40 (Brown & Kafatos, 1988).

Fluorescently labelled cross sections were mounted in Aqua-PolyMount (*Polysciences*). For cross sectioning embryos were cut manually with a syringe needle. Sections were imaged at 50% egg length. Confocal images were taken on a *Leica* SP2 confocal system on an inverted *Leica* DM IRBE microscope. For bright-field microscopy embryos were mounted in araldite and analyzed on an Axioplan 2 (*Zeiss*) equipped with a ProgRes C14 camera (*Jenoptik*).

8.4 Embryo permeabilization and drug application

Standard permeabilization protocols proved inappropriate for young (stage 1-5) embryos as they would not survive the toxic heptane treatment. Instead, an alternative protocol was developed, adopting a recently published method (Rand et al., 2010): After normal bleaching, embryos were transferred into a limonene containing wash buffer (*Kaloverta Lemon3*, 1:10 in ddH_2O) and incubated for 1 minute with gentle rocking and subsequently washed by rinsing 4x in standard phosphate buffer saline (PBS). To control successful permeabilization, embryos were optionally incubated in 1 mM rhodamine B (*Sigma*) for 5 min on a shaker, followed by rinsing 4x in PBS. Embryos were then set on a nitex basket and suspended in a petri dish containing 4 ml 0.2 mM chlorpromazine (*Sigma*) for 10 minutes before being mounted for imaging.

8.5 Microscopy

For time-lapse recordings dechorionated embryos were glued with their dorsal side to a slide (for surface-view confocal imaging) or positioned with their lateral side on a slide (for side-view brightfield imaging). They were mounted with a drop of water-saturated 3S Voltalef oil under a cover slip supported by two cover slips on each side. Image series were recorded using a *Leica SP2* confocal system for fluorescence or a *Zeiss Axioplan 2* equipped with a *SPOT Insight* camera for bright-field microscopy; the images were assembled to movies using

Photoshop CS5 and *QuickTime Player Pro*. For confocal live-imaging, image series were started as soon as the cellularization front had reached the yolk. Images were taken with 8 or 12 seconds/frame at a focal place of 2 µm below the apical surface.

For embryo live-imaging in cross-sectional view ("End-on imaging") embryos were individually mounted on a slide, basically following a procedure given in Witzberger et al. (2008): A 2.5% agarose solution was prepared and allowed to cool down to 80°C on a heating block. 200 µl were pipetted into a small self-made chamber (2.5 x 1.5 x 0.2 cm). A special "micro-comb", made by attaching short pieces of wire (0.2 mm diameter) to a holder at a right angle, was quickly put onto the agarose solution in the chamber to produce tiny holes in the gel after the solution had cured. These micro-gels were stored at 4°C in a petri dish with a wet piece of cloth included to prevent desiccation. For imaging, the gel was placed on a slide, and single embryos were mounted headlong into a hole in the gel using a fine brush. A drop of 3S Voltalef oil was put on the mounted embryo, and a long cover slip (22 x 55 mm) was placed over the gel, supported by two small pieces of modelling clay on either side of the gel to avoid squishing the embryo. End-on imaging was conducted on a LSM 510 (*Zeiss*).

8.6 Image quantification and statistical analysis

For automated cell tracking we developed custom scripts in MATLAB (MathWorks). Using low pass and high pass filtering, thresholding and built-in morphological operations, images were segmented to 1-pixel-thick cell outlines. Distances of cell centres between two subsequent images in the series were used as criterion to identify corresponding cells in the series. For each tracked cell pixel area and eccentricity was measured at each timepoint. Cell eccentricity was defined as the ratio of the major and minor axis of the ellipse that best fits the

cell. For plotting, area and eccentricity time series were smoothened using a Gaussian kernel (window: 1.5 time points) to reduce noise.

Apicobasal intensity profiles along membranes (Fig. 9) were measured using IPLab (Scanalytics) by manually drawing 1-pixel-thick linear ROIs along each membrane. For plotting, measurements were smoothened using a running average filter (window: +/- 10 data points).

For assessing signal diminishment of Dzy:GFP / Rap1:GFP (Fig. 16) or DE-Cad (Fig. 17) in the mesoderm, both mesodermal and ectodermal cells were marked manually in IPLab and mean pixel intensities were measured. Intensity measurements with manual ROIs were done in IPLab (Scanalytics). To quantify mesodermal spreading and clumping (Fig. 17), linear ROIs were drawn manually using IPLab according to the schemes in Fig. 17, and ROI lengths were measured. To check for significance, R software (R Foundation for Statistical Computing) was used to apply nonparametric Wilcoxon rank sum tests.

To count the number of floating DE-Cad:GFP particles in live recordings (Fig. 15), raw images were cropped to a defined size and analyzed in ImageJ (NIH). After background subtraction and manual thresholding (under visual control with the raw images) particles were extracted and automatically counted with the "Analyze Particles" command. For each sample, an image series spanning two minutes real-time (10 images) was analyzed this way. To quantify the ratio of cytoplasmic and membrane DE-Cad:GFP intensity, raw images were first segmented using MATLAB scripts and cropped to a defined size. Cell outlines were then expanded to two pixel width and mapped onto the raw images. Total membrane and total cytoplasmic intensities were then obtained by measuring mean pixel intensity only in the area covered, or not covered, by the outline overlay, respectively. The ratio of both intensities was followed over a time span of 50 frames (10 minutes real-time, starting at completion of

cellularization). To reduce measurement artefacts due to the apical position of nuclei at the onset of gastrulation (so the imaging plane shows the nucleus rather than the cytoplasm), only the average of the final 5 frames (1 minute real-time) in the series was considered for evaluation. Images had not been modified by filtering, levels or contrast adjustment prior to this analysis. Nonparametric Wilcoxon rank sum tests, as implemented in R software (*R Foundation for Statistical Computing*), were used to check for significance.

8.7 3D reconstructions of epithelial cells

Confocal image stacks of fixed embryos, stained against a membrane marker (Nrt/Spider:GFP/DE-Cad:GFP), were acquired on a DM IRBE (*Leica*) at a resolution of 0.6 µm per slice. The image stack was segmented using the MATLAB scripts we had developed for live-imaging analysis (see above) to break the raw images down into black-and-white images showing cell outlines only. With these cell outlines, individual cells could be easily reconstructed in 3D using Amira software (Visage Imaging). For slices at the apical or basal end where segmentation often proves difficult, cell outlines were marked manually using the raw images. For nuclear 3D reconstruction, embryos double-stained against membrane and nucleus (anti-Lamin staining), were imaged. Nuclear depth and cell area per slice were computed using built-in functions of Amira.

8.8 Biophysical modelling

In order to model cell shape change during ventral furrow formation we set-up a variant of a commonly used vertex model (compare e.g.: Farhadifar et al., 2007; Landsberg et al., 2009; Osterfield et al., 2013; Rauzi et al., 2008) to describe epithelia during development. The corresponding energy function is explained in Figs. 18,19. Parameter values were chosen to

reproduce the cell morphology seen in live-recordings (K = 2.5, Λ = 0.2, κ = 0.15). Alternative parameter values lead to aberrant morphology and are documented in Videos 9, 10. Preferred area (for area elasticity) and preferred edge length are equal for all cells and correspond to the initial state of the model (regular hexagonal sheet).

For the cutoff model contractility (Γ) was modelled by setting Γ = 10 in five central cell rows and Γ = 0 on the remaining sheet. For the gradient model contractility was modelled using the function $\Gamma(i,j) = \Gamma_Z \cdot \exp\left[-(i-Z)^2/(2\sigma^2)\right]$ with Γ_Z being contractility in the midline (= central cell row *Z*) (Γ_Z = 15), *i* the cell row (dorso-ventral coordinate) and *j* the cell column (antero-posterior coordinate) and σ the width parameter of the gradient (σ = 1.75). To introduce time-dependence in the cutoff model, we use $\Gamma(t) = \gamma_0 + \gamma_1 \cdot t$ in the five central cell rows and $\Gamma(t) = 0$ elsewhere (γ_0 = 0, γ_1 = 0.15). Time-dependence in the gradient model was achieved by using $\Gamma(i,j,t) = (\gamma_0 + \gamma_1 \cdot t) \cdot \exp\left[-(i-Z)^2/(2\sigma^2)\right]$. The linear term was bounded by $\Gamma_{max} = 25$ to avoid unlimited increase of contractility. Finally, autonomous stochastic dynamics were implemented in the time-dependent gradient model by adding Brownian motion to the contractility function via

$$\Gamma(i,j,t) = (\gamma_0 + \gamma_1 \cdot t + \gamma_2 \cdot W_t(i,j)) \cdot \exp\left[-(i-Z)^2/(2\sigma^2)\right]$$

where $W_t(i,j)$ represents a path of a standard Wiener process, drawn independently for each cell (γ_2 = 0.3). To model incomplete apical myosin accumulation in *twi PE::sna* mutants, contractility in the formula above was modified via $\tilde{\Gamma}(i,j,t) = \Gamma(i,j,t) \cdot U(i,j)$ with *U(i,j)* being a uniform random number between 0.0 and 0.5, drawn independently for each cell.

To derive the equation of motion for each vertex, we assume balance between frictional force and potential force as described previously in Nagai & Honda (2001). The equations are numerically integrated using an explicit Euler scheme. Boundary vertices remain fixed

through time. At the left and right margins of the sheet two cell columns are set non-contractile ($\Gamma = 0$ throughout) to delimit the anterior and posterior borders of the furrow. To reduce border artefacts, line tension (Λ) is set to 6.0 in all cells of the non-contractile margin. If the distance between two vertices falls below a critical threshold *eps* (*eps* = 0.1), they undergo a swapping process ("T1 transition") by changing connections with adjacent vertices (see Fig. 2 in Nagai & Honda (2001), Fig. 1b in Rauzi et al. (2008) or Fig. S1 in Farhadifar et al. (2007). Standard size of the cell sheet is 13x24 cells (cropped only for illustration purpose). If not stated otherwise, simulation runs stop as soon as cells from the three central cell rows (without the non-contractile margin) have, on average, reduced their area to a certain fraction *w* of their initial area (*w* = 0.33, based on measurements *in vivo*), marking completion of furrow formation and onset of invagination *in vivo*. Real-time designations in the model are obtained by normalizing the time-steps required to reach completion of furrow formation to real-time in live-recordings (10 minutes). Area designations in the model are obtained by normalizing the pixel area of the initial regular hexagon to the average area of cells at the end of cellularization *in vivo*. The model is implemented as a MATLAB script (The MathWorks).

9 VIDEO LEGENDS

Video 1. Initial speed of germ band extension is unaffected in and *dzy* and *rap1* germline clones. When VFF commences, pole cells are internalized into the embryo through the PMG invagination. In *dzy* (middle) and *rap1* (bottom) they are invaginated within essentially the same time as in wildtype. Video accelerated 120x, covering about 22 min real-time; anterior left.

Video 2. Apical constriction is affected in *dzy* and *rap1* germline clones. Detail ventral surface views of wildtype, *dzy* and *rap1* GLC expressing Spider:GFP to mark cell membranes. In *dzy* apical constriction is slowed down. In *rap1*, apical constriction varies among ventral cells, and a subset remains unconstricted. Video accelerated 72x, covering 23 min real-time starting at completion of cellularization; wildtype video was stopped when the furrow had closed after 13 min; anterior left; focal plane 5 µm below cell surface; scale bar: 10 µm.

Video 3. Ventral furrow formation is compromised in *dzy* and *rap1* germline clones. Ventral whole views of wildtype, *dzy* and *rap1* GLC expressing Spider:GFP. In *dzy* the ventral furrow has formed too late, fails to close and opens up again. In *rap1* a furrow does not form at any time. Video accelerated 120x, covering 39 min real-time starting at completion of cellularization; wildtype video stopped after 16 min, *rap1* video stopped after 24 min; anterior left; focal plane 5 µm below cell surface; frames show 187 µm in width.

Video 4. DE-Cad is improperly localized in *rap1* germline clones. Detail ventral surface views of wildtype, *dzy* and *rap1* GLC expressing DE-Cad:GFP. In *rap1,* DE-Cad rich particles are formed and float through the cytoplasm. These particles are not restricted to ventral cells, as shown here, but arise everywhere in the epithelium. Video accelerated 72x, covering 10 min; ventral view, grazing section at 5µm depth, anterior left, scale bar: 10 µm.

Video 5. Live-recording of ventral furrow formation in cross-sectional view. Wildtype embryo expressing DE-Cad:GFP, mounted upright on a slide. Prior to gastrulation, the embryo undergoes cellularization with cell membranes growing from apical towards basal to enclose individual nuclei. After completion of cellularization DE-cadherin accumulates in the apical membranes, and ventral cells constrict their apices leading to the formation of the

furrow. Subsequently, the furrow folds inwards and becomes invaginated. Imaging plane 160 μm below the posterior pole. Time in minutes relative to onset of ventral furrow formation.

Video 6: Ventral furrow formation. Confocal live-recording of the ventral epithelium of a *Drosophila* embryo expressing Spider:GFP to mark cell membranes. Imaging plane 2 μm below the apical surface. Video accelerated 120x, spanning 10 minutes real-time.

Video 7: Cutoff Model. Model of ventral furrow formation using a cutoff contractility function (temporally constant) and standard parameters ($\Gamma = 10$ in contractile cells, $\Gamma = 0$ in non-contractile cells, $K = 2.5$, $\Lambda = 0.2$, $\kappa = 0.15$).

Video 8: Gradient Model. Model of ventral furrow formation using a gradient contractility function (temporally constant) and standard parameters ($\Gamma_Z = 15$ in the ventral midline, $K = 2.5$, $\Lambda = 0.2$, $\kappa = 0.15$).

Video 9: Alternative energy parameters in the Cutoff Model. Models of ventral furrow formation using a cutoff contractility function (temporally constant) and alternative energy parameters. Upper left: standard parameters ($\Gamma = 10$, $K = 2.5$, $\Lambda = 0.2$, $\kappa = 0.15$). Lower left: Low contractility ($\Gamma = 5$); less constriction is achieved before force balance is reached. Upper central: Low line tension ($\Lambda = 0.005$). Lower central: High line tension ($\Lambda = 6.0$); constricting cells avoid stretching of edges and maintain a round morphology. Upper right: High line elasticity ($\kappa = 0.02$); cell edges become excessively compressed leading to a diamond morphology. Lower right: Low line elasticity ($\kappa = 0.4$); constricting cells avoid compression of edges leading to a brick-like morphology.

Video 10: Alternative energy parameters in the Gradient Model. Models of ventral furrow formation using a gradient contractility function (temporally constant) and alternative

energy parameters. Upper left: standard parameters (Γ_Z= 15, K = 2.5, Λ = 0.2, κ = 0.15). Lower left: Low contractility (Γ_Z = 7.5); less constriction is achieved before force balance is reached. Upper central: Low line tension (Λ = 0.005). Lower central: High line tension (Λ = 6.0); constricting cells avoid stretching of edges and maintain a round morphology. Upper right: High line elasticity (κ = 0.02); cell edges become excessively compressed leading to a diamond morphology. Lower right: Low line elasticity (κ = 0.4); constricting cells avoid compression of edges leading to a brick-like morphology.

Video 11: Time-dependent Gradient Model. Model of ventral furrow formation using a time-dependent gradient contractility function (see Materials & Methods) and standard parameters (K = 2.5, Λ = 0.2, κ = 0.15).

Video 12: Stochastic time-dependent Gradient Model. Model of ventral furrow formation using a time-dependent gradient contractility function with stochastic fluctuations (see Materials & Methods) (K = 2.5, Λ = 0.2, κ = 0.15).

Video 13: Stochastic time-dependent Gradient Model, with contractility coded by colour. Same model as in Video 12. Stochastic cell contractility is coded by colour, ranging from white (zero contractility) to dark red (maximum contractility).

Video 14: Phenotype of *twi* mutants. Confocal live-recording of the ventral epithelium of a *twi* mutant embryo (*twi PE::sna*) expressing Spider:GFP to mark cell membranes. Imaging plane 2 µm below the apical surface. Video accelerated 120x, spanning 20 minutes real-time.

Video 15: *twi* Model. Model of ventral furrow formation in *twi* mutants using random reduction of contractility across the cell sheet (see Materials & Methods) (K = 2.5, Λ = 0.2, κ = 0.15).

10 REFERENCES

Asha, H., de Ruiter, N., Wang, M., & Hariharan, I. (1999). The Rap1 GTPase functions as a regulator of morphogenesis in vivo. *EMBO J, 18*, 605-615.

Barrett, K., Leptin, M., & Settleman, J. (1997). The Rho GTPase and a putative RhoGEF mediate a signaling pathway for the cell shape changes in Drosophila gastrulation. *Cell, 91*(7), 905-915.

Bilder, D. (2001). PDZ proteins and polarity: functions from the fly. *Trends Genet, 17*(9), 511-519.

Boettner, B., Harjes, P., Ishimaru, S., Heke, M., Fan, H., Qin, Y., et al. (2003). The AF-6 homolog canoe acts as a Rap1 effector during dorsal closure of the Drosophila embryo. *Genetics, 165*(1), 159-169.

Boettner, B., & Van Aelst, L. (2007). The Rap GTPase activator Drosophila PDZ-GEF regulates cell shape in epithelial migration and morphogenesis. *Mol Cell Biol, 27*(22), 7966-7980.

Boettner, B., & Van Aelst, L. (2009). Control of cell adhesion dynamics by Rap1 signaling. *Curr Opin Cell Biol, 21*(5), 684-693.

Brodland, G. W., Conte, V., Cranston, P. G., Veldhuis, J., Narasimhan, S., Hutson, M. S. et al. (2010). Video force microscopy reveals the mechanics of ventral furrow invagination in Drosophila. *Proc Natl Acad Sci U S A, 107*(51), 22111-22116.

Brönner, G., Chu-LaGraff, Q., Doe, C. Q., Cohen, B., Weigel, D., Taubert, H., et al. (1994). Sp1/egr-like zinc-finger protein required for endoderm specification and germ-layer formation in Drosophila. *Nature, 369*(6482), 664-668.

Brown, N., & Kafatos, F. (1988). Functional cDNA libraries from Drosophila embryos. *J Mol Biol, 203*, 425-437.

Campos-Ortega, J., & Hartenstein, V. (1985). The embryonic development of Drosophila melanogaster. *Springer Verlag, Berlin, Heidelberg*.

Chou, T. B., Noll, E., & Perrimon, N. (1993). Autosomal *P[ovoD1]* dominant female-sterile insertions in *Drosophila* and their use in generating germ-line chimeras. *Development, 119*, 1359-1369.

Chou, T. B., & Perrimon, N. (1992). Use of a yeast site-specific recombinase to produce female germline chimeras in Drosophila. *Genetics, 131*(3), 643-653.

Conte, V., Muñoz, J. J., Baum, B., & Miodownik, M. (2009). Robust mechanisms of ventral furrow invagination require the combination of cellular shape changes. *Phys Biol, 6*(1), 016010.

Conte, V., Ulrich, F., Baum, B., Munoz, J., Veldhuis, J., Brodland, W., et al. (2012). A biomechanical analysis of ventral furrow formation in the Drosophila melanogaster embryo. *PLoS One, 7*(4), e34473.

Costa, M., Wilson, E., & Wieschaus, E. (1994). A putative cell signal encoded by the folded gastrulation gene coordinates cell shape changes during Drosophila gastrulation. *Cell, 76*, 1075-1089.

Dawes-Hoang, R., Parmar, K., Christiansen, A., Phelps, C., Brand, A., & Wieschaus, E. (2005). *folded gastrulation*, cell shape change and the control of myosin localization. *Development, 132*(18), 4165-4178.

de Beco, S., Gueudry, C., Amblard, F., & Coscoy, S. (2009). Endocytosis is required for E-cadherin redistribution at mature adherens junctions. *Proc Natl Acad Sci U S A, 106*(17), 7010-7015.

de Rooij, J., Boenink, N., van Triest, M., Cool, R., Wittinghofer, A., & Bos, J. (1999). PDZ-GEF1, a guanine nucleotide exchange factor specific for Rap1 and Rap2. *J Biol Chem, 274*(53), 38125-38130.

Desai, R., Sarpal, R., Ishiyama, N., Pellikka, M., Ikura, M., & Tepass, U. (2013). Monomeric alpha-catenin links cadherin to the actin cytoskeleton. *Nat Cell Biol, 15*(3), 261-273.

Drees, F., Pokutta, S., Yamada, S., Nelson, W. J., & Weis, W. I. (2005). Alpha-catenin is a molecular switch that binds E-cadherin-beta-catenin and regulates actin-filament assembly. *Cell, 123*(5), 903-915.

Driquez, B., Bouclet, A., & Farge, E. (2011). Mechanotransduction in mechanically coupled pulsating cells: transition to collective constriction and mesoderm invagination simulation. *Phys Biol, 8*(6), 066007.

Dupuy, A. G., L'Hoste, S., Cherfils, J., Camonis, J., Gaudriault, G., & de Gunzburg, J. (2005). Novel Rap1 dominant-negative mutants interfere selectively with C3G and Epac. *Oncogene, 24*(28), 4509-4520.

Farhadifar, R., Roper, J. C., Aigouy, B., Eaton, S., & Julicher, F. (2007). The influence of cell mechanics, cell-cell interactions, and proliferation on epithelial packing. *Curr Biol, 17*(24), 2095-2104.

Fox, D., Homem, C., Myster, S., Wang, F., Bain, E., & Peifer, M. (2005). Rho1 regulates Drosophila adherens junctions independently of p120ctn. *Development, 132*(21), 4819-4831.

Frasch, M., Hoey, T., Rushlow, C., Doyle, H., & Levine, M. (1987). Characterization and localization of the *even-skipped* protein of Drosophila. *EMBO J, 6*(3), 749-759.

Garcia-Mata, R., & Burridge, K. (2007). Catching a GEF by its tail. *Trends Cell Biol, 17*(1), 36-43.

Gates, J., & Peifer, M. (2005). Can 1000 reviews be wrong? Actin, alpha-Catenin, and adherens junctions. *Cell, 123*(5), 769-772.

Gauch, J., Hugh G. (2003). Scientific Method in Practice. *Cambridge University Press*.

Gelbart, M. A., He, B., Martin, A. C., Thiberge, S. Y., Wieschaus, E. F., & Kaschube, M. (2012). Volume conservation principle involved in cell lengthening and nucleus movement during tissue morphogenesis. *Proc Natl Acad Sci U S A, 109*(47), 19298-19303.

Giebel, B., Stuttem, I., Hinz, U., & Campos-Ortega, J. A. (1997). Lethal of scute requires overexpression of Daughterless to elicit ectopic neuronal development during embryogenesis in Drosophila. *Mech Devel, 63*(1), 75-87.

Großhans, J., Wenzl, C., Herz, H., Bartoszewski, S., Schnorrer, F., Vogt, N., et al. (2005). RhoGEF2 and the formin Dia control the formation of the furrow canal by directed actin assembly during Drosophila cellularisation. *Development, 132*(5), 1009-1020.

Häcker, U., & Perrimon, N. (1998). DRhoGEF2 encodes a member of the Dbl family of oncogenes and controls cell shape changes during gastrulation in Drosophila. *Genes Dev, 12*, 274-284.

Hinz, U., Giebel, B., & Campos-Ortega, J. (1994). The basic helix-loop-helix domain of Drosophila lethal of scute protein is sufficient for proneural function and activates neurogenic genes. *Cell, 76*(1), 77-87.

Hočevar, A., & Ziherl, P. (2011). Collective mechanisms of embryogenesis: Formation of ventral furrow in Drosophila. *arXiv: 1108.4795v1 [q-bio.CB]*. Epub Date: 24-Aug-2011

Hočevar Brezavšček, A., Rauzi, M., Leptin, M., & Ziherl, P. (2012). A model of epithelial invagination driven by collective mechanics of identical cells. *Biophys J, 103*(5), 1069-1077.

Hogan, C., Serpente, N., Cogram, P., Hosking, C. R., Bialucha, C. U., Feller, S. M., et al. (2004). Rap1 regulates the formation of E-cadherin-based cell-cell contacts. *Mol Cell Biol, 24*(15), 6690-6700.

Hoshino, T., Sakisaka, T., Baba, T., Yamada, T., Kimura, T., & Takai, Y. (2005). Regulation of E-cadherin endocytosis by nectin through afadin, Rap1, and p120ctn. *J Biol Chem, 280*(25), 24095-24103.

Howard, S., Deroo, T., Fujita, Y., & Itasaki, N. (2011). A positive role of cadherin in Wnt/beta-catenin signalling during epithelial-mesenchymal transition. *PLoS One, 6*(8), e23899.

Huelsmann, S., Hepper, C., Marchese, D., Knöll, C., & Reuter, R. (2006). The PDZ-GEF Dizzy regulates cell shape of migrating macrophages via Rap1 and integrins in the Drosophila embryo. *Development, 133*(15), 2915-2924.

Hunter, C., & Wieschaus, E. (2000). Regulated expression of nullo is required for the formation of distinct apical and basal adherens junctions in the Drosophila blastoderm. *J Cell Biol, 150*(2), 391-401.

Ip, Y. T., & Gridley, T. (2002). Cell movements during gastrulation: snail dependent and independent pathways. *Curr Opin Genet Dev, 12*(4), 423-429.

Ishimaru, S., Williams, R., Clark, E., Hanafusa, H., & Gaul, U. (1999). Activation of the Drosophila C3G leads to cell fate changes and overproliferation during development, mediated by the RAS-MAPK pathway and RAP1. *EMBO J, 18*, 145-155.

Kafer, J., Hayashi, T., Maree, A. F., Carthew, R. W., & Graner, F. (2007). Cell adhesion and cortex contractility determine cell patterning in the Drosophila retina. *Proc Natl Acad Sci U S A, 104*(47), 18549-18554.

Kam, Z., Minden, J. S., Agard, D. A., Sedat, J. W., & Leptin, M. (1991). Drosophila gastrulation: analysis of cell shape changes in living embryos by three-dimensional fluorescence microscopy. *Development, 112*(2), 365-370.

Kiehart, D., & Feghali, R. (1986). Cytoplasmic myosin from Drosophila melanogaster. *J Cell Biol, 103*, 1517-1525.

Kinoshita, N., Sasai, N., Misaki, K., & Yonemura, S. (2008). Apical accumulation of Rho in the neural plate is important for neural plate cell shape change and neural tube formation. *Mol Biol Cell, 19*(5), 2289-2299.

Knox, A., & Brown, N. (2002). Rap1 GTPase regulation of adherens junction positioning and cell adhesion. *Science, 295*(5558), 1285-1288.

Kölsch, V., Seher, T., Fernandez-Ballester, G. J., Serrano, L., & Leptin, M. (2007). Control of Drosophila gastrulation by apical localization of adherens junctions and RhoGEF2. *Science, 315*(5810), 384-386.

Kuiperij, H., De Rooij, J., Rehmann, H., van Triest, M., Wittinghofer, A., Bos, J., et al. (2003). Characterisation of PDZ-GEFs, a family of guanine nucleotide exchange factors specific for Rap1 and Rap2. *Biochim Biophys Acta, 1593*(2-3), 141-149.

Landsberg, K. P., Farhadifar, R., Ranft, J., Umetsu, D., Widmann, T. J., Bittig, T., et al. (2009). Increased cell bond tension governs cell sorting at the Drosophila anteroposterior compartment boundary. *Curr Biol, 19*(22), 1950-1955.

Le, T. L., Yap, A. S., & Stow, J. L. (1999). Recycling of E-cadherin: a potential mechanism for regulating cadherin dynamics. *J Cell Biol, 146*(1), 219-232.

Lee, J., Cho, K., Lee, J., Kim, D., Lee, S., Yoo, J., et al. (2002). Drosophila PDZ-GEF, a guanine nucleotide exchange factor for Rap1 GTPase, reveals a novel upstream regulatory mechanism in the mitogen-activated protein kinase signaling pathway. *Mol Cell Biol, 22*(21), 7658-7666.

Leptin, M. (1991). twist and snail as positive and negative regulators during Drosophila mesoderm development. *Genes Dev, 5*, 1568-1576.

Leptin, M. (1999). Gastrulation in Drosophila: the logic and the cellular mechanisms. *EMBO J, 18*(12), 3187-3192.

Leptin, M., & Grunewald, B. (1990). Cell shape changes during gastrulation in Drosophila. *Development, 110*(1), 73-84.

Levayer, R., Pelissier-Monier, A., & Lecuit, T. (2011). Spatial regulation of Dia and Myosin-II by RhoGEF2 controls initiation of E-cadherin endocytosis during epithelial morphogenesis. *Nat Cell Biol, 13*(5), 529-540.

Martin, A. C., Gelbart, M., Fernandez-Gonzalez, R., Kaschube, M., & Wieschaus, E. F. (2010). Integration of contractile forces during tissue invagination. *J Cell Biol, 188*(5), 735-749.

Martin, A. C., Kaschube, M., & Wieschaus, E. F. (2009). Pulsed contractions of an actin-myosin network drive apical constriction. *Nature, 457*(7228), 495-499.

McMahon, A., Reeves, G. T., Supatto, W., & Stathopoulos, A. (2010). Mesoderm migration in Drosophila is a multi-step process requiring FGF signaling and integrin activity. *Development, 137*(13), 2167-2175.

Mino, A., Ohtsuka, T., Inoue, E., & Takai, Y. (2000). Membrane-associated guanylate kinase with inverted orientation (MAGI)-1/brain angiogenesis inhibitor 1-associated protein (BAP1) as a scaffolding molecule for Rap small G protein GDP/GTP exchange protein at tight junctions. *Genes Cells, 5*(12), 1009-1016.

Morin, X., Daneman, R., Zavortink, M., & Chia, W. (2001). A protein trap strategy to detect GFP-tagged proteins expressed from their endogenous loci in Drosophila. *Proc Natl Acad Sci U S A, 98*(26), 15050-15055.

Morize, P., Christiansen, A. E., Costa, M., Parks, S., & Wieschaus, E. (1998). Hyperactivation of the *folded gastrulation* pathway induces specific cell shape changes. *Development, 125*(4), 589-597.

Müller, H. A., & Wieschaus, E. (1996). *armadillo*, *bazooka*, and *stardust* are critical for early stages in formation of the zonula adherens and maintenance of the polarized blastoderm epithelium in Drosophila. *J Cell Biol, 134*(1), 149-163.

Myster, S. H., Cavallo, R., Anderson, C. T., Fox, D. T., & Peifer, M. (2003). Drosophila p120catenin plays a supporting role in cell adhesion but is not an essential adherens junction component. *J Cell Biol, 160*(3), 433-449.

Nagai, T., & Honda, H. (2001). A dynamic cell model for the formation of epithelial tissues. *Philos Mag B, 81*(7), 699-719.

Nagai, T., & Honda, H. (2009). Computer simulation of wound closure in epithelial tissues: cell-basal-lamina adhesion. *Phys Rev E Stat Nonlin Soft Matter Phys, 80*(6 Pt 1), 061903.

Nikolaidou, K. K., & Barrett, K. (2004). A Rho GTPase signaling pathway is used reiteratively in epithelial folding and potentially selects the outcome of Rho activation. *Curr Biol, 14*(20), 1822-1826.

Oda, H., & Tsukita, S. (2001). Real-time imaging of cell-cell adherens junctions reveals that Drosophila mesoderm invagination begins with two phases of apical constriction of cells. *J Cell Sci, 114*(Pt 3), 493-501.

Oda, H., Tsukita, S., & Takeichi, M. (1998). Dynamic behavior of the cadherin-based cell-cell adhesion system during Drosophila gastrulation. *Dev Biol, 203*(2), 435-450.

Osterfield, M., Du, X., Schupbach, T., Wieschaus, E., & Shvartsman, S. Y. (2013). Three-dimensional epithelial morphogenesis in the developing Drosophila egg. *Dev Cell, 24*(4), 400-410.

Ott, A. (2010). The PDZ-GEF Dizzy regulates the establishment and maintenance of adherens junctions during early mesoderm formation in Drosophila. *Dissertation, Eberhard Karls Universität, Tübingen.*

Pacquelet, A., Lin, L., & Rorth, P. (2003). Binding site for p120/delta-catenin is not required for Drosophila E-cadherin function in vivo. *J Cell Biol, 160*(3), 313-319.

Parks, S., & Wieschaus, E. F. (1991). The *Drosophila* gastrulation gene *concertina* encodes a G α-like protein. *Cell, 64*(2), 447-458.

Pham, N., Cheglakov, I., Koch, C. A., de Hoog, C. L., Moran, M. F., & Rotin, D. (2000). The guanine nucleotide exchange factor CNrasGEF activates ras in response to cAMP and cGMP. *Curr Biol, 10*(9), 555-558.

Plageman, T. F., Jr., Chauhan, B. K., Yang, C., Jaudon, F., Shang, X., Zheng, Y., et al. (2011). A Trio-RhoA-Shroom3 pathway is required for apical constriction and epithelial invagination. *Development, 138*(23), 5177-5188.

Pouille, P. A., & Farge, E. (2008). Hydrodynamic simulation of multicellular embryo invagination. *Phys Biol, 5*(1), 015005.

Pouille, P. A., Ahmadi, P., Brunet, A. C., & Farge, E. (2009). Mechanical signals trigger Myosin II redistribution and mesoderm invagination in Drosophila embryos. *Sci Signal, 2*(66), ra16.

Ramain, P., Heitzler, P., Haenlin, M., & Simpson, P. (1993). *pannier*, a negative regulator of *achaete* and *scute* in Drosophila, encodes a zinc finger protein with homology to the vertebrate transcription factor GATA-1. *Development, 119*, 1277-1291.

Rand, M. D., Kearney, A. L., Dao, J., & Clason, T. (2010). Permeabilization of Drosophila embryos for introduction of small molecules. *Insect Biochem Mol Biol, 40*(11), 792-804.

Rauzi, M., Verant, P., Lecuit, T., & Lenne, P.-F. (2008). Nature and anisotropy of cortical forces orienting Drosophila tissue morphogenesis. *Nat Cell Biol, 10*(12), 1401-1410.

Reuter, R., & Leptin, M. (1994). Interacting functions of *snail*, *twist* and *huckebein* during the early development of germ layers in Drosophila. *Development, 120*, 1137-1150.

Rogers, S. L., Wiedemann, U., Hacker, U., Turck, C., & Vale, R. D. (2004). Drosophila RhoGEF2 associates with microtubule plus ends in an EB1-dependent manner. *Curr Biol, 14*(20), 1827-1833.

Roh-Johnson, M., Shemer, G., Higgins, C. D., McClellan, J. H., Werts, A. D., Tulu, U. S., et al. (2012). Triggering a Cell Shape Change by Exploiting Preexisting Actomyosin Contractions. *Science, 335*(6073), 1232-1235.

Roth, S., Stein, D., & Nüsslein-Volhard, C. (1989). A gradient of nuclear localization of the *dorsal* protein determines dorsoventral pattern in the Drosophila embryo. *Cell, 59*(6), 1189-1202.

Rumenapp, U., Blomquist, A., Schworer, G., Schablowski, H., Psoma, A., & Jakobs, K. H. (1999). Rho-specific binding and guanine nucleotide exchange catalysis by KIAA0380, a dbl family member. *FEBS Lett, 459*(3), 313-318.

Ryder, E., Ashburner, M., Bautista-Llacer, R., Drummond, J., Webster, J., Johnson, G., et al. (2007). The DrosDel Deletion Collection: A Drosophila Genomewide Chromosomal Deficiency Resource. *Genetics, 177*(1), 615-629.

Sawyer, J. K., Harris, N. J., Slep, K. C., Gaul, U., & Peifer, M. (2009). The Drosophila afadin homologue Canoe regulates linkage of the actin cytoskeleton to adherens junctions during apical constriction. *J Cell Biol, 186*(1), 57-73.

Schmidt, A., & Hall, A. (2002). Guanine nucleotide exchange factors for Rho GTPases: turning on the switch. *Genes Dev, 16*(13), 1587-1609.

Seher, T., Narasimha, M., Vogelsang, E., & Leptin, M. (2007). Analysis and reconstitution of the genetic cascade controlling early mesoderm morphogenesis in the Drosophila embryo. *Mech Devel, 124*(3), 167-179.

Seher, T. C., & Leptin, M. (2000). Tribbles, a cell-cycle brake that coordinates proliferation and morphogenesis during Drosophila gastrulation. *Curr Biol, 10*, 623-629.

Shirinian, M., Grabbe, C., Popovic, M., Varshney, G., Hugosson, F., Bos, H., et al. (2010). The Rap1 guanine nucleotide exchange factor C3G is required for preservation of larval muscle integrity in Drosophila melanogaster. *PLoS One, 5*(3), e9403.

Siekhaus, D., Haesemeyer, M., Moffitt, O., & Lehmann, R. (2010). RhoL controls invasion and Rap1 localization during immune cell transmigration in Drosophila. *Nat Cell Biol, 12*(6), 605-610.

Simpson, P. (1983). Maternal-zygotic gene interactions during formation of the dorsoventral pattern in Drosophila embryos. *Genetics, 105*, 615-632.

Solon, J., Kaya-Copur, A., Colombelli, J., & Brunner, D. (2009). Pulsed forces timed by a ratchet-like mechanism drive directed tissue movement during dorsal closure. *Cell, 137*(7), 1331-1342.

Spahn, P., Ott, A., & Reuter, R. (2012). The PDZ-GEF Dizzy regulates the establishment of adherens junctions required for ventral furrow formation in Drosophila. *J Cell Sci, 125*(16), 3801-3812.

Suzuki, M., Morita, H., & Ueno, N. (2012). Molecular mechanisms of cell shape changes that contribute to vertebrate neural tube closure. *Dev Growth Differ, 54*(3), 266-276.

Sweeton, D., Parks, S., Costa, M., & Wieschaus, E. (1991). Gastrulation in Drosophila: the formation of the ventral furrow and posterior midgut invaginations. *Development, 112*(3), 775-789.

Tautz, D., & Pfeifle, C. (1989). A non-radioactive in situ hybridization method for the localization of specific RNAs in Drosophila embryos reveals translational control of the segmentation gene hunchback. *Chromosoma, 98*, 81-85.

Tepass, U., Gruszynski-DeFeo, E., Haag, T. A., Omatyar, L., Torok, T., & Hartenstein, V. (1996). Shotgun encodes Drosophila E-cadherin and is preferentially required during cell rearrangement in the neurectoderm and other morphogenetically active epithelia. *Genes Dev, 10*, 672-685.

Tepass, U., Tanentzapf, G., Ward, R., & Fehon, R. G. (2001). Epithelial cell polarity and cell junctions in *Drosophila*. *Annu Rev Genet, 35*, 747-784.

Wang, F., & Hartenstein, V. (2006). Regulation of cell adhesion in the Drosophila embryo by phosphorylation of the Cadherin-Catenin-Complex. *Cell Tissue Res, 324*(1), 157-166.

Wang, H., Singh, S., Zheng, Z., Oh, S., Chen, X., Edwards, K., et al. (2006). Rap-GEF signaling controls stem cell anchoring to their niche through regulating DE-cadherin-mediated cell adhesion in the Drosophila testis. *Dev Cell, 10*(1), 117-126.

Wang, Y. C., Khan, Z., & Wieschaus, E. F. (2013). Distinct Rap1 Activity States Control the Extent of Epithelial Invagination via alpha-Catenin. *Dev Cell, 25*(3), 299-309.

Witzberger, M. M., Fitzpatrick, J. A., Crowley, J. C., & Minden, J. S. (2008). End-on imaging: a new perspective on dorsoventral development in Drosophila embryos. *Dev Dyn, 237*(11), 3252-3259.

Yamada, S., Pokutta, S., Drees, F., Weis, W. I., & Nelson, W. J. (2005). Deconstructing the cadherin-catenin-actin complex. *Cell, 123*(5), 889-901.

Young, P., Pesacreta, T., & Kiehart, D. (1991). Dynamic changes in the distribution of cytoplasmic myosin during Drosophila embryogenesis. *Development, 111*, 1-14.

11 AUTHOR CONTRIBUTIONS

Philipp Spahn

Apart from the exceptions specified below the work presented in this thesis was done by P.S. (project design, conduction of experiments, data analysis & interpretation, script programming and writing the manuscripts).

Alice Ott

Due to a cooperation on the project in section 6.1 a portion of the data shown in section 6.1 are contributions by A.O.: Fig. 2; Fig. 3A-F; Fig. 4; Fig. 5A,C,E-L (cross-sections); Fig. 7 A,C,E,G-I,K,M; Fig. 8A,C,D; Fig. 13; Fig. 17A, D-G; Video 1 (wt & dzy).

Rolf Reuter

R.R. outlined the major framework of the project in section 6.1 and contributed to design of the project in section 6.2. In addition, R.R. critically supervised the projects, discussed methods and results and commented on text and figures.

12 ACKNOWLEDGEMENTS

I would like to express my deep gratitude towards my boss, Rolf Reuter, for the support, lively discussions and intellectual stimulation during my time in his lab. I also want to express special thanks to Alexander Markowsky for assistance in physical modelling.

I would like to thank Anke Beermann for advice and support. I would like to thank Bernard Moussian for helpful and entertaining discussions about science, life, the universe and everything. I would like to thank Karin Henzler for her enduring cheerfulness. I would like to thank our technical staff, Ulrike Bochtler, Karin Flessner and Sabrina Thürmann for making life in the lab a lot easier. I would like to thank the current students in our lab (Anne-Marie Witz, Nadine Simon, Florian Hohnstein, Florian Heubach, Isabel Bayer, Yinwen Wang) for their interest in our projects and their vivid contribution to a healthy lab atmosphere.

In addition, I want to thank one of my academical teachers, Erich Weber, who I owe a lot of my scientific education, as well as my good friend Sören Alsheimer for allowing me to use the fantastic LSM 510 and for spending many after-work hours with me at the Irish Pub.

Several people have facilitated this thesis by sharing fly stocks, reagents or equipment with me which I highly appreciate. In particular, these are Maria Leptin, Elisabeth Knust, Michael Welte, Lisa Vogelsang, Martina Rembold, Adam Martin, Suzanne Eaton, Ruth Palmer, Uwe Irion, Andrew Renault, Thomas Lecuit, Jörg Grosshans, Marcos Gonzalez-Gaitan, Akira Nakamura, Dan Kiehart, Robert Cohen, Donald Ready, the Bloomington stock center and the microscopic facility at Max Planck Institute Tübingen.

Data and text in this work have been published in part in peer-reviewed journals and are reproduced with permission from the Company of Biologists and the Public Library of Science, respectively. In particular the articles are:

P. Spahn et al. (2012), J Cell Sci 125(16), 3801-12. doi: 10.1242/jcs.101196

P. Spahn & R. Reuter (2013), PLoS One, 8(9):e75051. doi: 10.1371/journal.pone.0075051

13 APPENDIX

MATLAB code of the computational model analyzed in section 6.2:

```
function VentralFurrow

% v 5.4a
% A VERTEX MODEL OF DROSOPHILA VENTRAL FURROW FORMATION
% ---------------------------------------------------

% ========================================================================
% Auxiliary Functions
    function trapez = Area(row,col,time)
        C = length(Cells{row,col,time});
        x = zeros(1,C); y = zeros(1,C);
        for s = 1:C
            sr = Cells{row,col,time}(1,s);
            sc = Cells{row,col,time}(2,s);
            x(s) = e_x(sr,sc,time);
            y(s) = e_y(sr,sc,time);
        end;
        smd = zeros(1,C);
        for s = 1:(C-1)
            smd(s) = (y(s)+y(s+1)) * (x(s)-x(s+1));
        end;
        smd(C) = (y(C)+y(1)) * (x(C)-x(1));
        trapez = 1/2*sum(smd);
    end

    function [a1x a1y] = Rot(a,cntr)
        a1 = [0 -1; 1 0]*(a'-cntr') + cntr';
        a1 = a1';
        a1x = a1(1); a1y = a1(2);
    end

    function [row col] = coord(a,dv)
        if mod(a,dv) == 0
            row = a/dv;
            col = dv;
        else
            row = floor(a/dv) + 1;
            col = mod(a,dv);
        end;
    end

    function [CellAreax_avg Gammax_avg Eccx_avg] =
             SmoothData(CellAreax,Gammax,Eccx,wsize)
        Nx = length(CellAreax(:,1,1));
        Mx = length(CellAreax(1,:,1));
        Tx = length(CellAreax(1,1,:));
        % Preallocation
        xmax = floor(Tx/2);
        xmin = -xmax;
        x = xmin:xmax;
```

```
        x = x(1:Tx);
        kernelx = 1/sqrt(2*pi*wsize^2) * exp(-x.^2/(2*wsize^2));
        Tx_avg = Tx - 4*wsize-4;
        CellAreax_avg = zeros(Nx,Mx,Tx_avg);
        Gammax_avg = zeros(Nx,Mx,Tx_avg);
        Eccx_avg = zeros(Nx,Mx,Tx_avg);
        % Smooth Data
        for ix = 1:Nx
            for jx = 1:Mx
                A = reshape(CellAreax(ix,jx,:),[1 Tx]);
                A0 = conv(kernelx,A,'same');
                CellAreax_avg(ix,jx,:) = A0((2*wsize+3):(end-2*wsize-2));
                G = reshape(Gammax(ix,jx,:),[1 Tx]);
                G0 = conv(kernelx,G,'same');
                Gammax_avg(ix,jx,:) = G0((2*wsize+3):(end-2*wsize-2));
                E = reshape(Eccx(ix,jx,:),[1 Tx]);
                E0 = conv(kernelx,E,'same');
                Eccx_avg(ix,jx,:) = E0((2*wsize+3):(end-2*wsize-2));
            end;
        end;
    end

    function [semimajor_axis, semiminor_axis, x0, y0, phix] =
            ellipse_fit(x, y)
        % (## documentation omitted, see .m File on CD ##)
        % Programmed by: Tal Hendel <thendel@tx.technion.ac.il>
        % Faculty of Biomedical Engineering, Technion- Israel Institute of
        % Technology
        % 12-Dec-2008
        %
        %-------------------------------------------------------------------
        x = x(:);
        y = y(:);
        %Construct Mx
        Mx = [2*x.*y y.^2 2*x 2*y ones(size(x))];
        % Multiply (-X.^2) by pseudoinverse(Mx)
        Ex = Mx\(-x.^2);
        %Extract parameters from vector Ex
        ax = 1;
        bx = Ex(1);
        cx = Ex(2);
        dx = Ex(3);
        fx = Ex(4);
        gx = Ex(5);
        %Use Formulas from Mathworld to find semimajor_axis,
        % semiminor_axis, x0, y0 and phix
        delta = bx^2-ax*cx;
        x0 = (cx*dx - bx*fx)/delta;
        y0 = (ax*fx - bx*dx)/delta;
        phix = 0.5 * acot((cx-ax)/(2*bx));
        nom = 2 * (ax*fx^2 + cx*dx^2 + gx*bx^2 - 2*bx*dx*fx - ax*cx*gx);
        sx = sqrt(1 + (4*bx^2)/(ax-cx)^2);
        a_prime = sqrt(nom/(delta* ( (cx-ax)*sx -(cx+ax))));
        b_prime = sqrt(nom/(delta* ( (ax-cx)*sx -(cx+ax))));
        semimajor_axis = max(a_prime, b_prime);
        semiminor_axis = min(a_prime, b_prime);
        if (a_prime < b_prime)
            phix = pi/2 - phix;
        end
    end
```

```
% ========================================================================

tic

disp('STARTING SIMULATION ....')

set(0,'DefaultFigureWindowStyle','docked')

% ------------------------------------------------------------------------
% MODEL PARAMETERS
% ------------------------------------------------------------------------
N = 13;                  % Sheet Height
M = 24;                  % Sheet Width
Z = (N+1)/2;             % Midline
deltaT = 0.01;           % Step Size
sigma = 1.75;            % Gradient Width (for Cut-Off set to Zero);
                         %  standard 1.75
thr = [Z-2 Z+2];         % Cut-Off Width
T0 = 200;                % Estimated Step Number
w = 0.33;                % Final Width of Furrow; standard 0.33
eta = 1;                 % (Viscosity; formal parameter, do not change)
eps = 0.1;               % Swap Threshold for T1 transitions
Gmax = 25;               % Maximum Contractility (linear term)
shf = 0.0;               % Initial Vertex Position Randomizer
                         %  (0.0 = no randomization)
Mrg = 2;                 % Non-contractile Margin
Lambda_M = 6.0;          % Lambda at Furrow Margin

% Define Area Elasticity
K = 2.5;

% Define Contractility
G00 = 0.0;               % Linear Offset; standard 0.0
G01 = 0.15;              % Linear Slope; standard 0.15
G02 = 0.3;               % Brownian Noise; standard 0.3

% Define Line Tension
Lambda = 0.2;            % standard 0.2

% Define  Line Elasticity
Kappa = 0.15;            % standard 0.15

% Special Cases
tear = 0;                % Simulation of tear in epithelium (not used)
twi = 0;                 % Simulation of twi phenotype
relax = 0;               % Simulation of relaxation after loss of
                         %  contractility
tfix = 0;                % Simulation with fixed number of time-steps
colcode = 0;             % Simulation with contractility coded by colour

% Smoothing
windowsize = 2;          % Windowsize for smoothing measurement data

% Proximity Alert
proxy = 'on';            % Enable T1 transitions

% Define Colormap
if colcode == 1
```

```
    load('VFF_colormap','mymap3');
    colmap = flipud(mymap3);
end;

% ------------------------------------------------------------------------
% PREALLOCATION
% ------------------------------------------------------------------------

% Estimated Simulation Time
T = 0.01/deltaT * T0;

% Preferred Area and Preferred Edge Length
A0 = 2.5981;
L0 = 1;

e_x(:,:,T) = zeros(N+1,2*M+2);
e_y(:,:,T) = zeros(N+1,2*M+2);
CellArea = A0*ones(N,M,T);
delE1x = zeros(N+1,2*M+2);
delE1y = zeros(N+1,2*M+2);
delE2x = zeros(N+1,2*M+2);
delE2y = zeros(N+1,2*M+2);
delE3x = zeros(N+1,2*M+2);
delE3y = zeros(N+1,2*M+2);
delE4x = zeros(N+1,2*M+2);
delE4y = zeros(N+1,2*M+2);
E1_Mat = zeros(N,M,T);
E3_Mat = zeros(N,M,T);
E4_Mat = zeros(N,M,T);
E = zeros(1,T);
Gamma(:,:,T) = zeros(N,M);
Cells{N,M,T} = zeros(2,6);
Ngbs = zeros((N+1)*(2*M+2),(N+1)*(2*M+2),T);
Ngb_t = zeros((N+1)*(2*M+2),3);
AdjCells = zeros((N+1)*(2*M+2),N*M,T);
AdjC_t = zeros((N+1)*(2*M+2),3);

% ------------------------------------------------------------------------
% CREATE SIMULATION ID
% ------------------------------------------------------------------------
rng shuffle
SimID = floor(10000*rand);
SimID = uint32(SimID);
ID_text = int2str(SimID);
foldername = strcat('ID#',ID_text);
mkdir(foldername);
cd(foldername);

mkdir('Frames');
cd('Frames');

% ---------------------------------------------------------
% CELL SHEET
% ---------------------------------------------------------

% Randomizer
shf_r = shf * rand(N+1,2*M+2);
shf_r(1,:) = 0; shf_r(N+1,:) = 0;
```

```
shf_r(:,1:2) = 0; shf_r(:,(2*M+1):end) = 0;
shf_phi = 2*pi * rand(N+1,2*M+2);
shf_x = shf_r .* cos(shf_phi);
shf_y = shf_r .* sin(shf_phi);

% Define Vertices
for i = 1:2:N           % i odd
    for j = 1:2:(2*M+1)     % j odd
        e_x(i,j,1) = floor(j/2)*sqrt(3) + shf_x(i,j);
        e_y(i,j,1) = 1/2+floor(i/2)*3 + shf_y(i,j);
    end;
    for j = 2:2:(2*M+2)     % j even
        e_x(i,j,1) = sqrt(3)/2+floor((j-1)/2)*sqrt(3) + shf_x(i,j);
        e_y(i,j,1) = floor(i/2)*3 + shf_y(i,j);
    end;
end;
for i = 2:2:(N+1)       % i even
    for j = 1:2:(2*M+1)     % j odd
        e_x(i,j,1) = floor(j/2)*sqrt(3) + shf_x(i,j);
        e_y(i,j,1) = 3/2+floor((i-1)/2)*3 + shf_y(i,j);
    end;
    for j = 2:2:(2*M+2)     % j even
        e_x(i,j,1) = sqrt(3)/2+floor((j-1)/2)*sqrt(3) + shf_x(i,j);
        e_y(i,j,1) = 2+floor((i-1)/2)*3 + shf_y(i,j);
    end;
end;

% Define Cells
for t = 1:T
    for j = 1:M
        for i = 1:2:N       % i odd
            Cells{i,j,t} = [i+1 i+1 i i i i+1;
                            2*j 2*j+1 2*j+1 2*j 2*j-1 2*j-1];
        end;
        for i = 2:2:(N-1)   % i even
            Cells{i,j,t} = [i+1 i+1 i i i i+1;
                            2*j+1 2*j+2 2*j+2 2*j+1 2*j 2*j];
        end;
    end;
end;

% Plot Cell Sheet
figure;
hold on;
axis equal;
x_min = 0;
y_min = 0;
x_max = M*sqrt(3)+sqrt(3)/2;
y_max = 2+floor(N/2)*3;
axis([x_min-1 x_max y_min-1 y_max]);
axis off;
for i = 1:N
    for j = 1:M
        rows = Cells{i,j,1}(1,:); cols = Cells{i,j,1}(2,:);
        vertices_x = diag(e_x(rows,cols,1))';
        vertices_y = diag(e_y(rows,cols,1))';
        fill(vertices_x,vertices_y,[1 1 1]);
    end;
end;
```

```
image_title = strcat('ID#',ID_text,'-t001');
title(image_title);
filename = strcat(image_title,'.png');
saveas(gcf,filename,'png');


% Define Neighbour Vertices and Adjacent Cells
for i = 3:2:N           % i odd
    for j = 3:2:(2*M+1)       % j odd
        R = (i-1)*(2*M+2)+j;
        N1 = (i-1)*(2*M+2)+j+1;
        N2 = i*(2*M+2)+j;
        N3 = (i-1)*(2*M+2)+j-1;
        Ngbs(R,N1,:) = 1; Ngbs(R,N2,:) = 2; Ngbs(R,N3,:) = 3;
        C1 = (i-1)*M + (j-1)/2;
        C2 = (i-2)*M + (j-1)/2;
        C3 = (i-1)*M + (j+1)/2;
        AdjCells(R,C1,:) = 1; AdjCells(R,C2,:) = 2; AdjCells(R,C3,:) = 3;
    end;
    for j = 2:2:(2*M)         % j even
        R = (i-1)*(2*M+2)+j;
        N1 = (i-1)*(2*M+2)+j-1;
        N2 = (i-2)*(2*M+2)+j;
        N3 = (i-1)*(2*M+2)+j+1;
        Ngbs(R,N1,:) = 1; Ngbs(R,N2,:) = 2; Ngbs(R,N3,:) = 3;
        C1 = (i-2)*M + j/2;
        C2 = (i-1)*M + j/2;
        C3 = (i-2)*M + (j-2)/2;
        AdjCells(R,C1,:) = 1; AdjCells(R,C2,:) = 2; AdjCells(R,C3,:) = 3;
    end;
end;
for i = 2:2:(N-1)         % i even
    for j = 3:2:(2*M+1)       % j odd
        R = (i-1)*(2*M+2)+j;
        N1 = (i-1)*(2*M+2)+j-1;
        N2 = (i-2)*(2*M+2)+j;
        N3 = (i-1)*(2*M+2)+j+1;
        Ngbs(R,N1,:) = 1; Ngbs(R,N2,:) = 2; Ngbs(R,N3,:) = 3;
        C1 = (i-2)*M + (j+1)/2;
        C2 = (i-1)*M + (j-1)/2;
        C3 = (i-2)*M + (j-1)/2;
        AdjCells(R,C1,:) = 1; AdjCells(R,C2,:) = 2; AdjCells(R,C3,:) = 3;
    end;
    for j = 2:2:(2*M)         % j even
        R = (i-1)*(2*M+2)+j;
        N1 = (i-1)*(2*M+2)+j+1;
        N2 = i*(2*M+2)+j;
        N3 = (i-1)*(2*M+2)+j-1;
        Ngbs(R,N1,:) = 1; Ngbs(R,N2,:) = 2; Ngbs(R,N3,:) = 3;
        C1 = (i-1)*M + (j-2)/2;
        C2 = (i-2)*M + j/2;
        C3 = (i-1)*M + j/2;
        AdjCells(R,C1,:) = 1; AdjCells(R,C2,:) = 2; AdjCells(R,C3,:) = 3;
    end;
end;
```

```
% --------------------------------
% CONTRACTILITY DRIVER
% --------------------------------

% Linear Component
g00 = G00;                  % Linear Offset
g01 = T0/T * G01;           % Linear Slope
% Brownian Component
g2 = T0/T * G02;


% Linear Component
LIN = g00*ones(N*M,T) + min(Gmax,g01*repmat(1:T,N*M,1));

% Brownian Component
Q = randn(T,N*M);
BROWN = g2 * cumsum(Q)';

G = abs(LIN + BROWN);


% --------------------------------
% CUTOFF / GRADIENT
% --------------------------------

if sigma == 0               % CUTOFF
    for i = 1:(thr(1)-1)
        for j = 1:M
            Gamma(i,j,:) = zeros(1,T);
        end;
    end;
    for i = thr(1):thr(2)
        for j = 2:(M-1)
            Gamma(i,j,:) = G((i-1)*N+j,:);
        end;
    end;
    for i = (thr(2)+1):N
        for j = 1:M
            Gamma(i,j,:) = zeros(1,T);
        end;
    end;
else                        % GRADIENT
    for i = 1:N
        for j = 1:M
            Gamma(i,j,:) = exp(-(i-Z)^2/(2*sigma^2))*G((i-1)*M+j,:);
        end;
    end;
end;

GammaMax = max(Gamma(:));

% --------------------------------
% NON-CONTRACTILE MARGIN
% --------------------------------

Gamma(:,1:Mrg,:) = 0 ;
Gamma(:,(M-Mrg+1):M,:) = 0 ;
```

```
% ---------------------------------
% SPECIAL SIMULATIONS
% ---------------------------------

if tear == 1
    Gamma((Z-2):(Z+2),M/2:(M/2+1),100:T) = 0;
end;

if twi == 1
    RM = 0.5*rand(N,M);
    Random = repmat(RM,[1 1 T]);
    Gamma = Random .* Gamma;
end;

if relax == 1
    Gamma(:,:,100:T) = 0;
end;

if tfix == 1
    w = 0;
end;

% ---------------------------------

% Furrow Width
U0 = mean2(CellArea((Z-2):(Z+2),(Mrg+2):(M-Mrg-2),1));
U = U0;


% ---------------------------------
% MAIN PROCEDURE
% ---------------------------------

t = 1;

while (U > w*U0 && t < T)

    % Cell Areas
    for i = 1:N
        for j = 1:M
            CellArea(i,j,t) = abs(Area(i,j,t));
        end;
    end;

    % ---------------------------------
    % ENERGY
    % ---------------------------------

    % Area Elasticity
    for i = 1:N
        for j = 1:M
            E1_Mat(i,j,t) = K/2 * (CellArea(i,j,t) - A0)^2;
        end;
    end;
    E1 = sum(sum(E1_Mat(:,:,t)));
```

```
% Line Tension
E2 = 0;
for i = 1:(N+1)
    for j = 1:(2*M+2)
        ngbs = find(Ngbs((i-1)*(2*M+2)+j,:,t));
        R_ngbs = ngbs(ngbs>(i-1)*(2*M+2)+j);
        for r = 1:length(R_ngbs)
            [ir is] = coord(R_ngbs(r),2*M+2);
            L = norm([e_x(i,j,t)-e_x(ir,is,t)
                    e_y(i,j,t)-e_y(ir,is,t)]);
            if (j < 2*Mrg+4 || j > 2*M+2-2*Mrg-4)
                E2 = E2 + Lambda_M*L;
            else
                E2 = E2 + Lambda*L;
            end;
        end;
    end;
end;

% Contractility
for i = 1:N
    for j = 1:M
        E3_Mat(i,j,t) = Gamma(i,j,t)/2 * CellArea(i,j,t)^2;
    end;
end;
E3 = sum(sum(E3_Mat(:,:,t)));


% Cortical Line Elasticity
for i = 1:N
    for j = 1:M
        r = Cells{i,j,t}(1,:);
        s = Cells{i,j,t}(2,:);
        for k = 1:(length(r)-1)
            e1 = [e_x(r(k),s(k),t) e_y(r(k),s(k),t)];
            e2 = [e_x(r(k+1),s(k+1),t) e_y(r(k+1),s(k+1),t)];
            L = norm(e1 - e2);
            E4_Mat(i,j,t) = E4_Mat(i,j,t) + Kappa/2*(L - L0)^2;
        end;
        e1 = [e_x(r(end),s(end),t) e_y(r(end),s(end),t)];
        e2 = [e_x(r(1),s(1),t) e_y(r(1),s(1),t)];
        L = norm(e1 - e2);
        E4_Mat(i,j,t) = E4_Mat(i,j,t) + Kappa/2*(L - L0)^2;
    end;
end;
E4 = sum(sum(E4_Mat(:,:,t)));


% Total
E(t) = E1 + E2 + E3 + E4;

% ---------------------------------------------------------


% ----------------------------------------
% ENERGY DERIVATIVE
% ----------------------------------------
```

```
    for i = 2:N
        for j = 3:(2*M)
            % Identify Adjacent Cells and Neighbours
            R = (i-1)*(2*M+2) + j;
            AdjC_t(R,1) = find(AdjCells(R,:,t) == 1);
            AdjC_t(R,2) = find(AdjCells(R,:,t) == 2);
            AdjC_t(R,3) = find(AdjCells(R,:,t) == 3);
            Ngb_t(R,1) = find(Ngbs(R,:,t) == 1);
            Ngb_t(R,2) = find(Ngbs(R,:,t) == 2);
            Ngb_t(R,3) = find(Ngbs(R,:,t) == 3);
            % Get row/col coordinates
            [C1r C1c] = coord(AdjC_t(R,1),M);
            [C2r C2c] = coord(AdjC_t(R,2),M);
            [C3r C3c] = coord(AdjC_t(R,3),M);
            [N1r N1c] = coord(Ngb_t(R,1),2*M+2);
            [N2r N2c] = coord(Ngb_t(R,2),2*M+2);
            [N3r N3c] = coord(Ngb_t(R,3),2*M+2);

            % ..............................................
            % Area Elasticity Derivative (E1)
            % ..............................................
            delE1x_1 = K * (CellArea(C1r,C1c,t)-A0) * sign(Area(C1r,C1c,t))
                         * (e_y(N3r,N3c,t)/2 - e_y(N2r,N2c,t)/2);
            delE1y_1 = K * (CellArea(C1r,C1c,t)-A0) * sign(Area(C1r,C1c,t))
                         * (e_x(N2r,N2c,t)/2 - e_x(N3r,N3c,t)/2);
            delE1x_2 = K * (CellArea(C2r,C2c,t)-A0) * sign(Area(C2r,C2c,t))
                         * (e_y(N1r,N1c,t)/2 - e_y(N3r,N3c,t)/2);
            delE1y_2 = K * (CellArea(C2r,C2c,t)-A0) * sign(Area(C2r,C2c,t))
                         * (e_x(N3r,N3c,t)/2 - e_x(N1r,N1c,t)/2);
            delE1x_3 = K * (CellArea(C3r,C3c,t)-A0) * sign(Area(C3r,C3c,t))
                         * (e_y(N2r,N2c,t)/2 - e_y(N1r,N1c,t)/2);
            delE1y_3 = K * (CellArea(C3r,C3c,t)-A0) * sign(Area(C3r,C3c,t))
                         * (e_x(N1r,N1c,t)/2 - e_x(N2r,N2c,t)/2);
            delE1x(i,j) = delE1x_1 + delE1x_2 + delE1x_3;
            delE1y(i,j) = delE1y_1 + delE1y_2 + delE1y_3;

            % ..............................................
            % Line Tension Derivative (E2)
            % ..............................................
            % R - N1 ---------------------------------------
            if (j < 2*Mrg+4 || j > 2*M+2-2*Mrg-4)
                lambda = Lambda_M;
            else
                lambda = Lambda;
            end;
            L = norm([e_x(i,j,t)-e_x(N1r,N1c,t)
                  e_y(i,j,t)-e_y(N1r,N1c,t)]);
            delE2x_1 = lambda * (e_x(i,j,t) - e_x(N1r,N1c,t)) / L;
            delE2y_1 = lambda * (e_y(i,j,t) - e_y(N1r,N1c,t)) / L;
            % R - N2 ---------------------------------------
            L = norm([e_x(i,j,t)-e_x(N2r,N2c,t)
                  e_y(i,j,t)-e_y(N2r,N2c,t)]);
            delE2x_2 = lambda * (e_x(i,j,t) - e_x(N2r,N2c,t)) / L;
            delE2y_2 = lambda * (e_y(i,j,t) - e_y(N2r,N2c,t)) / L;
            % R - N3 ---------------------------------------
            L = norm([e_x(i,j,t)-e_x(N3r,N3c,t)
                  e_y(i,j,t)-e_y(N3r,N3c,t)]);
            delE2x_3 = lambda * (e_x(i,j,t) - e_x(N3r,N3c,t)) / L;
            delE2y_3 = lambda * (e_y(i,j,t) - e_y(N3r,N3c,t)) / L;
            % total ----------------------------------------
```

```
delE2x(i,j) = delE2x_1 + delE2x_2 + delE2x_3;
delE2y(i,j) = delE2y_1 + delE2y_2 + delE2y_3;

% ..............................................
% Contractility Derivative (E3)
% ..............................................
delE3x_1 = Gamma(C1r,C1c,t) * CellArea(C1r,C1c,t) *
 sign(Area(C1r,C1c,t)) * (e_y(N3r,N3c,t)/2 - e_y(N2r,N2c,t)/2);

delE3y_1 = Gamma(C1r,C1c,t) * CellArea(C1r,C1c,t) *
 sign(Area(C1r,C1c,t)) * (e_x(N2r,N2c,t)/2 - e_x(N3r,N3c,t)/2);

delE3x_2 = Gamma(C2r,C2c,t) * CellArea(C2r,C2c,t) *
 sign(Area(C2r,C2c,t)) * (e_y(N1r,N1c,t)/2 - e_y(N3r,N3c,t)/2);

delE3y_2 = Gamma(C2r,C2c,t) * CellArea(C2r,C2c,t) *
 sign(Area(C2r,C2c,t)) * (e_x(N3r,N3c,t)/2 - e_x(N1r,N1c,t)/2);

delE3x_3 = Gamma(C3r,C3c,t) * CellArea(C3r,C3c,t) *
 sign(Area(C3r,C3c,t)) * (e_y(N2r,N2c,t)/2 - e_y(N1r,N1c,t)/2);

delE3y_3 = Gamma(C3r,C3c,t) * CellArea(C3r,C3c,t) *
 sign(Area(C3r,C3c,t)) * (e_x(N1r,N1c,t)/2 - e_x(N2r,N2c,t)/2);

delE3x(i,j) = delE3x_1 + delE3x_2 + delE3x_3;

delE3y(i,j) = delE3y_1 + delE3y_2 + delE3y_3;

% ..............................................
% Cortical Line Elasticity Derivative (E4)
% ..............................................
L1 = norm([e_x(i,j,t)-e_x(N1r,N1c,t)
      e_y(i,j,t)-e_y(N1r,N1c,t)]);
L2 = norm([e_x(i,j,t)-e_x(N2r,N2c,t)
      e_y(i,j,t)-e_y(N2r,N2c,t)]);
L3 = norm([e_x(i,j,t)-e_x(N3r,N3c,t)
      e_y(i,j,t)-e_y(N3r,N3c,t)]);
% C1
delE4x_1 = Kappa*(L2-L0)*(e_x(i,j,t)-e_x(N2r,N2c,t))/L2 +
      Kappa*(L3-L0)*(e_x(i,j,t)-e_x(N3r,N3c,t))/L3;

delE4y_1 = Kappa*(L2-L0)*(e_y(i,j,t)-e_y(N2r,N2c,t))/L2 +
      Kappa*(L3-L0)*(e_y(i,j,t)-e_y(N3r,N3c,t))/L3;
% C2
delE4x_2 = Kappa*(L1-L0)*(e_x(i,j,t)-e_x(N1r,N1c,t))/L1 +
      Kappa*(L3-L0)*(e_x(i,j,t)-e_x(N3r,N3c,t))/L3;

delE4y_2 = Kappa*(L1-L0)*(e_y(i,j,t)-e_y(N1r,N1c,t))/L1 +
      Kappa*(L3-L0)*(e_y(i,j,t)-e_y(N3r,N3c,t))/L3;
% C3
delE4x_3 = Kappa*(L1-L0)*(e_x(i,j,t)-e_x(N1r,N1c,t))/L1 +
      Kappa*(L2-L0)*(e_x(i,j,t)-e_x(N2r,N2c,t))/L2;

delE4y_3 = Kappa*(L1-L0)*(e_y(i,j,t)-e_y(N1r,N1c,t))/L1 +
      Kappa*(L2-L0)*(e_y(i,j,t)-e_y(N2r,N2c,t))/L2;
% total
delE4x(i,j) = delE4x_1 + delE4x_2 + delE4x_3;
delE4y(i,j) = delE4y_1 + delE4y_2 + delE4y_3;
```

```
    end;
end;

% ---------------------------------------------------------

% -------------------------------------------------
% NEW COORDINATES
% -------------------------------------------------

delEx = delE1x + delE2x + delE3x + delE4x;
delEy = delE1y + delE2y + delE3y + delE4y;
e_x(2:N,3:(2*M),t+1)
        = e_x(2:N,3:(2*M),t) - deltaT * 1/eta * delEx(2:N,3:(2*M));
e_y(2:N,3:(2*M),t+1)
        = e_y(2:N,3:(2*M),t) - deltaT * 1/eta * delEy(2:N,3:(2*M));

% Fixed vertices
e_x(1,:,t+1) = e_x(1,:,t); e_y(1,:,t+1) = e_y(1,:,t);
e_x(N+1,:,t+1) = e_x(N+1,:,t); e_y(N+1,:,t+1) = e_y(N+1,:,t);
e_x(:,1:2,t+1) = e_x(:,1:2,t); e_y(:,1:2,t+1) = e_y(:,1:2,t);
e_x(:,(2*M+1):end,t+1) = e_x(:,(2*M+1):end,t);
e_y(:,(2*M+1):end,t+1) = e_y(:,(2*M+1):end,t);


% -------------------------------------------------
% PROXIMITY ALERT AND SWAPPING
% -------------------------------------------------

if strcmp(proxy,'on')
    % Calculate Distance between 2-Neighbours
    N2dist = zeros((N+1)*(2*M+2),(N+1)*(2*M+2));
    for i = 2:N
        for j = 4:(2*M-1)
            R = (i-1)*(2*M+2)+j;
            [N2r N2c] = coord(Ngb_t(R,2),2*M+2);
            N2dist(R,Ngb_t(R,2)) = norm([e_x(i,j,t+1)-e_x(N2r,N2c,t+1)
                                         e_y(i,j,t+1)-e_y(N2r,N2c,t+1)]);
        end;
    end;
    N2Dist = triu(N2dist);
    % Identify Proximity Alerts
    [S1 S2] = find(N2Dist < eps & N2Dist > 0);   % always S1(i) < S2(i)
    for i = 1:length(S1)
        % Identify Coordinates of Neighbours and Adjacent Cells
        % Involved in Swap
        [S1r S1c] = coord(S1(i),2*M+2);
        [S2r S2c] = coord(S2(i),2*M+2);
        S1N2 = Ngb_t(S1(i),2); S1N3 = Ngb_t(S1(i),3);
        S2N2 = Ngb_t(S2(i),2); S2N3 = Ngb_t(S2(i),3);
        S1C1 = AdjC_t(S1(i),1); S1C2 = AdjC_t(S1(i),2);
        S2C1 = AdjC_t(S2(i),1); S2C2 = AdjC_t(S2(i),2);
        [S1C1r S1C1c] = coord(S1C1,M);
        [S1C2r S1C2c] = coord(S1C2,M);
        [S2C1r S2C1c] = coord(S2C1,M);
        [S2C2r S2C2c] = coord(S2C2,M);
        [S2N3r S2N3c] = coord(S2N3,2*M+2);
        S1N1 = Ngb_t(S1(i),1);
        [S1N1r S1N1c] = coord(S1N1,2*M+2);
        S2N1 = Ngb_t(S2(i),1);
```

```
[S2N1r S2N1c] = coord(S2N1,2*M+2);

% STEP 1: Swap Vertices (90° rotation)
RC = 1/2 * ([e_x(S1r,S1c,t+1) e_y(S1r,S1c,t+1)] +
       [e_x(S2r,S2c,t+1) e_y(S2r,S2c,t+1)]);
vec1 = [e_x(S1r,S1c,t+1) e_y(S1r,S1c,t+1)];
vec2 = [e_x(S2r,S2c,t+1) e_y(S2r,S2c,t+1)];
[e_x(S1r,S1c,t+1) e_y(S1r,S1c,t+1)] = Rot(vec1,RC);
[e_x(S2r,S2c,t+1) e_y(S2r,S2c,t+1)] = Rot(vec2,RC);
% STEP 2: Change Neighbour Vertices
    % 2a
Ngbs(S1(i),S1N3,t:T) = 0;
Ngbs(S1(i),S2(i),t:T) = 3;
Ngbs(S1(i),S2N3,t:T) = 2;
Ngbs(S2(i),S2N3,t:T) = 0;
Ngbs(S2(i),S1(i),t:T) = 3;
Ngbs(S2(i),S1N3,t:T) = 2;
u = Ngbs(S1N3,S1(i),t);
Ngbs(S1N3,S1(i),t:T) = 0;
Ngbs(S1N3,S2(i),t:T) = u;
v = Ngbs(S2N3,S2(i),t);
Ngbs(S2N3,S2(i),t:T) = 0;
Ngbs(S2N3,S1(i),t:T) = v;
    % 2b
Ngb_t(S1(i),2) = S2N3; Ngb_t(S1(i),3) = S2(i);
Ngb_t(S2(i),2) = S1N3; Ngb_t(S2(i),3) = S1(i);
Ngb_t(S1N3,u) = S2(i); Ngb_t(S2N3,v) = S1(i);
% STEP 3: Change Adjacent Cells
    % 3a
AdjCells(S1(i),S1C1,t:T) = 0;
AdjCells(S1(i),S2C2,t:T) = 1;
AdjCells(S2(i),S2C1,t:T) = 0;
AdjCells(S2(i),S1C2,t:T) = 1;
    % 3b
AdjC_t(S1(i),1) = S2C2;
AdjC_t(S2(i),1) = S1C2;
% STEP 4: Change Cells
    % S1C1
S1C1rows = Cells{S1C1r,S1C1c,t}(1,:);
S1C1cols = Cells{S1C1r,S1C1c,t}(2,:);
pos = findstr([S2N1r S2r S1r],S1C1rows);
S1C1rows = [S1C1rows(1:(pos+1)) S1C1rows((pos+3):end)];
S1C1cols = [S1C1cols(1:(pos+1)) S1C1cols((pos+3):end)];
    % S1C2
S1C2rows = Cells{S1C2r,S1C2c,t}(1,:);
S1C2cols = Cells{S1C2r,S1C2c,t}(2,:);
S1C2rows(end+1) = S2r; S1C2cols(end+1) = S2c;
    % S2C1
S2C1rows = Cells{S2C1r,S2C1c,t}(1,:);
S2C1cols = Cells{S2C1r,S2C1c,t}(2,:);
pos = findstr([S1N1r S1r S2r],S2C1rows);
S2C1rows = [S2C1rows(1:(pos+1)) S2C1rows((pos+3):end)];
S2C1cols = [S2C1cols(1:(pos+1)) S2C1cols((pos+3):end)];
    % S2C2
S2C2rows = Cells{S2C2r,S2C2c,t}(1,:);
S2C2cols = Cells{S2C2r,S2C2c,t}(2,:);
pos = findstr([S2N3r S2r S2N1r],S2C2rows);
S2C2rows = [S2C2rows(1:pos) S1r S2C2rows((pos+1):end)];
S2C2cols = [S2C2cols(1:pos) S1c S2C2cols((pos+1):end)];
for time = t:T
```

```
                Cells{S1C1r,S1C1c,time} = [S1C1rows; S1C1cols];
                Cells{S1C2r,S1C2c,time} = [S1C2rows; S1C2cols];
                Cells{S2C1r,S2C1c,time} = [S2C1rows; S2C1cols];
                Cells{S2C2r,S2C2c,time} = [S2C2rows; S2C2cols];
            end;
        end;
    end;
    % ---------------------------------------------------------

    t = t+1;

    % Plot Cell Sheet
    clf;
    hold on;
    axis equal;
    x_min = 0;
    y_min = 0;
    x_max = M*sqrt(3)+sqrt(3)/2;
    y_max = 2+floor(N/2)*3;
    axis([x_min-1 x_max y_min-1 y_max]);
    axis off;
    for i = 1:N
        for j = 1:M
            rows = Cells{i,j,t}(1,:); cols = Cells{i,j,t}(2,:);
            vertices_x = diag(e_x(rows,cols,t))';
            vertices_y = diag(e_y(rows,cols,t))';
            if colcode == 1
                q = min(length(colmap),round(Gamma(i,j,t)/GammaMax *
                   length(colmap))+1);
                fill(vertices_x,vertices_y,[colmap(q,1) colmap(q,2)
                   colmap(q,3)]);
            else
                fill(vertices_x,vertices_y,[1 1 1]);
            end;
        end;
    end;

    % Save Image
    if t <= 9
        image_title = strcat('ID#',ID_text,'-t00',int2str(t));
    elseif t <= 99
        image_title = strcat('ID#',ID_text,'-t0',int2str(t));
    else image_title = strcat('ID#',ID_text,'-t',int2str(t));
    end;
    title(image_title);
    filename = strcat(image_title,'.png');
    saveas(gcf,filename,'png');

    % Furrow Width
    U = mean2(CellArea((Z-2):(Z+2),(Mrg+2):(M-Mrg-2),t-1));

    % Display Progress
    disp(['Energy: ',num2str(E(t-1)),' || ','Furrow Width [%]:
      ',num2str(U/U0*100)]);

end;

% ---------------------------------------------------------------------
```

```
% ------------------------------------------------
% ASSEMBLE RESULTS
% ------------------------------------------------
T = t-1;
E = E(1:T);
Gamma = Gamma(:,:,1:T);
e_x = e_x(:,:,1:T);
e_y = e_y(:,:,1:T);
CellArea = CellArea(:,:,1:T);
% Calculate Eccentricity
Eccentricity = zeros(N,M,T);
for i = 1:N
    for j = 1:M
        for t = 1:T
            rows = Cells{i,j,t}(1,:); cols = Cells{i,j,t}(2,:);
            vx = diag(e_x(rows,cols,t))';
            vy = diag(e_y(rows,cols,t))';
            [a,b,~,~,theta] = ellipse_fit(vx,vy);
            theta = min(theta,pi/2-theta)/2;
            a0 = sqrt(1/(cos(theta)^2/a^2 + sin(theta)^2/b^2));
            b0 = sqrt(1/(sin(theta)^2/a^2 + cos(theta)^2/b^2));
            Eccentricity(i,j,t) = a0/b0;
        end;
    end;
end;
% Smooth Data
[CellArea_avg Gamma_avg Ecc_avg] =
SmoothData(CellArea,Gamma,Eccentricity,windowsize);
T_avg = length(CellArea_avg(1,1,:));
% Calculate Rates
GammaRate = zeros(N,M,T-1);
ConstrictionRate = zeros(N,M,T-1);
GammaRate_avg = zeros(N,M,T_avg-1);
ConstrictionRate_avg = zeros(N,M,T_avg-1);
for t = 1:(T-1)
    GammaRate(:,:,t) = Gamma(:,:,t+1) - Gamma(:,:,t);
    ConstrictionRate(:,:,t) = -(CellArea(:,:,t+1) - CellArea(:,:,t));
end;
for t = 1:(T_avg-1)
    GammaRate_avg(:,:,t) = Gamma_avg(:,:,t+1) - Gamma_avg(:,:,t);
    ConstrictionRate_avg(:,:,t) = -(CellArea_avg(:,:,t+1) -
CellArea_avg(:,:,t));
end;


cd ..

% ------------------------------------------------
% SAVE RESULTS AND PARAMETERS
% ------------------------------------------------

save all_parameters.mat

paramtxt = fopen('Parameters.txt','w');
fprintf(paramtxt,['Sheet Height: ' int2str(N)]);
fprintf(paramtxt,'\n');
fprintf(paramtxt,['Sheet Width: ' int2str(M)]);
```

```
fprintf(paramtxt,'\n');
fprintf(paramtxt,['Area Elasticity: ' num2str(K)]);
fprintf(paramtxt,'\n');
fprintf(paramtxt,['Contractility (linear offset): ' num2str(G00)]);
fprintf(paramtxt,'\n');
fprintf(paramtxt,['Contractility (linear slope): ' num2str(G01)]);
fprintf(paramtxt,'\n');
fprintf(paramtxt,['Contractility (noise): ' num2str(G02)]);
fprintf(paramtxt,'\n');
fprintf(paramtxt,['Line Tension: ' num2str(Lambda)]);
fprintf(paramtxt,'\n');
fprintf(paramtxt,['Line Elasticity: ' num2str(Kappa)]);
fprintf(paramtxt,'\n');
fprintf(paramtxt,['Gradient Width: ' num2str(sigma)]);
fprintf(paramtxt,'\n');
fprintf(paramtxt,['Delta T: ' num2str(deltaT)]);
fprintf(paramtxt,'\n');
fprintf(paramtxt,['Time-Steps: ' num2str(T+1)]);
fprintf(paramtxt,'\n');
fprintf(paramtxt,['Initial Vertex Randomization: ' num2str(shf)]);
fprintf(paramtxt,'\n');
fprintf(paramtxt,['Vertex Swap Threshold: ' num2str(eps)]);



% ********************************************************************


disp('SIMULATION COMPLETED.')

toc

disp(' ');

cd ..


end
```